ISBN 978-82-471-2590-8 (printed ver.)
ISBN 978-82-471-2591-5 (electronic ver.)
ISSN 1503-8181

Knut Sponheim Seim
Doctoral Thesis

Doctoral theses at NTNU, 2011:35

Knut Sponheim Seim

Mixing processes in dense overflows with emphasis on the Faroe Bank Channel overflow

NTNU
Norwegian University of
Science and Technology
Thesis for the degree of
philosophiae doctor
Faculty of Engineering Science and Technology
Department of Marine Technology

NTNU
Norwegian University of
Science and Technology

Doctoral theses at NTNU, 2011:35

NTNU

NTNU
Norwegian University of
Science and Technology

Knut Sponheim Seim

Mixing processes in dense overflows with emphasis on the Faroe Bank Channel overflow

Thesis for the degree of philosophiae doctor

Trondheim, February 2011

Norwegian University of
Science and Technology
Faculty of Engineering Science and Technology
Department of Marine Technology

NTNU
Norwegian University of
Science and Technology

NTNU
Norwegian University of Science and Technology

Thesis for the degree of philosophiae doctor

Faculty of Engineering Science and Technology
Department of Marine Technology

ISBN ISBN 978-82-471-2590-8 (printed ver.)
ISBN ISBN 978-82-471-2591-5 (electronic ver.)
ISSN 1503-8181

Doctoral Theses at NTNU, 2011:35

Printed by Tapir Uttrykk

Abstract

The amount and distribution of mixing and entrainment that the overflows across the Greenland-Scotland Ridge encounter influence the ventilation of the deep North Atlantic. Constituting about 30% of the total overflow (about 6 Sv) across the Greenland-Scotland Ridge, the continuous, swift overflow through the deepest passage from the Nordic Seas to the North Atlantic Ocean, the Faroe Bank Channel, is a major overflow in the region.

The mixing processes of the Faroe Bank Channel overflow are explored by combining results from observations, including the first direct turbulence measurements, numerical simulations of the overflow, and an idealized process study. The observations show an overflow characterized by strong lateral variability in entrainment and mixing, a transverse circulation actively diluting the bottom layer, and a pronounced vertical structure composed of an about 100 m thick stratified interface and a comparably thick well-mixed bottom layer. The turbulent overflow is associated with intense mixing and enhanced turbulent dissipation rate near the bottom and at the plume-ambient interface, but with a quiescent core.

Results from numerical simulations of the overflow with second order turbulence closures are compared to the observations. Turbulent dissipation rate and eddy diffusivity profiles inferred from the observations are used in refining the parameters of the turbulence closure. In the bottom-most 50-60 m, where the Richardson number is small and the production of turbulent kinetic energy is well-resolved, the model reproduces the observed vertical structure of enhanced dissipation rate and eddy diffusivity exceptionally well. In the interfacial layer and above the plume-ambient interface, however, the model does not resolve the mixing. A further investigation of the observations, addressing the role of the transverse circulation and internal waves in mixing in the stratified interface, shows that the transverse circulation effectively contributes to mixing of the overflow plume. Dissipation rates are more than doubled in the interfacial layer due to the transverse flow. In the ambient above the overflow plume, internal wave breaking is the dominant mechanism for dissipation of turbulent energy. In the interfacial

layer the main mechanism of mixing is the shear-instability and entrainment associated with the swift gravity current, enhanced by the secondary circulation. However, the internal wave continuum is energetic in the interfacial layer and may contribute to mixing.

To investigate the influence of unresolved small scale topography on the flow of a stratified fluid, a 2-m resolution, non-hydrostatic, three-dimensional numerical model is used. The drag and associated mixing on the stratified flow over real, 1-m resolution, complex topography (interpolated to model resolution) are studied. The results show that a significant drag can be exerted on the flow of a stratified layer overlaying a well-mixed layer (resembling the bottom and interfacial layer of the Faroe Bank Channel overflow) over rough topography. A parameterization of the internal wave drag is developed and implemented, and provides satisfactory results in terms of the domain integrated turbulent kinetic energy levels.

Acknowledgements

First of all I would like to thank my supervisors; Dag Myrhaug, Ilker Fer and Gunnar Furnes, for valuable scientific guidance. I am especially grateful to Ilker for his dedication and involvement. We have had a great cooperation which has been very valuable for me.
A special thanks to Jarle Berntsen for valuable discussions, ideas, and support, and to Helge Avlesen for providing the initial set-up on my last work and for support on his great, new set-up system for BOM.
Thanks to all colleagues at Department of Marine Technology, GFI, and the Production Facilities department, to Tove and Øyvind for housing me in Trondheim, and thanks to my good friend Gisle for "alt utenomsportslig".
Finally, thanks to friends and family, and especially to Tonje for encouragement and for enduring long working hours!

Contents

1. Outline

This study investigates mixing processes in dense overflows with a special focus on the Faroe Bank Channel overflow. The study is based on observations collected during a dedicated survey to the Faroe Bank Channel overflow region in June 2008, numerical simulations of the overflow, and an idealized process study. By combining results from observations and numerical simulations, a more complete understanding is achieved since each method has its limitations and advantages.

The thesis consists of an introduction followed by four papers. In the introduction, the scientific background is presented (Section 2) followed by a presentation of this study including a summary of the papers (Section 3). A discussion of the main results and future perspectives are given in Section 4.

The following four papers detail the results of this dissertation:

- **Paper I**:
  Intense mixing of the Faroe Bank Channel overflow
  I. Fer, G. Voet, K. S. Seim, B. Rudels and K. Latarius
  Geophysical Research Letters, Volume 37, L02604, doi:10.1029/2009GL041924, 2010

- **Paper II**:
  Regional simulations of the Faroe Bank Channel overflow using a σ-coordinate ocean model
  K. S. Seim, I. Fer, and J. Berntsen
  Ocean Modelling, Volume 35, 31-44, doi:10.1016/j.ocemod.2010.06.002, 2010

- **Paper III**:
  Mixing in the stratified interface of the Faroe Bank Channel overflow: the role of transverse circulation and internal waves
  K. S. Seim and I. Fer
  Submitted to Journal of Geophysical Research

- **Paper IV**:
  Stratified flow over complex topography
  K. S. Seim
  Manuscript in preparation for submission to Ocean Modelling

Paper I presents the first direct turbulence measurements from the Faroe Bank Channel overflow and the anatomy and mixing processes of the overflow. An idealized numerical model of the Faroe Bank Channel overflow was set up and the results are compared to the observations of **Paper I** and previous numerical studies of the overflow. These results are presented in **Paper II**. Using the observations and the regional numerical simulations in concert, we show that the mixing at the stratified interfacial layer and above is not adequately represented in the model, and identify the processes that need to be improved. These findings initiated a study of the observed mixing processes in the interfacial layer presented in **Paper III**. In **Paper IV** the importance of mixing due to unresolved topography is studied by carrying out numerical simulations of flow over high resolution topography. A parameterization is suggested to account for internal wave drag exerted in the water column.

Regarding the authorship and my contributions in these papers, I am the first author of **Papers II, III**, and I am the only author of **Paper IV**. I was responsible for performing the numerical simulations in **Papers II** and **IV**, and analysis of observations in **Paper III**, providing the results and discussions, and writing the papers under supervision of Prof. Ilker Fer. Prof. Ilker Fer and Prof. Jarle Berntsen contributed with comments and suggestions of improvement on **Paper II**. In **Paper III** Prof. Ilker Fer contributed with the data set and the part on the role of internal waves. As a third author of **Paper I** I participated at the field work, and contributed with comments and discussion on the results. **Paper I** is included to introduce the extensive data set from the Faroe Bank Channel overflow and our initial analyses and discussions of the anatomy and mixing processes of the overflow.

2. Scientific background

2.1 The Atlantic Meridional Overturning Circulation

The large scale ocean circulation (Fig. 2.1) can be thought of as a combination of currents driven by three different mechanisms (Rahmstorf, 2002): i) directly by winds (mostly confined to the upper several hundred metres of the sea), ii) by fluxes of heat and freshwater and subsequent interior mixing of heat and salt (the thermohaline circulation, THC), and iii) by tides. Because of its relevance for the global climate, the Atlantic meridional overturning circulation (AMOC) has been a major research focus for many years (Kuhlbrodt et al., 2007). Yet the main driver mechanism of the AMOC remains in debate. The circulation can, much simplified, be closed in four main branches: upwelling of abyssal water masses towards the ocean surface, poleward transport of relatively light water by surface currents, sinking dense water in deep water formation regions, and deep currents closing the loop (Kuhlbrodt et al., 2007).

It was first shown by Sandström (1908, 1916) (Sandström's theorem), by performing tank experiments and theoretical work, that a deep, thermally driven, closed, steady circulation in the ocean is only established if heating takes place at a higher presssure (deeper) than cooling. The ocean is heated at the tropics at the surface and cooled at high latitudes at the surface. Hence, deep mixing is a prerequisite for the deep circulation to be closed. The only possible sources of mechanical energy to drive the interior mixing are the winds and tides (Munk and Wunsch, 1998). Assuming a uniform upwelling associated with 25 Sv ($1\,\mathrm{Sv}{=}10^6\,\mathrm{m}^3\,\mathrm{s}^{-1}$) of deep water formation, Munk (1966) estimated that a diapycnal mixing coefficient of $10^{-4}\,\mathrm{m}^2\,\mathrm{s}^{-1}$ is needed to maintain the abyssal stratification. Subsequent measurements give a uniform pelagic (away from topography) diffusivity which is one order of magnitude smaller. This led Munk and Wunsch (1998) to reinterpret their diapycnal mixing coefficient (associated with 30 Sv of deep water formation) as a basin-wide spatial average, with values one order of magnitude smaller in the ocean interior and much higher values in a small number of localized mixing regions (sources of buoyancy flux). They estimate the energy available for mixing from wind and tides to be just what is necessary to upwell the deep water, with the reservation that such estimates are very

uncertain.

An alternative mechanism to the upwelling-diapycnal diffusion balance, is an upwelling balanced purely by kinetic energy input from winds. Toggweiler and Samuels (1998) show that the AMOC can be closed by upwelling south of the wind driven Antarctic Circumpolar Current (ACC) due to the divergence in the Ekman transport, with very little energy input from surface buoyancy forces. In this theory, the southward flow of deep waters from the North Atlantic is merely the return flow of the northward Ekman transport from the Southern Ocean. A strong sensitivity of the AMOC to Southern Ocean wind forcing is not found in all models (Rahmstorf and England, 1997) and the sensitivity decreases with increasing model resolution (Hallberg and Gnanadesikan, 2006).

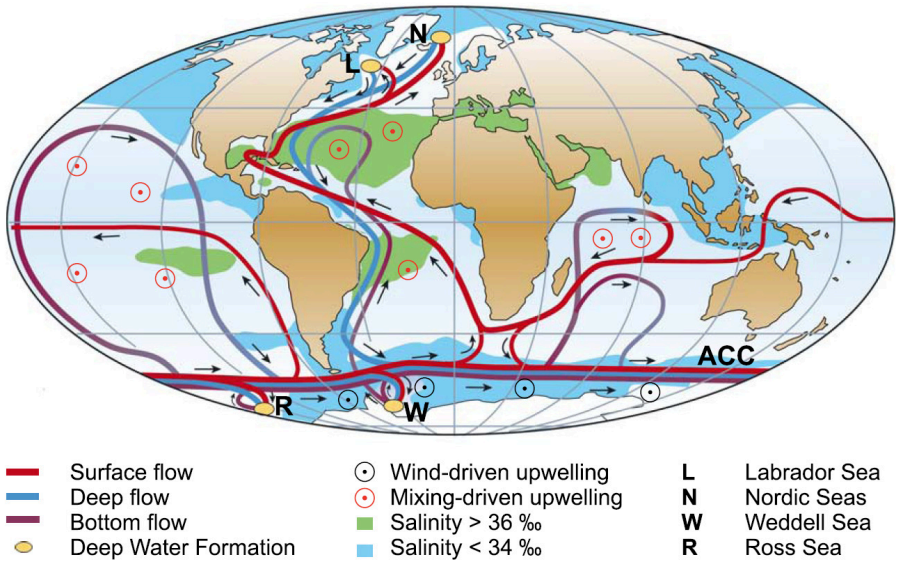

Figure 2.1: A simplified sketch of the global overturning circulation system (Kuhlbrodt et al., 2007).

The picture that emerges is that of an AMOC driven by both mixing and wind-driven upwelling (Kuhlbrodt et al., 2007). For the diapycnal mixing mechanism there is just enough energy input from wind and tides to rise the ocean background diapycnal diffusivity by one order of magnitude, but it is not obvious that all this energy is available for diapycnal mixing. Accounting for the Southern Ocean upwelling and arguing that only the vertical mixing of the deep water with North Atlantic origin needs to

be considered, Webb and Suginohara (2001) estimate the vertical mixing coefficient, averaged over the whole ocean, to be less than $3\times10^{-5}\,\mathrm{m^2\,s^{-1}}$. Hughes and Griffiths (2006) argue that the entrainment into the turbulent dense overflows has been neglected in the vertical advection-diffusion balance that maintains the deep density stratification. Buoyancy forcing at the sea surface might be capable of driving a substantial fraction, and perhaps all, of the overturning circulation if mixing of dense overflows currents is included in the balance. Dense overflows and the associated mixing processes are an important part of the AMOC and play a central role in "closing the loop".

"Any serious attempt to forecast future climate states requires an understanding of the present state" (Munk and Wunsch, 1998).

2.2 Dense overflows

According to Sandström's theorem, surface buoyancy cannot provide the energy necessary to drive the AMOC. However, it is essential for the formation of deep water. It is the deep water formation process that set the interhemispheric shape and the strength of the overturning cell (Kuhlbrodt et al., 2007). The density of the water masses is raised by surface cooling and ice freezing and brine rejection at high latitude and/or increased salinity due to evaporation. There are two distinct types of convection (Killworth, 1983). The first is the shelf convection initiated by brine release, as typified by various locations at Arctic and Antarctic shelves. The freezing of sea ice and subsequent brine rejection, results in cold, saline, dense water descending the shelf slope under a balance of Coriolis, gravity and frictional forces. The second convection process is the open-ocean convection. This process occurs in localized regions characterized by weak stratification and, in winter, exposed to intense buoyancy loss leading to deep-reaching convection (Killworth, 1983; Marshall and Schott, 1999). In the present climate, open-ocean deep convection occurs only in the Atlantic Ocean: the Labrador, Greenland, and Mediterranean Seas, and occasionally also in the Weddell Sea (Marshall and Schott, 1999).

On the Southern Hemisphere, the Filchner overflow in the Weddell Sea (Foldvik et al., 2004) is thought to be the most important overflow site, but overflows are also observed in the Ross Sea (Gordon et al., 2004) and other shelf locations around Antarctica (Baines and Condie, 1998). The dense water of Antarctic origin is fresher but colder and denser than the dense water formed at high, northern latitudes, and consequently occupies

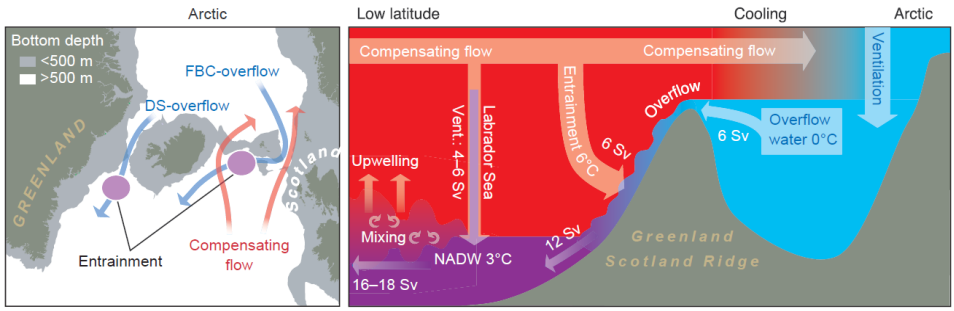

Figure 2.2: The exchange of water across the Greenland-Scotland Ridge. Arrows on the map indicate the main overflow (blue) and compensating inflow (red) branches. On the schematic section to the right, temperatures in °C and volume transports in Sv are given by approximate values (Hansen et al., 2004). DS: Denmark Strait; FBC: Faroe Bank Channel. From Hansen et al. (2004).

the major part of the deep ocean. On the northern Hemisphere, the dense water formed in the Arctic and in the Nordic seas has to cross the Greenland-Scotland ridge (Hansen and Østerhus, 2000). The northward flow of warm, saline Atlantic water is converted to colder water masses in the Arctic and the Nordic Seas, and returns southward over the ridge as cold fresh surface flows and dense overflows through deep passages across the ridge (Fig. 2.2). The overflow across the ridge consists of four distinct regions: the Denmark Strait, the Iceland-Faroe Ridge, the Faroe Bank Channel (FBC), and the Wyville Thomson Ridge. Across the Greenland-Scotland ridge a total transport of 6 Sv (Hansen and Østerhus, 2000) is approximately equally divided between the Denmark Strait, west of Iceland, and the overflow regions east of Iceland. With a transport of 2.1 Sv (Hansen and Østerhus, 2007) through the Faroe Bank Channel, 1 Sv across the Iceland-Faroe Ridge (Perkins et al., 1998), and 0.3 Sv across the Wyville Thomson Ridge (Sherwin et al., 2008), the Faroe Bank Channel overflow constitutes about 30% of the total overflow. The Faroe Bank Channel overflow is the focus of this study.

2.3 Dynamics and mixing of overflows

Dense turbulent overflows occur downstream of many sills and straits which separate ocean basins (Killworth, 2001). In the following section the dynamics and mixing of dense overflows entering ocean basins along continental

slopes will be briefly explained.

On basin scales, the Coriolis force will influence all motions. Dense water moving down a slope under the influence of gravity, is said to be in geostrophic balance if the gravity, or more accurately the pressure gradient force, is balanced by the Coriolis force. The along-flow geostrophic balance may be approximated by

$$fu = bS_y\,, \tag{2.1}$$

where u is the along-flow velocity, f the Coriolis parameter, $b = -g(\rho - \rho_0)/\rho_0$ is the buoyancy with respect to the background density ρ_0, and S_y is the bottom slope in the cross-flow direction. In this case the flow of dense water will be along isobaths and the overflow will not descend the slope. Since the overflow is a boundary flow it will be influenced by friction, and the flow may only be assumed to be in near geostrophic balance some distance away from the boundary. Under the influence of bottom friction the velocity decreases and veers to the left looking downstream (on the northern hemisphere) resulting in a down-slope component of the flow. The integrated transport in the bottom layer, influenced by bottom friction, is directed 90° to the left of the interior flow and is referred to as the Ekman transport. The down-slope transport results in a widening of the plume as it flows along the slope.

2.3.1 Entrainment

The flow of dense plumes down a slope is driven by the difference in buoyancy between the dense fluid and its environment. As the plume flows down the slope, instabilities on the interface between the plume and the more buoyant fluid above may lead to entrainment of the fluid above. There are different mechanisms causing entrainment, e.g. shear induced turbulence, Kelvin-Helmholtz instability (Özgökmen and Chassignet, 2002; Özgökmen et al., 2004), roll-waves (Cenedese et al., 2004), and hydraulic transitions. In addition to a vertical buoyancy flux (mixing) associated with entrainment, the entrained fluid generally has no or less momentum than the dense flow, and thus entrainment exerts a drag (vertical flux of momentum) on the flow.

The entrainment parameter, E, is commonly defined as $E = w_E/U$ (e.g. Ellison and Turner, 1959), where w_E is the entrainment velocity and U is the flow velocity. Performing laboratory experiments, Ellison and Turner (1959) defined E as a function of the overall Richardson number of the dense flow defined as $Ri = g'h/U^2$, where $g' = g(\rho - \rho_0)/\rho_0 = -b$ is the reduced gravity. Parameterizations of E based on the non-rotating laboratory experiments of Ellison and Turner (1959) and Turner (1986) are widely used. Both

parameterizations assume no entrainment ($E = 0$) if Ri is above a critical value (1 and 0.8 for the two parameterizations, respectively). However, subcritical mixing is observed in rotating laboratory experiments (Cenedese et al., 2004; Adduce and Cenedese, 2008) and a parameterization allowing for mixing when Ri is above the critical value is proposed by Adduce and Cenedese (2008).

Similar to the entrainment parameterizations, turbulence closure models typically predict the collapse of turbulent transport in stratified regions with negligible shear (i.e. $Ri \gg 1$), although observations show mixing for subcritical Ri. As the local shear production of turbulent kinetic energy (TKE) is negligible in such a situation, the energy has to come from another source. Two alternative energy sources have been identified: vertical transport of TKE from neighboring regions by turbulent motions (Umlauf, 2009), and TKE generated by internal waves (Baumert and Peters, 2009).

2.3.2 Role of internal waves

Mixing in boundary layers and mean shear flows are commonly represented in turbulence closure models. These models originate from turbulence theory of neutrally stratified flows and are completely ignorant of internal waves (Baumert and Peters, 2009). From laboratory experiments, direct numerical simulations and idealized theoretical considerations of stratified, spatially homogeneous shear layers, the following turbulence regimes are found (Baumert and Peters, 2009):

- $Ri_g \leq Ri_g^a = 0$: unstable and neutral stratification, convective and neutral turbulence, no internal waves.
- $Ri_g^a < Ri_g < Ri_g^b = 1/4$: neutral and stable stratification, shear-dominated growing turbulence, coexistence of turbulence and nonlinear internal waves.
- $Ri_g^b < Ri_g < Ri_g^c = 1/2$: stable stratification, wave dominated decaying turbulence, coexistence of turbulence and internal waves.
- $Ri_g^c < Ri_g$: stable stratification, waves-only regime.

Here the mean-flow gradient Richardson number, $Ri_g = N^2/S^2$, is given as the ratio of the buoyancy frequency, $N = \sqrt{(g/\rho_0)\partial\rho/\partial z}$ and the vertical shear of the mean velocity, $S = \partial U/\partial z$. The numerical limits, Ri_g^a, Ri_g^b, and Ri_g^c are only valid for the asymptotic case of an infinite Reynolds number, but turbulence occurs at larger Ri_g in the ocean due to the presence of saturated internal waves.

A possible local generation mechanism of internal waves in dense overflows is rough bottom topography. Depending on the intrinsic frequency of the flow, U/L, given by the flow speed and the length scale of the topography, and the buoyancy frequency of the flow, N, evanescent or propagating waves may be exerted, only the latter resulting in a pressure gradient over the obstacle and an associated drag force (e.g. Baines, 1995).

2.3.3 Lateral mixing - eddies

Eddies are commonly observed in dense overflows. Bruce (1995) observed numerous cold cyclonic eddies in satellite IR imagery along the East Greenland Shelf South-West of the Denmark Strait. He suggests that the eddies are generated by vortex stretching associated with the sinking of dense overflow water downstream of the Denmark Strait sill. Such eddies are confirmed in laboratory experiments (Lane-Serff and Baines, 1998a,b; Cenedese et al., 2004) and are associated with stretching of the fluid column above the current resulting in rotation to conserve the potential vorticity. A second category of eddies are the eddies generated from baroclinic instabilities (Swaters, 1991). Using parameters (bottom slope, density contrast, ambient stratification) characteristic for the Denmark Strait overflow plume, Jungclaus et al. (2001) found that baroclinic instability was responsible for the initial destabilization of the overflow plume.

For a zero potential vorticity, hydraulically driven sill flow in a rotating parabolic channel, Pratt et al. (2008) have shown that the linear stability only depends on the curvature of the channel, and their calculations suggest that the flow is always unstable. Maximum growth rates and the density of unstable wavenumbers increase as the channel is made dynamically wider (decreased curvature). The largest growth rates are associated with the interaction of two frontal/Kelvin-type waves trapped to opposite edges of the flow. Downstream of a controlling sill, wave breaking leads to a widening of the flow and if the curvature is sufficiently small, the flow eventually breaks into a train of eddies.

2.3.4 Transverse circulation

Ageostrophic processes, such as the Ekman transport and baroclinic eddies, will cause a cross-isobath, downslope transport of the dense water. Dense water may also be steered downslope by submarine canyons (Wåhlin, 2002, 2004; Darelius, 2008) and ridges (Darelius and Wåhlin, 2007). Downward steering of dense plumes and plumes passing through channel-like topography has been observed in several major overflows: the Filchner overflow

(Foldvik et al., 2004; Darelius and Wåhlin, 2007), the Faroe Bank Channel overflow (Johnson and Sanford, 1992; Fer et al., 2010), Mediterranean outflow (Baringer and Price, 1997), and the Red Sea outflow (Peters et al., 2005; Peters and Johns, 2005). Channelized overflows are also found in smaller scale in the Baltic Sea (Arneborg et al., 2007; Umlauf and Arneborg, 2009a) and in the Wyville Thompson overflow (Sherwin and Turrell, 2005; Sherwin et al., 2008; Sherwin, 2010).

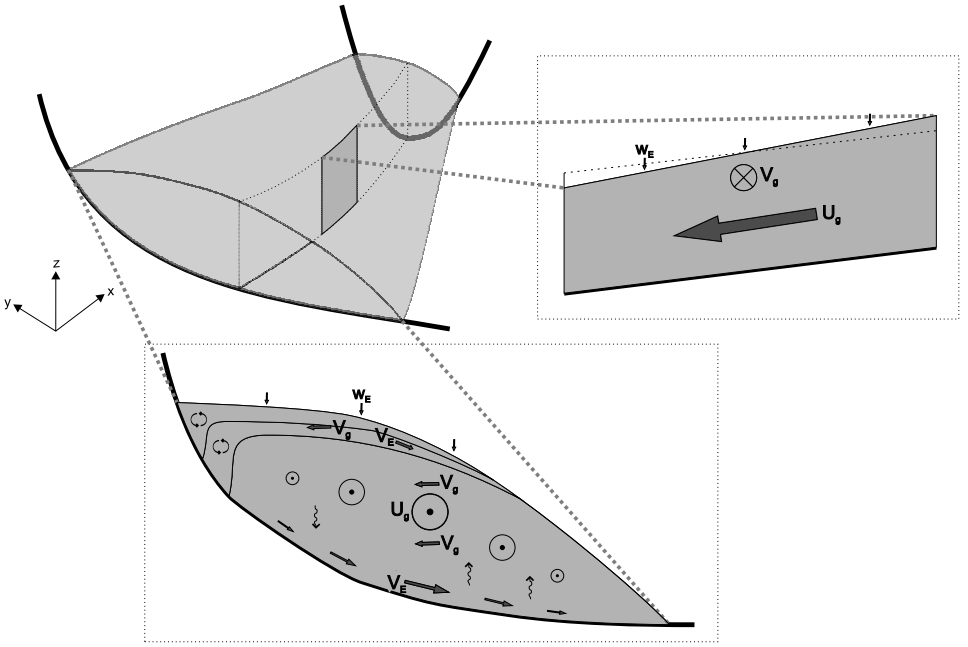

Figure 2.3: Illustration of the transverse circulation in an along-stream and cross-stream section. Arrows illustrate geostrophic velocities (U_g along-stream and V_g cross-stream), Ekman transport (V_E), and entrainment velocity (w_E). Vertical motions due to overturning and Ekman transport divergence/convergence are also depicted. From Seim and Fer (2010).

A simple model of the flow through a channel (or along a corrugation) can be achieved by assuming that the flow along the channel is geostrophically balanced, and that the speed is adjusted by friction such that the bottom stress balances the interfacial stress along the channel (Wåhlin, 2004; Darelius, 2008). For a steady flow, this means that the Ekman transport in the bottom layer has to be balanced by the oppositely directed geostrophic flow in the cross-channel direction as the flow is laterally constrained within

the channel. The divergence of the Ekman flow causes the fluid to move between the Ekman layer and the interior flow (Fig. 2.3). Analysing data from a channelized gravity current in the western Baltic Sea, Umlauf and Arneborg (2009b) found a complex transverse circulation modifying the entrainment process by i) laterally draining the interface and ii) providing additional interfacial shear comparable to the down-channel shear. This shallow gravity current is characterized by Ekman numbers in the order of unity, but transverse circulation is also found to significantly affect the dynamics of deeper overflows (Johnson and Sanford, 1992; Fer et al., 2010; Sherwin, 2010).

2.4 The Faroe Bank Channel overflow

The Faroe Bank Channel (see Fig. 2.4) is the deepest passage across the Greenland-Scotland Ridge and the deep part of this channel is home to swift flow of cold, dense water toward the Atlantic (Borenäs and Lundberg, 1988; Hansen and Østerhus, 2000, 2007). Since its importance for the exchange between the North Atlantic and the Nordic Seas was recognized by Cooper (1955), the FBC overflow has been studied extensively: Overflow '60 (Harvey, 1965), Overflow '73 (Dooley and Meincke, 1981), NANSEN (Borenäs and Lundberg, 1988; Saunders, 1990, 1992), and the Nordic WOCE and VEINS (Hansen et al., 2001). Recent studies of the overflow include Duncan et al. (2003); Mauritzen et al. (2005); Prater and Rossby (2005); Geyer et al. (2006); Fer et al. (2010). The overflow water is characterised by a vertically stratified plume structure, with a stratified, interfacial layer, 120 m thick on average, and a well-mixed bottom layer of 70 m average thickness (Fer et al., 2010). At the FBC sill the cold core of the overflow is significantly thicker, on average 250 m (Mauritzen et al., 2005), and has a mean velocity of $1\,\mathrm{m\,s^{-1}}$. The volume transport of the overflow at the sill is 2.1 Sv, inferred from continuous measurements from 1995 to 2005 (Hansen and Østerhus, 2007). Downstream of the sill, the overflow enters the Iceland-Faroe slope and starts descending the slope under frictional control. Approximately 100 km downstream of the sill, the plume accelerates as it descends from 800 to 1200 m, and the highest velocities ($>1.2\,\mathrm{m\,s^{-2}}$) and buoyancy fluxes are found at this section (Mauritzen et al., 2005). Quantifying the mixing of the FBC overflow using overturning length scales (Thorpe, 1977), Mauritzen et al. (2005) find very high diapycnal mixing coefficients ($600\text{-}1000\times10^{-4}\,\mathrm{m^2\,s^{-1}}$), particularly close to the bottom associated with frictional drag. Although one order of magnitude smaller (around $100\times10^{-4}\,\mathrm{m^2\,s^{-1}}$), enhanced levels of mixing in the inter-

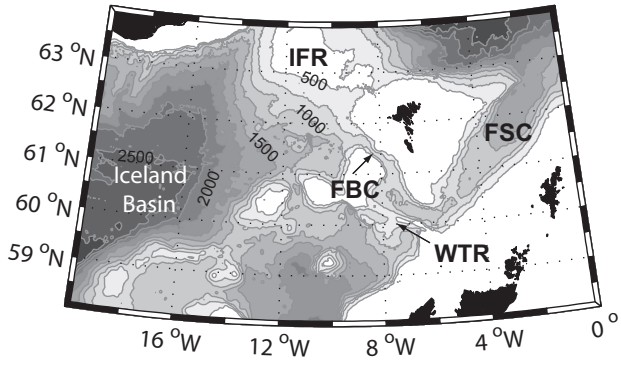

Figure 2.4: Bathymetry of the channel system around the Faroe islands. Isobaths are drawn at 250-m intervals starting with 500 m. FBC: Faroe Bank Channel; FSC: Faroe Shetland Channel; WTR: Wyville-Thomson Ridge; and IFR: Iceland-Faroe ridge. From Seim et al. (2010).

face will significantly affect the water masses compared to the maximum mixing in the bottom layers with fairly homogeneous stratification. Mauritzen et al. (2005) conclude that the hydrographic properties of the FBC overflow are set within 100-150 km downstream of the sill. The mixing is found to be enhanced in the Faroese Channels compared to the Denmark Strait resulting in significantly warmer deep water masses downstream of the FBC sill although it is deeper than the Denmark Strait.

A regular pattern of strong temperature and velocity oscillations has been observed in the FBC overflow. In-situ observations downstream of the FBC sill show large current and temperature fluctuations with a period of 3.5 days associated with mesoscale eddies (Høyer and Quadfasel, 2001). A similar variation (∼3.7 days) in near-bottom temperature and velocity measurements is reported by Geyer et al. (2006), and in highly idealized numerical simulations of the overflow (Ezer, 2005). Based on numerical model results Ezer (2006) identifies three flow regimes resembling those found in the laboratory experiments of Cenedese et al. (2004): a sub-critical flow upstream of the sill, a "wave" regime (periods of 3-6 days) from the sill to 100-200 km downstream where the flow is super-critical with strong mixing and entrainment, and an "eddy" regime farther downstream.

The Faroe Bank Channel overflow is a highly variable, both in time and space, dense overflow associated with intense mixing and entrainment. Constituting almost 30% of the total overflow of dense water across the Greenland-Scotland Ridge, understanding the dynamics of the FBC over-

flow is important to improve the understanding of the global overturning circulation.

3. This study

3.1 Motivation and objectives

The aim of this study is to identify and investigate the processes of importance for the mixing of dense overflows, focussing on the Faroe Bank Channel overflow. As described in previous sections, the diapycnal mixing, transporting heat from surface to the deep water masses, is crucial for the maintenance of the present-day overturning circulation. The average pelagic diffusivity is too small to support the mixing required to maintain the abyssal stratification. A small number of regions with intense mixing ("hot-spots"), associated typically with variable bottom topography, are proposed to account for the "missing mixing". The enhanced levels of mixing observed in regions of dense overflows can further reduce this discrepancy to sustain the overturning circulation, and are certainly important for the formation of the deep water masses. Yet, the processes determining the mixing of major dense overflows are, to a large degree, unknown.

With this motivation, the following questions are addressed in this study:

i) Which processes are important for the mixing of the Faroe Bank Channel overflow? How does the observed mesoscale variability affect the descent and mixing of the overflow plume?

ii) How is the thick, stratified interfacial layer of the overflow plume maintained, and which processes dominate the mixing there?

iii) Can numerical models with state-of-the-art turbulence closure models represent the mixing of the overflow? Is the unresolved topography important for the mixing of overflow plumes?

3.2 Methods

This study is a combination of unique observations and numerical modelling, used in concert to complement each other to achieve a better understanding of mixing processes in dense overflows. All observed data used in this

study were obtained during the cruise of R.V. Håkon Mosby to the Faroe Bank Channel overflow region between 29 May and 8 June 2008 and from moored instruments deployed in the period from 14 May to 18 July 2008. The dataset includes vertical properties of hydrography and velocity, turbulence profiles from a microstructure profiler, and time series of hydrography and velocity from the moored instruments. Horizontal current profiles were collected by a pair of acoustic Doppler current profilers attached to the Conductivity-Temperature-Depth (CTD) rosette. The profiles of dissipation rate (ε) are obtained as 1 m averages from shear probes of the tethered free-fall microstructure profiler. Processing of current profiles, CTD, and microstructure data is done employing widely-used matured methods. From the dissipation rate the diapycnal eddy diffusivity was estimated by three different models following Osborn (1980); Shih et al. (2005) and Peters and Baumert (2007). Analysis of data involves time series analysis, frequency domain spectral analysis, as well as inferring integral plume properties over pre-defined layers and occupied sections.

An idealized regional numerical model of the Faroe Bank Channel overflow was set up with identical bathymetry and forcing to a recent study of the overflow using a z-level model (Riemenschneider and Legg, 2007) to be able to compare our σ-coordinate model (Bergen Ocean Model, BOM) to the observations and the z-level model. The bathymetry and forcing data were provided by U. Riemenschneider and S. Legg. The horizontal resolution of the model is 2 km. In the vertical 32 layers are used, with increasing resolution toward the bottom resulting in a near-bottom vertical resolution ranging from about 2 m to 22 m, depending on the bottom depth. To parameterize sub-grid-scale processes, three different second order turbulence closure models were applied in the vertical: the Mellor and Yamada (1982) 2-1/2 scheme implemented in BOM, the k-ε model, or the k-ω model, the two latter by coupling the General Ocean Turbulence Model (GOTM Umlauf et al., 2006) to BOM. The results of the simulations were evaluated by comparing the volume transports of dense overflow water to observations and the results of the z-level model. The diffusivity and dissipation rate estimated by the model were compared to the microstructure measurements to assess the performance of the turbulence closure models.

To evaluate the influence of complex topography on stratified flow (specifically in a stratified layer resembling the stratified interface of the Faroe Bank Channel overflow), another numerical model case was set up using the non-hydrostatic, parallelized version of BOM. Real, unique topographic data with a resolution of 1 m from a 400 m $\times$ 400 m region was interpolated

to a grid with horizontal resolution of 2 m and a vertical resolution of about 2 m. A parameterization of the drag induced by breaking internal waves, based on linear, two-dimensional, hydrostatic wave solutions, was tested on the flow over a flat bottom with stratification resembling the Faroe Bank Channel overflow water. The topography inducing the internal waves is represented in the parameterization by its statistical properties.

3.3 Summary of papers

This work is presented in Papers I-IV summarized below.

3.3.1 Paper I

Intense mixing of the Faroe Bank Channel overflow
Published in Geophysical Research Letters

In this paper the dynamic properties and mixing of the Faroe Bank Channel overflow are described using the first direct turbulence measurements and vertical profiles of hydrography and velocity. The overflow plume is on average 160±70 m thick and, similar to other major overflows (Red Sea, the Denmark Strait, and the Mediterranean overflow), the presence of a stratified interfacial layer (IL, 120±60 m thick) is observed. The overflow transport is equally distributed between the IL and the well-mixed layer below the IL, the well-mixed bottom layer (BL), with average magnitudes of 0.9±0.1 Sv and 1±0.3 Sv for the two layers, respectively.
Exceptionally high dissipation rates reaching $10^{-5}\,\mathrm{W\,kg^{-1}}$ are measured in the IL and BL with a quiescent region in between associated with the velocity maximum. Enhanced mixing at the strongly stratified and sheared IL can be due to coexisting shear instabilities and internal wave-turbulence transition and vertical transport of turbulence. The vigorous turbulence near the bottom is due to the bottom shear stress and weak stratification.
The transverse velocity component has a vertical structure with an Ekman transport, to the left looking downstream, in the BL and an opposing transport to the right in the IL (a transverse transport due to the downchannel tilt of the interface). This transverse circulation actively dilutes the BL by supplying warmer interface water into the Ekman layer.
According to our findings, neither bulk entrainment parameterizations, nor traditional turbulence closure models will be adequate in representing the mixing of the dense overflow plume downstream of the Faroe Bank Channel sill.

3.3.2 Paper II

Regional simulations of the Faroe Bank Channel overflow using a σ-coordinate ocean model
Published in Ocean Modelling

This paper presents the results of idealized numerical simulations of the Faroe Bank Channel overflow using a terrain-following ocean model. The terrain-following coordinate system eliminates the spurious mixing resulting from the step topography in z-coordinate models. Turbulence closure schemes are introduced in the vertical to account for the unresolved mixing. Turbulent dissipation rate and eddy diffusivity profiles inferred from the observations (**Paper I**) are used in refining the parameters of the turbulence closure. The model reproduces the features of the overflow plume reasonably well. At the sill the transport is within 20% of the observed transport, which is in better agreement than a recent z-level model study with identical forcing of the model.
Near the bottom the dissipation rate and eddy diffusivity dictated by the turbulence closure compare exceptionally well with the direct measurements reported in **Paper I**. This is because the production of turbulent kinetic energy is well resolved. In the interfacial layer, however, the model dissipation rate and eddy diffusivity drop to levels well below the observations. This is due to the unresolved processes in the interfacial layer leading to mixing of the overflow at Richardson numbers around unity.
In accordance with observations, the model develops low-frequency oscillations with a period of 4-4.5 days downstream of the sill where the overflow enters the Iceland-Faroe slope. The regular oscillations are shown to have a strong impact on the mixing and the descent rate of the overflow plume. They are associated with enhanced levels of dissipation rate and periodic rapid cross-isobath descent of the plume. Similarly, enhanced mixing and rapid descent can be expected in other major overflows with comparable mesoscale eddies and low frequency fluctuations.

3.3.3 Paper III

Mixing in the stratified interface of the Faroe Bank Channel overflow: the role of transverse circulation and internal waves
Submitted to Journal of Geophysical Research

Motivated by **Paper I** and **II**, this paper addresses mixing in the stratified interface. Analyzing observations of hydrography, currents, and turbulence, the role of the transverse circulation and internal waves in mixing in the

stratified plume-ambient interface is described.
In the stream-wise direction entrainment stress is found to be negligible, and the momentum budget is dominated by a balance between the pressure gradient and bottom friction. In the transverse direction, the velocity is in near geostrophic balance, and the variability is governed by the tilt of the isotherms relative to the bottom slope. This cross-stream flow in the interfacial layer, together with the flow near the bottom (Ekman transport), effectively contributes to mixing in several ways: i) by diluting the bottom layer of the plume, ii) by acting as an advective source of buoyancy, iii) by transporting interfacial layer water to the right of the stream-wise flow, iv) by reducing the Richardson number in the interfacial layer, and v) by convection on the upper slope. Dissipation rates are more than doubled in the interfacial layer due to the transverse flow.
The main mechanism of mixing of the overflow plume is the shear-instability and entrainment associated with the swift gravity current. However, we find that the internal wave continuum is energetic in the interfacial layer and may significantly contribute to mixing. Above the overflow plume, the main mechanism of dissipating turbulent kinetic energy is breaking of internal waves.

3.3.4 Paper IV

Stratified flow over complex topography
Manuscript in preparation

This paper describes the flow of stratified water over realistic, complex topography and the associated drag on the fluid exerted by the obstacles. A non-hydrostatic numerical ocean model is used to simulate the flow of stratified fluid for cases with linear and hyperbolic tangent density profiles. The latter is chosen to be representative of the well mixed bottom layer and the stratified interface of the Faroe Bank Channel overflow to illustrate the possible interfacial mixing caused by rough bottom topography. The flow is over real topography, represented by a unique dataset sampled at 1 m resolution, allowing for realistic flow topography interaction. The simulations show that the topography leads to wave breaking and significant mixing in the stratified interface. The drag exerted on the flow reduces the domain integrated velocity by up to 27%.
A parameterization, based on linear, two-dimensional, hydrostatic wave solutions, of the drag exerted on the flow by unresolved topography is tested. The parameterization predicts the wave breaking at the correct level and yields comparable levels of turbulent kinetic energy compared to the sim-

ulations resolving the topography. However, the parameterization overestimates the drag in the layer where the wave breaking is effective due to a too shallow momentum flux deposit layer.

4. Conclusions and outlook

In this section the main results and conclusions of Papers I-IV are presented, followed by suggestions for future work.

4.1 Main results and conclusions

Mixing of the overflow The Faroe Bank Channel is characterised by strong lateral variability in entrainment and mixing with a significant vertical structure including an about 100 m thick strongly stratified interfacial layer. Exceptionally large dissipation rates, reaching $10^{-5}\,\mathrm{W\,kg^{-1}}$, are found in the bottom layer and in the stratified interface. The Richardson number is below unity in the stratified interface with a minimum value of 0.6. In the well-mixed bottom layer Ri<1 in the entire layer with Ri<0.25 in the bottom-most 25 m. The weak stratification in combination with the mean shear in the bottom boundary layer causes the low Ri, but leads to negligible water mass transformations as the bottom layer is fairly homogeneous. In the interfacial layer, the low (but not sub-critical) Ri is due to strong shear across the strongly stratified interface. The enhanced mixing in the layer is due to shear instability enhanced by the transverse (secondary) circulation. The energetic internal wave continuum suggests that internal waves may contribute to mixing in the stratified interface.

Representation of the overflow in a numerical model A numerical model was set up for the Faroe Bank Channel overflow region with idealized forcing (no wind and tide). The results are compared with observations of hydrography, currents, and turbulence; the model reproduces the features of the plume reasonably well. The volume transport at the sill is within 20% of the observed transport. Three different second-order turbulence closures are applied to account for the unresolved mixing. In the bottom boundary layer the model resolves the Richardson number; the dissipation rates from the turbulence closure are in exceptional agreement with the observed values. In the stratified layer, on the other hand, where Ri is above the critical threshold, the turbulence models underestimate the dissipation rate.

The model develops low-frequency oscillations with a period of 4-4.5 days between 50 and 100 km downstream of the sill. These mesoscale variations in the overflow are comparable to both earlier numerical simulations

and observations from moored instruments. The regular oscillations have a strong impact on the descent rate and mixing of the plume.

Unresolved topography The breaking of internal waves, and the associated drag, induced by unresolved topography is generally ignored in ocean modelling, although the importance of varying topography in the average ocean diapycnal mixing has been recognized. In this study it is shown that small scale topography (defined by a restriction on the length scale of an obstacle, $L < U/N$, where U and N are the flow speed and buoyancy frequency, respectively) variation induces a significant drag on a stratified flow, and it is hypothesized that it may be important in the mixing of dense overflows. Applying a hyperbolic tangent density profile, resembling the stratified interfacial layer of the Faroe Bank Channel overflow above a well-mixed bottom layer, we find that internal waves breaking in the stratified layer induce a significant drag on the flow, reducing the velocity up to 27%. A parameterization of the internal wave drag is implemented and tested, resulting in comparable levels of domain integrated turbulent kinetic energy. The parameterization successfully predicts the level of wave breaking, but the deposit of momentum flux is too shallow leading to an overestimated drag in the layer.

4.2 Future work

The work presented in this thesis is a step toward a better understanding of the mixing processes in dense overflows, illustrated by discussing the Faroe Bank Channel overflow. The observations presented here show enhanced levels of mixing of the overflow plume, particularly in the stratified interface. This is not captured by state-of-the-art turbulence closures, and improved models are needed. Considerable advances are made in making models with no finite critical Ri (Canuto et al., 2008; Umlauf, 2009) and mixing due to internal gravity waves (Baumert and Peters, 2009), and applying such turbulence closures in dense overflow modelling should be explored.

The parameterization of drag induced by internal gravity waves due to unresolved topography was only tested in a highly idealized model with constant velocity and buoyancy forcing. The result of applying the parameterization on a larger scale case, like the Faroe Bank Channel overflow model, is the next step in testing the parameterization.

The observed data set presented here is an extensive and detailed data set, but has a few shortages. The highly variable overflow requires very

high spatial and temporal resolution. Long time mooring arrays covering the whole vertical extent of the plume and designed to capture the transverse circulation and the variability in the interfacial layer, would certainly improve the understanding of the mixing processes in the Faroe Bank Channel overflow.

Bibliography

Adduce, C., Cenedese, C., 2008. Mixing in a density driven current down a slope in a rotating fluid. J. Fluid Mech. 604, 369–388.

Arneborg, L., Fiekas, V., Umlauf, L., Burchard, H., 2007. Gravity current dynamics and entrainment - a process study based on observations in the Arkona Basin. J. Phys. Oceanogr. 37, 2094–2113.

Baines, P. G., 1995. Topographic Effects in Stratified Flows. Cambridge Monographs on Mechanics. Cambridge University Press.

Baines, P. G., Condie, S., 1998. Observations and modelling of Antarctic downslope flows: a review. In: Jacobs, S. S., Weiss, R. F. (Eds.), Ocean, Ice, and Atmosphere: Interactions at the Antarctic Continental Margin. Vol. 75. AGU, Washington D.C.

Baringer, M. O., Price, J. F., 1997. Mixing and spreading of the Mediterranean Outflow. J. Phys. Oceanogr. 27, 1654–1677.

Baumert, H. Z., Peters, H., 2009. Turbulence closure: turbulence, waves and the wave-turbulence transition - Part 1: Vanishing mean shear. Ocean Sci. 5, 47–58.

Borenäs, K. M., Lundberg, P. A., 1988. On the deep-water flow trough the Faroe-Bank Channel. J. Geophys. Res. 93, 1281–1292.

Bruce, J. G., 1995. Eddies southwest of the Denmark Strait. Deep-Sea Res. I 42, 13–29.

Canuto, V. M., Cheng, Y., Howard, A. M., Esau, I. N., 2008. Stably stratified flows: a model with no Ri(cr). J. Atmos. Sci. 65, 2437–2447.

Cenedese, C., Whitehead, J. A., Ascarelli, T. A., Ohiwa, M., 2004. A dense current flowing down a sloping bottom in a rotating fluid. J. Phys. Oceanogr. 34, 188–203.

Cooper, L. H. N., 1955. Deep water movements in the North Atlantic as a link between climatic changes around Iceland and biological productivity of the English Channel and Celtic Sea. J. Mar. Res. 14, 347–362.

Darelius, E., 2008. Topographic steering of dense overflows: Laboratory experiments with V-shaped ridges and canyons. Deep-Sea Res. I 55, 1021–1034.

Darelius, E., Wåhlin, A. K., 2007. Downward flow of dense water leaning on a submarine ridge. Deep-Sea Res. I 54, 1173–1188.

Dooley, H. D., Meincke, J., 1981. Circulation and water masses in the Faroese Channels during Overflow '73. Dt. Hydrogr. Z. 34, 41–45.

Duncan, L. M., Bryden, H. L., Cunningham, S. A., 2003. Friction and mixing in the Faroe Bank Channel outflow. Oceanol. Acta 26, 473–486.

Ellison, T. H., Turner, J. S., 1959. Turbulent entrainment in stratified flow. J. Fluid Mech. 6, 423–448.

Ezer, T., 2005. Entrainment, diapycnal mixing and transport in three-dimensional bottom gravity current simulations using the Mellor-Yamada turbulence scheme. Ocean Model. 9, 151–168.

Ezer, T., 2006. Topographic influence on overflow dynamics: idealized numerical simulations and the Faroe Bank Channel. J. Geophys. Res. 111, doi:10.1029/2005JC003195.

Fer, I., Voet, G., Seim, K. S., Rudels, B., Latarius, K., 2010. Intense mixing of the Faroe Bank Channel overflow. Geophys. Res. Lett. 37, L02604, doi:10.1029/2009GL041924.

Foldvik, A., Gammelsrød, T., Østerhus, S., Fahrbach, E., Rohardt, G., Schröder, M., Nicholls, K. W., Padman, L., Woodgate, R. A., 2004. Ice shelf water overflow and bottom water formation in the southern Weddell Sea. J. Geophys. Res. 109, C02015.

Geyer, F., Østerhus, S., Hansen, B., Quadfasel, D., 2006. Observations of highly regular oscillations in the overflow plume downstream of the Faroe Bank Channel. J. Geophys. Res. 111, C12020, doi:10.1029/2006JC003693.

Gordon, A. L., Zambianchi, E., Orsi, A., Visbeck, M., Giulivi, C. F., Withworth III, T., Spezie, G., 2004. Energetic plumes over the western Ross Sea continental slope. Geophys. Res. Lett. 31, L21302.

Hallberg, R., Gnanadesikan, A., 2006. The role of eddies in determining the structure and response of the wind-driven Southern Hemisphere overturning: Results from the modeling eddies in the Southern Ocean project. J. Phys. Oceanogr. 36, 2232–2252.

Hansen, B., Østerhus, S., 2000. North Atlantic-Nordic Seas exchanges. Prog. Oceanogr. 45, 953–954.

Hansen, B., Østerhus, S., 2007. Faroe Bank Channel overflow 1995-2005. Prog. Oceanogr. 75, 817–856.

Hansen, B., Østerhus, S., Quadfase, D., Turrell, W., 2004. Already the day after tomorrow. Science 305, 817–856.

Hansen, B., Turrell, W. R., Østerhus, S., 2001. Decreasing overflow from the Nordic Seas into the Atlantic Ocean through the Faroe Bank channel since 1950. Nature 411, 929–930.

Harvey, J., 1965. The topography of the South-Western Faroe Channel. Deep-Sea Res. 12, 121–127.

Høyer, J. L., Quadfasel, D., 2001. Detection of deep overflows with satellite altimetry. Geophys. Res. Lett. 28(8), 1611–1614.

Hughes, G. O., Griffiths, R. W., 2006. A simple convective model of the global overturning circulation, including effects of entrainment into sinking regions. Ocean Model. 12, 46–79.

Johnson, G., Sanford, T., 1992. Secondary circulation in the Faroe Bank Channel outflow. J. Phys. Oceanogr. 22, 927–933.

Jungclaus, J. H., Hauser, J., Käse, R. H., 2001. Cyclogenesis in the Denmark Strait overflow plume. J. Phys. Oceanogr. 31, 3214–3229.

Killworth, P. D., 1983. Deep convection in the world ocean. Rev. Geophys. Space Ge. 21, 1–26.

Killworth, P. D., 2001. On the rate of descent of overflows. J. Geophys. Res. 106 (C10), 22,267–22,275.

Kuhlbrodt, T., Griesel, A., Levermann, A., Hofmann, M., Rahmstorf, S., 2007. On the driving processes of the Atlantic meridional overturning circulation. Rev. Geophys. 45, 2001–2032.

Lane-Serff, G. F., Baines, P. G., 1998a. Eddy formation by dense flows on slopes in a rotating fluid. J. Fluid Mech. 363, 229–252.

Lane-Serff, G. F., Baines, P. G., 1998b. Eddy formation by overflows in stratified water. J. Phys. Oceanogr. 363, 229–252.

Marshall, J., Schott, F., 1999. Open-ocean convection: Observations, theory, and models. Rev. Geophys. 37, 1–64.

Mauritzen, C., Price, J., Sanford, T., Torres, D., 2005. Circulation and mixing in the Faroese Channels. Deep-Sea Res. I 52, 883–913.

Mellor, G. L., Yamada, T., 1982. Development of a turbulence closure model for geophysical fluid problems. Rev. Geophys. Space Phys. 20, 851–875.

Munk, W., 1966. Abyssal recipes. Deep-Sea Res. 13, 707–730.

Munk, W., Wunsch, C., 1998. Abyssal recipes II: energetics of tidal and wind mixing. Deep-Sea Res. I 45, 1978–2010.

Osborn, T. R., 1980. Estimates of the local rate of vertical diffusion from dissipation measurements. J. Phys. Oceanogr. 10 (1), 83–89.

Özgökmen, T. M., Chassignet, E. P., 2002. Dynamics of Two-Dimensional Turbulent Bottom Gravity Currents. J. Phys. Oceanogr. 32, 1460–1478.

Özgökmen, T. M., Fischer, P. F., Duan, J., Iliescu, T., 2004. Three-Dimensional Turbulent Bottom Density Currents from a High-Order Nonhydrostatic Spectral Element Model. J. Phys. Oceanogr. 34, 2006–2026.

Perkins, H., Hopkins, T. S., Malmberg, S.-A., Poulain, P.-M., Warn-Varnas, A., 1998. Oceanographic conditions east of Iceland. J. Geophys. Res. 103 (C10), 21,531–21,542.

Peters, H., Baumert, H. Z., 2007. Validating a turbulence closure against estuarine microstructure measurements . Ocean Model. 19, 183–203.

Peters, H., Johns, W. E., 2005. Mixing and entrainment in the Red Sea outflow plume. Part II: Turbulence characteristics. J. Phys. Oceanogr. 35, 584–600.

Peters, H., Johns, W. E., Bower, A. S., Fratantoni, D. M., 2005. Mixing and entrainment in the Red Sea outflow plume. Part I: Plume structure. J. Phys. Oceanogr. 35, 569–583.

Prater, M. D., Rossby, T., 2005. Observations of the Faroe Bank Channel overflow using bottom-following RAFOS floats. Deep-Sea Res. II 52, 481–494.

Pratt, L. J., Helfrich, K. R., Leen, D., 2008. On the stability of ocean overflows. J. Fluid Mech. 602, 241–266.

Rahmstorf, S., 2002. Ocean circulation and climate during the past 120,000 years. Nature 419, 207–214.

Rahmstorf, S., England, M., 1997. Influence of Southern Hemisphere winds on North Atlantic Deep Water flow. J. Phys. Oceanogr. 27, 2040–2054.

Riemenschneider, U., Legg, S., 2007. Regional simulations of the Faroe Bank Channel overflow in a level model. Ocean Model. 17, 93–122.

Sandström, J. W., 1908. Dynamische Versuche mit Meerwasser. Ann. Hydrgr. Mar. Meteorol. 36, 6–23.

Sandström, J. W., 1916. Meteorologische Studien im Schwedischen Hochgebirge. Göteborgs K. Vetensk. Vitterhetssamhällets Handkl. 27, 48 pp.

Saunders, P. M., 1990. Cold outflow from the Faroe Bank Channel. J. Phys. Oceanogr. 1, 29–43.

Saunders, P. M., 1992. Combining hydrographic and shipborne ADCP measurements. Deep-Sea Res. 39, 1417–1427.

Seim, K. S., Fer, I., 2010. Mixing in the stratified interface of the Faroe Bank Channel overflow: the role of transverse circulation and internal waves. submitted to J. Geophys. Res.

Seim, K. S., Fer, I., Berntsen, J., 2010. Regional simulations of the Faroe Bank Channel overflow using a σ-coordinate ocean model. Ocean Model. 35, 31–44.

Sherwin, T. J., 2010. Observations of the velocity profile of a fast and deep oceanic density current constrained in a gully. J. Geophys. Res. 115, C03013.

Sherwin, T. J., Griffiths, C. R., Inall, M. E., Turrell, W. R., 2008. Quantifying the overflow across the Wyville Thomson Ridge into the Rockall Trough. Deep-Sea Res. I 55, 396–404.

Sherwin, T. J., Turrell, W. R., 2005. Mixing and advection of a cold water cascade over the Wyville Thompson Ridge. Deep-Sea Res. I 52, 1392–1413.

Shih, L. H., Koseff, J. R., Ivey, G. N., Ferziger, J. H., 2005. Parameterization of turbulent fluxes and scales using homogeneous sheared stably stratified turbulence simulations. J. Fluid Mech. 525, 193–214.

Swaters, G. E., 1991. On the baroclinic instability of cold-core coupled density fronts on a sloping continental-shelf. J. Fluid Mech. 224, 361–382.

Thorpe, S. A., 1977. Turbulence and mixing in a Scottish loch. Philos. T. R. Soc. A 286, 125–181.

Toggweiler, J. R., Samuels, B., 1998. On the ocean's large scale circulation in the limit of no vertical mixing. J. Phys. Oceanogr. 28, 1832–1852.

Turner, J. S., 1986. Turbulent entrainment - the development of the entrainment assumption, and its application to geophysical flows. J. Fluid Mech. 173, 431–471.

Umlauf, L., 2009. The description of mixing in stratified layers without shear in large-scale ocean models. J. Phys. Oceanogr. 39, 3032–3039.

Umlauf, L., Arneborg, L., 2009a. Dynamics of rotating shallow gravity currents passing through a channel. Part I: Observation of transverse structure. J. Phys. Oceanogr. 39, 2385–2401.

Umlauf, L., Arneborg, L., 2009b. Dynamics of rotating shallow gravity currents passing through a channel. Part II: Analysis. J. Phys. Oceanogr. 39, 2402–2416.

Umlauf, L., Burchard, H., Bolding, K., 2006. GOTM - Sourcecode and Test Case Documentation. Version 4.0.

Wåhlin, A. K., 2002. Topographic steering of dense currents with application to submarine canyons. Deep-Sea Res. I 49, 305–320.

Wåhlin, A. K., 2004. Downward channeling of dense water in topographic corrugations. Deep-Sea Res. I 51, 577–590.

Webb, D. J., Suginohara, N., 2001. Vertical mixing in the ocean. Nature 409, 37.

Paper I:

Intense mixing of the Faroe Bank Channel overflow

GEOPHYSICAL RESEARCH LETTERS, VOL. 37, L02604, doi:10.1029/2009GL041924, 2010

Intense mixing of the Faroe Bank Channel overflow

Ilker Fer,[1,2] Gunnar Voet,[3] Knut S. Seim,[4] Bert Rudels,[5,6] and Katrin Latarius[3]

Received 25 November 2009; revised 29 December 2009; accepted 5 January 2010; published 29 January 2010.

[1] The continuous, swift flow of cold water across the sill of the Faroe Bank Channel, the deepest passage from the Nordic Seas to the North Atlantic Ocean, forms a bottom-attached dense plume (overflow). The amount and distribution of entrainment and mixing that the overflow encounters during its descent influence the ventilation of the deep North Atlantic, however, remain poorly known due to lack of direct measurements. Using the first direct turbulence measurements, we describe the dynamic properties and mixing of the overflow plume as it descends toward the Iceland Basin. The vigorously turbulent plume is associated with intense mixing and enhanced turbulent dissipation near the bottom and at the plume-ambient interface, but with a quiescent core. Our measurements show a pronounced transverse circulation consistent with rotating plume dynamics, a strong lateral variability in entrainment velocity, and a vertical structure composed of order 100 m thick stratified interface and comparably thick well-mixed bottom boundary layer with significant transport and entrainment. **Citation:** Fer, I., G. Voet, K. S. Seim, B. Rudels, and K. Latarius (2010), Intense mixing of the Faroe Bank Channel overflow, *Geophys. Res. Lett.*, *37*, L02604, doi:10.1029/2009GL041924.

1. Introduction

[2] The export of cold, dense water from the Norwegian Sea through the Faroe Bank Channel (FBC, Figure 1) into the sub-polar North Atlantic accounts for about one third of the total overflow from the Nordic Seas [*Hansen and Østerhus*, 2007]. The FBC overflow, a bottom-attached gravity current, descends the sloping topography under the combined influence of pressure gradient, bottom friction and the Earth's rotation, and mixes with overlying water [*Saunders*, 2001; *Mauritzen et al.*, 2005]. The latter determines the end-product properties associated with the source water and needs to be properly represented in climate models for credible climate projections [*Legg et al.*, 2009]. Despite the importance of mixing of the FBC overflow, no previous measurements of turbulence have been available. Motivated by this lack of measurements we conducted such a survey in June 2008.

[1]Geophysical Institute, University of Bergen, Bergen, Norway.
[2]Bjerknes Centre for Climate Research, Bergen, Norway.
[3]Institute of Oceanography, University of Hamburg, Hamburg, Germany.
[4]Department of Marine Technology, Norwegian University of Science and Technology, Trondheim, Norway.
[5]Department of Physics, University of Helsinki, Helsinki, Finland.
[6]Finnish Meteorological Institute, Helsinki, Finland.

0094-8276/10/2009GL041924$05.00

2. Measurements and Data

[3] The obtained data set includes vertical profiles of hydrography and velocity from 63 casts with a conductivity-temperature-depth (CTD, SBE911+) package equipped with down and uplooking lowered acoustic Doppler current profilers (LADCPs, 300 kHz Workhorse), and of turbulence profiles from 90 casts with a vertical microstructure profiler (VMP, Rockland Sci. Int.). The VMP is equipped with accurate CTD sensors and a pair of microstructure shear probes used for measuring the dissipation rate of turbulent kinetic energy (ε). Turbulent shear is sampled at 512 Hz at a profiling speed of 0.6 m s^{-1}. Stations are occupied along the path of the overflow plume and along six sections starting from the sill crest (section A) to about 120 km downstream (section F, Figure 1a).

3. Technical Details

3.1 Currents, Dissipation Rate, and Eddy Diffusivity

[4] The velocity profile is calculated as 4 m vertical averages using the inverse method [*Visbeck*, 2002] constrained by accurate shipboard navigation and bottom tracking by the LADCP, and detided using a barotropic tidal model [*Egbert et al.*, 1994] for the European Shelf at 1/30° resolution. Tidal velocity is within 3 to 34% (18% on the average) of the maximum velocity at a given station.

[5] The profiles of ε are produced as 1 m vertical averages to a noise level of 10^{-10} W kg^{-1} [*Fer*, 2006]. The diapycnal eddy diffusivity is calculated using three different formulations: First, an upper limit is obtained from $K_\rho = 0.2\varepsilon N^{-2}$ [*Osborn*, 1980] assuming 17% mixing efficiency. $N = [-g/\rho(\partial\rho/\partial z)]^{1/2}$ is the buoyancy frequency, g is the gravitational acceleration, and ρ is density. Second, we use $K_\rho = 2\nu(\varepsilon / \nu N^2)^{1/2}$ [*Shih et al.*, 2005], suggested for $\varepsilon / \nu N^2 > 100$, valid for our data ($\nu$ is the viscosity). This formulation, inferred from direct numerical simulation results, has been supported by field data [*Fer and Widell*, 2007]. Third, we use a gradient Richardson number (Ri) dependent mixing efficiency with the range of parameters validated against microstructure measurements [*Peters and Baumert*, 2007]. Ri $= N^2/S^2$, where S is the shear. In all calculations, N is inferred from 4 m vertical gradients of sorted σ_θ (potential density referenced to nil pressure) profiles. The vertical scale is chosen to be consistent with shear calculations and the sorting approximates the background stratification against which the turbulence works.

3.2 Plume Properties and Stress

[6] The density anomaly, ρ', is obtained as deviations from an exponential background σ_θ profile fitted to observations excluding the plume. Velocity profiles are rotated into streamwise (u) and transverse (v, positive to the right of u) components with respect to the direction of the maximum

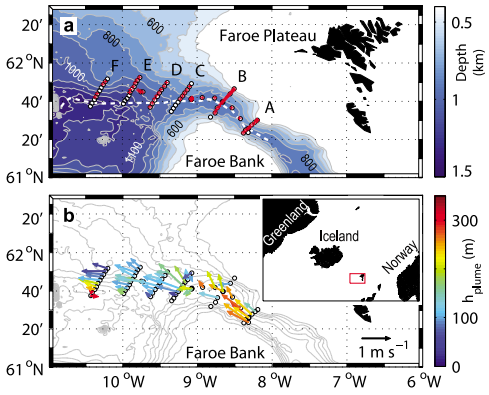

Figure 1. (a) Bathymetric contours drawn at 100 m intervals starting with 400 m, together with the thalweg (deepest point of the channel, white dashed line), sampling stations (CTD-LADCP, circles, and VMP, red crosses) and sections A to F. (b) Overflow velocity (arrows) averaged over h_{plume} (color). The salient features of the plume velocity and thickness are described in section 4. The inset shows the experiment location (red).

velocity (u_{nose}) in the bottom 200 m. The depth of the plume interface z_i and plume thickness h_{plume} are inferred from the $\sigma_\theta = 27.65$ kg m^{-3} isopycnal [*Mauritzen et al.*, 2005; *Girton et al.*, 2006]. The well-mixed bottom layer (BL) thickness is estimated as the height above bottom (HAB) where the density difference from the bottommost value exceeds 0.01 kg m^{-3}. The stratified interfacial layer (IL) is defined as the layer between the top of BL and the depth above the interface where $\partial\sigma_\theta/\partial z$ first drops below 5×10^{-4} kg m^{-4}. These thresholds robustly delineate the BL and IL. The calculation of integral plume properties and density-anomaly-weighted averages follows *Girton and Sanford* [2003]. The internal Froude number is calculated in two ways: from integral plume properties of each section using $\mathrm{Fr} = U/\sqrt{g'H}$ and using a two-layer formulation devised for transverse variations in velocity [*Pratt*, 2008]. In the former method g' is the reduced gravity, $H = A/(2W_{0.5})$ is the mean plume thickness for a section with area A and plume "half-width" $W_{0.5}$ [*Girton and Sanford*, 2003], and $U = Q_p/A$, using the section-integrated plume volume transport Q_p.

[7] The bottom shear stress, $\tau_b = \rho u_*^2$, is estimated using the friction velocity u_* from the slope of a linear fit of u against the log of HAB, assuming law of the wall (LOW). A series of fits is made for each profile, starting with 3 data points (12 m) and increasing to a maximum of BL thickness. The value with the least error, inferred from goodness of the fit, is chosen for analysis. The Ekman number $\mathrm{Ek} = u_*^2 / fuh_{plume}$ and the drag coefficient $C_D = u_*^2 / u_{nose}^2$ are obtained. Stress at the plume-ambient interface is estimated assuming a balance between the shear production, the dissipation rate, and the resulting buoyancy flux (0.2ε), as $\tau_i = 1.2\bar{\varepsilon}/(\rho\overline{du/dz})$, where overbars denote averaging over the interface thickness.

4. Results and Discussion

[8] The overflow plume descends the channel and the slope of the Iceland-Faroe Ridge with a typical speed of 0.5 – 1 m s^{-1}, reaching a maximum velocity of 1.35 m s^{-1} at section C (Figure 1b). Plume thickness averaged over stations is $h_{\mathrm{plume}} = 160 \pm 70$ m ($\pm$ 1 standard deviation, σ). Mean overflow thickness (H) inferred from section-integrated properties is between 110 m (section E) and 350 m (section B). All sections, however, show significant lateral variability (Figure 2).

[9] The vertical structure of the overflow is composed of a 70 ± 35 m thick well-mixed BL, overlaid by a 120 ± 60 m thick IL. With the caveat that the section-averaged transports are not synoptic with respect to variability on tidal and subtidal scales [*Geyer et al.*, 2006], the overflow is about equally distributed between the BL (0.9 ± 0.1 Sv, 1 Sv $\equiv 10^6$ m^3 s^{-1}) and the IL (1 ± 0.3 Sv). The presence of a thick IL was also observed at the Red Sea [*Peters et al.*, 2005], the Denmark Strait [*Girton and Sanford*, 2003], and the Mediterranean

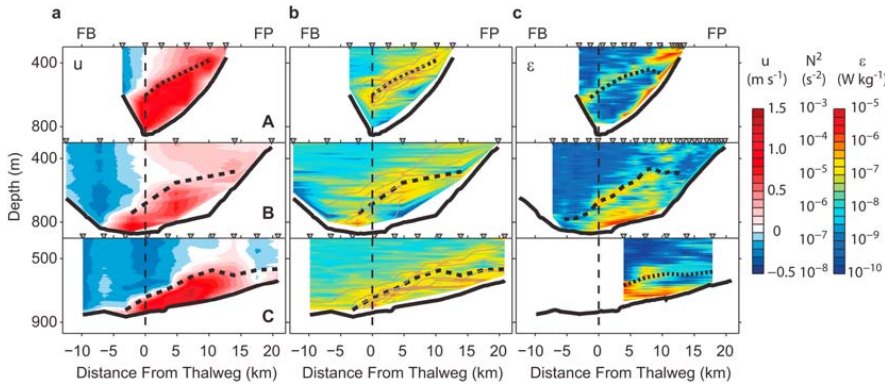

Figure 2. Contours of (a) downchannel velocity, u, (b) stratification, N^2 (color), and σ_θ at 0.1 kg m^{-3} intervals (gray), and (c) dissipation rate, ε, for sections A to C. Locations of the stations (triangles), the Faroe Bank (FB), and the Faroe Plateau (FP) are indicated. Dashed curves delineate the plume interface ($\sigma_\theta = 27.65$ kg m^{-3}).

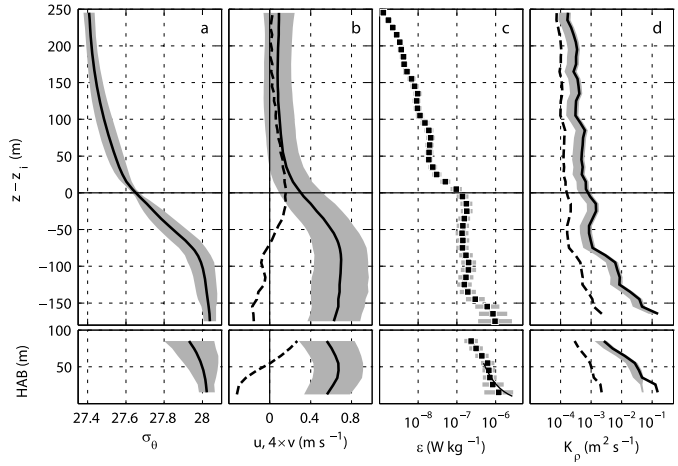

Figure 3. Survey averaged profiles of (a) σ_θ ($\pm$ 1σ, gray shading), (b) downchannel, u (solid line, $\pm$1σ, gray shading), and cross-channel, v (dashed line, multiplied by 4 for clarity), component of the velocity, (c) dissipation rate, ε (95% confidence limits, gray bars), and (d) eddy diffusivity, K_ρ, using *Osborn* [1980] (solid line), *Peters and Baumert* [2007] (gray), and *Shih et al.* [2005] (dashed line). Profiles are averaged in 10-m vertical bins referenced to (top) the interface depth, z_i, and to (bottom) bottom (HAB). Thin line in Figure 3c (bottom) is fit to LOW ($\varepsilon = u_*^3 / 0.4z$) in the bottom 55 m yielding u_* = 2.2 cm s^{-1} (τ_b = 0.5 Pa).

[*Price et al.*, 1993] outflow plumes, and suggests that bulk parameterization of entrainment [*Legg et al.*, 2009] devised for gravity currents with relatively thin interface may not be adequate.

[10] The velocity maximum is typically located deeper than the interface and is associated with weak ε as a result of weak shear production of turbulent kinetic energy (see the quiescent core at section A, Figure 2). This quiescent layer is present at all sections. The average thickness of layer with $\varepsilon < 10^{-8}$ W kg^{-1} below the interface is 40 m for the core stations and varies between 15 m (section B) and 60 m (section A). In the BL and the IL ε is exceptionally large, reaching 10^{-5} W kg^{-1} (Figure 2c). Typically BL is 20–70 m thicker than the bottom layer with enhanced dissipation. The vigorous turbulence near the bottom is due to stirring by the bottom shear stress. Enhanced mixing at the stratified and highly-sheared IL where Ri < 1 can be due to coexisting shear instabilities and internal wave-turbulence transition [*Baumert and Peters*, 2009] and vertical transport of turbulence [*Umlauf*, 2009]. The internal structure of turbulence in the FBC overflow is reminiscent of the observations in the Baltic Sea [*Umlauf et al.*, 2007], particularly the quiescent central region, and the asymmetry in ε at the sill section with enhanced ε where the interface intersects the Faroe Plateau slope (Figure 2b). A wedge-shaped interface, related to the secondary flow in the IL, as discussed by *Umlauf and Arneborg* [2009], is not resolved in our data set.

[11] Survey-averaged profiles are constructed for plume stations in 10-m thick bins relative to the interface and relative to the bottom (Figure 3). Due to variable interface depth and plume thickness, the average profiles cannot be combined (i.e., the lower part of Figure 3 (top) will not be consistent with Figure 3 (bottom) due to averaging). Dissipation rates, exceeding 10^{-7} W kg^{-1} in the plume, increase by one order of magnitude as the bottom is approached, consistent with LOW (thin line in Figure 3c). The mixing efficiency implied by the models of *Shih et al.* [2005] and *Peters and Baumert* [2007] differ significantly, particularly in weakly stratified layers (Figure 3d). The shear is strong throughout the IL, but the maximum in ε apparent in Figure 2c near the interface is smoothed out as a result of averaging. When calculated using the density and velocity profiles in Figure 3, Ri < 1 between 20 m above and 40 m below the interface, with a minimum value of 0.6 at 15 m below the interface. Ri < 1 in the entire BL with Ri < 0.25 in the bottommost 25 m. Low Ri in the BL is due to a combination of weak stratification and mean shear of the logarithmic velocity profile, whereas that in the IL is due to strong shear across the strongly stratified interface. Previous observations from a mooring near the FBC sill show frequent occurrence of low Ri in the IL, modulated by tidal and inertial flows [*Saunders*, 2001].

[12] The transverse velocity, v (Figure 3b), has a vertical structure consistent with the rotating gravity current dynamics [*Umlauf and Arneborg*, 2009]. Water in the IL is transported to the right, looking downstream (a transverse geostrophic transport due to the downchannel tilt of the plume interface), and water in the BL is transported to the left, consistent with an Ekman bottom boundary layer, leading to a flattening and broadening of the plume. Integrated across the IL and BL, the transverse flow approximately balances with 5 m^2 s^{-1} in the IL, −3.3 m^2 s^{-1} in the BL (−4.5 m^2 s^{-1} if an unresolved 15-m thick bottom layer with v = −8 cm s^{-1}, the bottommost average value, is included).

[13] The FBC overflow can be characterized by Fr between 0.5 and 1 and by Ek between 0.05 and 0.2; that is, the plume is thicker than the frictional boundary layer (Figure 4). In contrast to the Red Sea outflow [*Peters et al.*, 2005], the FBC overflow is significantly diluted in the BL. The buoy-

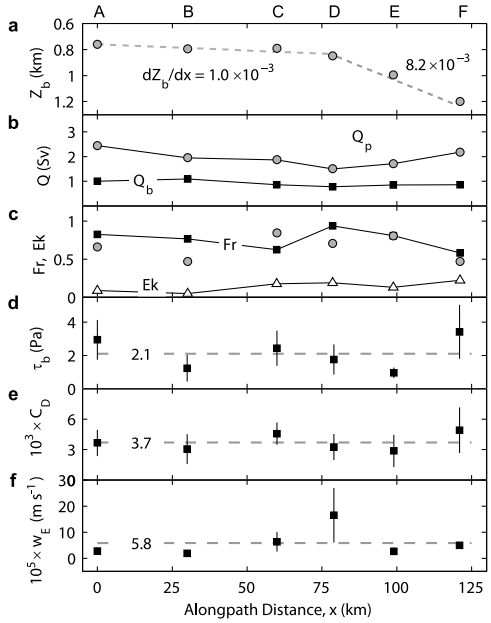

Figure 4. Downstream evolution of section-averaged properties. (a) Mass-anomaly-weighted depth of the plume, Z_b [*Girton and Sanford*, 2003]. Linear fits between sections A-D and D-F yield a descent rate of 1 m and 8.2 m per km along the path, respectively (dashed lines). (b) Volume transport in the overflow plume (Q_p, circles) and in the BL (Q_b, squares). (c) Froude number (Fr, following *Pratt* [2008], squares; and using section integral properties, circles), and Ekman number, Ek (triangles). (d) Bottom stress, τ_b, and (e) drag coefficient, C_D, from LADCP profiles, and (f) the entrainment velocity, w_E, from ε [*Arneborg et al.*, 2007]. The survey-averaged values are indicated by dashed lines. Error bars are $\sigma_e = \sigma\sqrt{n-1}$, where σ is the standard deviation and n is the number of plume stations in a section.

ancy averaged in BL (IL) increases by 1.4×10^{-3} m s^{-2} (5×10^{-4} m s^{-2}) on the first 80 km. This suggests entrainment into the BL, through, e.g., internal mixing in the plume, entrainment as a result of the transverse circulation, or lateral entrainment due to stirring by mesoscale eddies. The volume transport, however, is nearly constant in the BL (Q_b in Figure 4b), counterintuitive to the expected increase due to entrainment. Detrainment [*Baines*, 2005] might explain the lack of increase in Q_b. Nevertheless, interpreted together with the Red Sea outflow observations which show a similar vertical density structure but no dilution in BL, we suggest that the transverse circulation supplying the warmer interface water into the Ekman layer may cause the dilution in the BL. Q_b remains nearly constant due to the approximate lateral balance of the transverse circulation; that is, water entrained in the BL is transported back to the IL.

[14] Section-averaged K_ρ varies between $(2 - 10) \times 10^{-4}$ m^2 s^{-1} in the IL and between $(10 - 320) \times 10^{-4}$ m^2 s^{-1} in the BL, consistent with heat-budget considerations [*Saunders*, 1990; *Duncan et al.*, 2003]. The entrainment velocity, w_E, calculated from ε [*Arneborg et al.*, 2007] (assuming 17% mixing efficiency) varies by one order of magnitude laterally in each section (except section F). Section-averaged w_E increases fivefold from 3×10^{-5} m s^{-1} at the sill to 1.7×10^{-4} m s^{-1} at section D (Figure 4f) where Fr is accordingly at its highest, close to unity. The entrainment parameter, w_E/U, increases by one order of magnitude from 3.8×10^{-5} to 3.3×10^{-4}. The largest mixing and entrainment rates are observed at section D in the vicinity of the hot-spot of mixing identified by *Mauritzen et al.* [2005]. Detailed analysis of earlier observations suggests that FBC overflow is hydraulically controlled [*Girton et al.*, 2006] with the critical section (i.e., Fr = 1) located between 20 – 90 km down sill, comparing well with Fr $\approx$ 1 at our section D. While the overflow volume transport, Q_p, increases downstream of section D (consistent with enhanced entrainment), Q_p decreases between sections A and D. The mesoscale variability of the overflow makes the comparison of single sections complex.

[15] The overflow plume descends the slope as a result of bottom friction. The descent rate is relatively small between sections A-D and increases farther downstream (Figure 4a), comparable to that of the Denmark Strait plume [*Girton and Sanford*, 2003], but significantly larger than 2.5 m km^{-1} predicted by *Killworth* [2001]. The bottom stress $\tau_b = 2.1 \pm 0.4$ Pa, corresponding to a drag coefficient of $C_D = (3.7 \pm 0.4) \times 10^{-3}$, is large throughout the channel, and in the range of previous observations [*Mauritzen et al.*, 2005]. When tides are included, the survey-mean C_D increases by 20%. The average bottom stress inferred from the velocity profiles is about four times larger than that estimated from ε measurements near the bottom (Figure 3c), similar to observations from diverse sites and can be attributed to, e.g., the form drag. The stress at the IL is relatively weak, $\tau_i = 0.05 \pm 0.02$ Pa. Inferred from the balance of buoyancy, total drag (due to τ_b and τ_i) and Coriolis force acting on a slab of plume [*Girton and Sanford*, 2003], the total stress to account for the observed descent rates is 0.9 (sections A-D) and 4.9 Pa (D-F). Recalling that $\tau_b \approx \tau_b + \tau_i$ in our data set, Figure 4d does not show this trend, suggesting that the observed descent rates cannot be described by this simple force balance.

5. Concluding Remarks

[16] Our observations reveal the anatomy and mixing processes of the FBC overflow plume and add to our understanding of a highly sheared and stratified gravity current in a rotating system. The overflow plume is characterized by strong lateral variability in entrainment and mixing with a significant vertical structure including an about 100 m thick strongly-stratified interfacial layer. A transverse circulation actively dilutes the bottom layer of the plume. Neither the bulk entrainment parameterizations, mainly devised for non-rotating, two-layer gravity current plume dynamics, nor the traditional turbulence closure models will be adequate in representing mixing of the dense overflow plume downstream of the FBC sill.

[17] **Acknowledgments.** This study is funded by the Research Council of Norway, through Bipolar Atlantic Thermohaline Circulation (BIAC) project. Comments from an anonymous reviewer, L. Umlauf, H. Peters,

H. Z. Baumert, and T. Özgökmen are greatly appreciated. This is publication no. A 271 from the Bjerknes Centre for Climate Research.

References

Arneborg, L., V. Fiekas, L. Umlauf, and H. Burchard (2007), Gravity current dynamics and entrainment: A process study based on observations in the Arkona Basin, *J. Phys. Oceanogr.*, *37*, 2094–2113, doi:10.1175/JPO3110.1.

Baines, P. G. (2005), Mixing regimes for the flow of dense fluid down slopes into stratified environments, *J. Fluid Mech.*, *538*, 245–267, doi:10.1017/S0022112005005434.

Baumert, H. Z., and H. Peters (2009), Turbulence closure: Turbulence, waves and the wave-turbulence transition—Part 1: Vanishing mean shear, *Ocean Sci.*, *5*, 47–58.

Duncan, L. M., H. L. Bryden, and S. A. Cunningham (2003), Friction and mixing in the Faroe Bank Channel outflow, *Oceanol. Acta*, *26*, 473–486, doi:10.1016/S0399-1784(03)00042-2.

Egbert, G. D., A. F. Bennett, and M. G. G. Foreman (1994), TOPEX/POSEIDON tides estimated using a global inverse model, *J. Geophys. Res.*, *99*, 24,821–24,852, doi:10.1029/94JC01894.

Fer, I. (2006), Scaling turbulent dissipation in an Arctic fjord, *Deep Sea Res., Part II*, *53*, 77–95, doi:10.1016/j.dsr2.2006.01.003.

Fer, I., and K. Widell (2007), Early spring turbulent mixing in an ice-covered Arctic fjord during transition to melting, *Cont. Shelf Res.*, *27*, 1980–1999, doi:10.1016/j.csr.2007.04.003.

Geyer, F., S. Østerhus, B. Hansen, and D. Quadfasel (2006), Observations of highly regular oscillations in the overflow plume downstream of the Faroe Bank Channel, *J. Geophys. Res.*, *111*, C12020, doi:10.1029/2006JC003693.

Girton, J. B., and T. B. Sanford (2003), Descent and modification of the overflow plume in the Denmark Strait, *J. Phys. Oceanogr.*, *33*, 1351–1364, doi:10.1175/1520-0485(2003)033<1351:DAMOTO>2.0.CO;2.

Girton, J. B., L. J. Pratt, D. A. Sutherland, and J. F. Price (2006), Is the Faroe Bank Channel overflow hydraulically controlled? *J. Phys. Oceanogr.*, *36*, 2340–2349, doi:10.1175/JPO2969.1.

Hansen, B., and S. Østerhus (2007), Faroe Bank Channel overflow 1995–2005, *Prog. Oceanogr.*, *75*, 817–856.

Killworth, P. D. (2001), On the rate of descent of overflows, *J. Geophys. Res.*, *106*, 22,267–22,275, doi:10.1029/2000JC000707.

Legg, S., et al. (2009), Improving oceanic overflow representation in climate models: The Gravity Current Entrainment Climate Process Team, *Bull. Am. Meteorol. Soc.*, *90*, 657–670, doi:10.1175/2008BAMS2667.1.

Mauritzen, C., J. F. Price, T. B. Sanford, and D. Torres (2005), Circulation and mixing in the Faroese Channels, *Deep Sea Res., Part I*, *52*, 883–913, doi:10.1016/j.dsr.2004.11.018.

Osborn, T. R. (1980), Estimates of the local rate of vertical diffusion from dissipation measurements, *J. Phys. Oceanogr.*, *10*, 83–89, doi:10.1175/1520-0485(1980)010<0083:EOTLRO>2.0.CO;2.

Peters, H., and H. Z. Baumert (2007), Validating a turbulence closure against estuarine microstructure measurements, *Ocean Modell.*, *19*, 183–203, doi:10.1016/j.ocemod.2007.07.002.

Peters, H., W. E. Johns, A. S. Bower, and D. M. Fratantoni (2005), Mixing and entrainment in the Red Sea outflow plume. Part I: Plume structure, *J. Phys. Oceanogr.*, *35*, 569–583, doi:10.1175/JPO2679.1.

Pratt, L. J. (2008), Critical conditions and composite Froude numbers for layered flow with transverse variations in velocity, *J. Fluid Mech.*, *605*, 281–291, doi:10.1017/S002211200800150X.

Price, J. F., et al. (1993), Mediterranean outflow and mixing dynamics, *Science*, *259*, 1277–1282, doi:10.1126/science.259.5099.1277.

Saunders, P. M. (1990), Cold outflow from the Faroe Bank Channel, *J. Phys. Oceanogr.*, *20*, 29–43, doi:10.1175/1520-0485(1990)020<0029:COFTFB>2.0.CO;2.

Saunders, P. M. (2001), The dense northern overflows, in *Ocean Circulation and Climate,* edited by G. Siedler et al., pp. 401–417, Academic, San Diego, Calif.

Shih, L. H., J. R. Koseff, G. N. Ivey, and J. H. Ferziger (2005), Parameterization of turbulent fluxes and scales using homogeneous sheared stably stratified turbulence simulations, *J. Fluid Mech.*, *525*, 193–214, doi:10.1017/S0022112004002587.

Umlauf, L. (2009), The description of mixing in stratified layers without shear in large-scale ocean models, *J. Phys. Oceanogr.*, *39*, 3032–3039, doi:10.1175/2009JPO4006.1.

Umlauf, L., and L. Arneborg (2009), Dynamics of rotating shallow gravity currents passing through a channel. Part II: Analysis, *J. Phys. Oceanogr.*, *39*, 2402–2416, doi:10.1175/2009JPO4164.1.

Umlauf, L., L. Arneborg, H. Burchard, V. Fiekas, H. U. Lass, V. Mohrholz, and H. Prandke (2007), Transverse structure of turbulence in a rotating gravity current, *Geophys. Res. Lett.*, *34*, L08601, doi:10.1029/2007GL029521.

Visbeck, M. (2002), Deep velocity profiling using lowered acoustic Doppler current profilers: Bottom track and inverse solutions, *J. Atmos. Oceanic Technol.*, *19*, 794–807, doi:10.1175/1520-0426(2002)019<0794:DVPULA>2.0.CO;2.

I. Fer, Geophysical Institute, University of Bergen, N-5007 Bergen, Norway.

K. Latarius and G. Voet, Institute of Oceanography, University of Hamburg, D-20146 Hamburg, Germany.

B. Rudels, Department of Physics, University of Helsinki, FI-00561 Helsinki, Finland.

K. S. Seim, Department of Marine Technology, Norwegian University of Science and Technology, NO-7491 Trondheim, Norway.

Paper II:

Regional simulations of the Faroe Bank Channel overflow using a σ-coordinate ocean model

Ocean Modelling 35 (2010) 31–44

Contents lists available at ScienceDirect

Ocean Modelling

journal homepage: www.elsevier.com/locate/ocemod

Regional simulations of the Faroe Bank Channel overflow using a σ-coordinate ocean model

Knut S. Seim [a,*], Ilker Fer [b,c], Jarle Berntsen [d]

[a] Department of Marine Technology, Norwegian University of Science and Technology, O. Nielsens vei 10, Tyholt, 7491 Trondheim, Norway
[b] Geophysical Institute, University of Bergen, Allégaten 70, 5007 Bergen, Norway
[c] Bjerknes Centre for Climate Research, Allégaten 55, 5007 Bergen, Norway
[d] Department of Mathematics, University of Bergen, Johannes Brunsgate 12, 5008 Bergen, Norway

ARTICLE INFO

Article history:
Received 16 January 2010
Received in revised form 4 May 2010
Accepted 9 June 2010
Available online 1 July 2010

Keywords:
Dense overflow
Gravity current
Entrainment and mixing
σ-level model

ABSTRACT

Gravity-driven overflow of cold, deep and intermediate water from the Norwegian Sea through the Faroe Bank Channel carries significant volume flux and contributes to the ventilation of the deep North Atlantic Ocean. Here we present results from regional simulations of the Faroe Bank Channel overflow using a terrain-following (σ-coordinate) ocean model with fine resolution near the sea bed. The model results are compared with observations of hydrography, currents and turbulence conducted in 2008. Turbulent dissipation rate and eddy diffusivity profiles inferred from the observations are used in refining the parameters of the turbulence closure. The model reproduces the observed vertical structure of the enhanced dissipation and diffusivity in the bottommost 50–60 m exceptionally well. In this region, shear-induced mixing dominates and is found to be well-represented by the applied second order turbulence closure models. Farther away from the boundary, however, in the 100-m thick interfacial layer and above the plume-ambient interface, the model does not resolve the observed mixing. The contribution of turbulence from breaking internal waves is one of the processes not represented in the model with significant consequences for observed entrainment and mixing. Regular sub-inertial oscillations (eddies) at 4–4.5 day period develop downstream of the sill, consistent with the observations. When averaged over several eddy events, the evolution of section-averaged plume properties over the oscillation period shows that the eddies significantly affect mixing and the descent rate of the plume. At a section 60 km downstream of the sill, eddies lead to periodic and abrupt cross-isobath descent of the overflow plume and an increase in dissipation rate by one order of magnitude.

1. Introduction

Intermediate and deep water masses of the Greenland, Iceland and Norwegian Seas (collectively referred to as the Nordic Seas) flow through topographic constrictions and over shallow sills (termed 'overflow') across the Greenland–Scotland Ridge (GSR). The equatorward flow of this heavy water feeds the upper limb of the Atlantic meridional overturning circulation (MOC). While the overflow between Greenland and Iceland is through the Denmark Strait, east of Iceland, GSR consists of three distinct overflow regions (Fig. 1): the Iceland–Faroe Ridge (IFR), the Faroe Bank Channel (FBC), and the Wyville–Thomson Ridge (WTR) (Hansen and Østerhus, 2000). With a sill depth of 840 m, FBC is the deepest connection between the North Atlantic Ocean and the Nordic Seas. According to observations, the transport of overflow water across the GSR is about 6 Sv (1 Sv = 1×10^6 m^3 s^{-1}) (Hansen and Østerhus, 2000). The passages east of Iceland account for approximately half of the volume transport with 2.1 Sv across the FBC (Hansen and Østerhus, 2007), 1 Sv across the IFR (Perkins et al., 1998), and 0.3 Sv across the WTR (Sherwin et al., 2008). Hence, the FBC overflow constitutes about 30% of the total overflow.

The FBC overflow of dense, cold intermediate water from the Norwegian Sea forms a bottom-attached turbulent gravity current, mixing intensively as it descends across the Iceland–Faroe slope (Mauritzen et al., 2005; Fer et al., 2010). The mixing and entrainment associated with the plume set the hydrographic properties downstream of the sill, eventually contributing to the North Atlantic Deep Water production and the ventilation of the North Atlantic Ocean (Dickson and Brown, 1994). Since the importance of the FBC overflow for the exchange between the North Atlantic and the Nordic Seas was recognized by Cooper (1955), extensive studies of the FBC overflow were performed during NANSEN (Borenäs and Lundberg, 1988; Saunders, 1990, 1992) and the Nordic WOCE and VEINS (Hansen et al., 2001) programmes. Recent studies using

* Corresponding author. Tel.: +47 91378516.
E-mail addresses: knut.seim@ntnu.no (K.S. Seim), ilker.fer@gfi.uib.no (I. Fer), jarle.berntsen@math.uib.no (J. Berntsen).

1463-5003/$ - see front matter © 2010 Elsevier Ltd. All rights reserved.
doi:10.1016/j.ocemod.2010.06.002

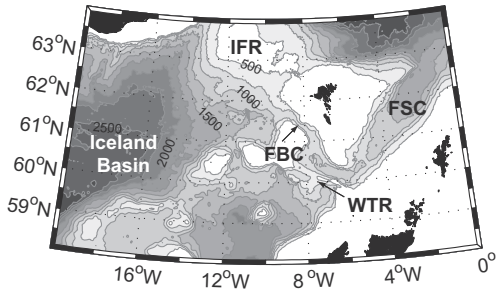

Fig. 1. Bathymetry of the channel system around the Faroe islands. Isobaths are drawn at 250-m intervals starting with 500 m. FBC: Faroe Bank Channel; FSC: Faroe Shetland Channel; WTR: Wyville–Thomson Ridge; and IFR: Iceland–Faroe ridge.

measurements from the FBC include Duncan et al. (2003), Mauritzen et al. (2005), Prater and Rossby (2005), Geyer et al. (2006), and Fer et al. (2010). The overflow water at the FBC sill can be characterized by a vertical temperature distribution composed of an about 100 m thick interface separating, on average, a 250 m thick deep cold ($T < 0°C$) layer from the overlying Atlantic Water. At its core, the mean overflow velocity is about 1 m s^{-1}. The volume transport of the overflow at the sill, inferred from continuous measurements from 1995 to 2005, is 2.1 Sv (Hansen and Østerhus, 2007). The volume transport inferred from cruise-duration observations is consistent, but highly variable (Duncan et al., 2003; Mauritzen et al., 2005). As the channel widens downstream of the sill, the overflow plume feels the steeper slope and descends under the influence of friction. Mauritzen et al. (2005) observe the highest velocities and levels of mixing approximately 100 km downstream of the sill and conclude that the hydrographic properties of the overflow are set within 100–150 km of the sill. The first direct turbulence measurements in FBC conducted in 2008, using a loosely tethered vertical microstructure profiler, show exceptionally large dissipation rates, reaching 10^{-5} W kg^{-1} near the bottom and at the interface of the overflow plume (Fer et al., 2010). The largest mixing and entrainment rates are observed in the vicinity of the hot spot of mixing identified by Mauritzen et al. (2005). Several threads of evidence from detailed analysis of observations suggest that the exchange at the sill, to the first order, is hydraulically controlled with a critical section between 20 and 90 km of the sill crest (Girton et al., 2006). This region is also associated with a widening of the plume, also apparent in Riemenschneider and Legg's (2007) model results. The widening of the plume is suggested to be associated with a transverse hydraulic jump (Pratt et al., 2007), however, conclusive observations are needed.

The FBC overflow is affected by regular sub-tidal variability. In situ observations downstream of the FBC sill show large temperature and current fluctuations of the overflow with a dominating period of 3.5 days (Høyer and Quadfasel, 2001). These fluctuations are associated with mesoscale eddies and have an impact on sea surface height. Geyer et al. (2006) report near-bottom velocity and temperature oscillations with a period of ~3.7 days observed between 75 and 140 km distance from the sill. A similar oscillation is reported by Ezer (2006) using highly idealized numerical simulations of the FBC overflow with a parabolic channel cross-section. Ezer (2006) identifies three different flow regimes resembling those found in the laboratory experiments of Cenedese et al. (2004): a sub-critical flow regime upstream of the FBC sill, a supercritical flow with strong mixing and entrainment from the sill to 100–200 km downstream ("wave" regime, reminiscent of the observations of roll-waves in Lake Geneva (Fer et al., 2001, 2002)), and the "eddy" regime farther downstream. Eddies apparent in observations, numerical simulations, and laboratory experiments might be due to the change in the channel curvature with downstream distance. For a zero-potential-vorticity flow in a parabolic channel with smooth topography, Pratt et al. (2008) show that the maximum growth rates and density of unstable wavenumbers increase for dynamically wider channels (decreasing curvature), and eddy generation downstream of the sill can occur solely by reducing the curvature in the downstream region.

In this study, we conduct regional simulations of the FBC overflow with an eddy-permitting σ-coordinate ocean model using different turbulence closures. New observations of hydrography, currents, and microstructure conducted in summer 2008 are compared with the model results. Turbulent dissipation rate and eddy diffusivity profiles inferred from the observations are used in refining the parameters of the turbulence closure. We adopt the domain and forcing applied in a recent study conducted with a z-level model (Riemenschneider and Legg, 2007, RL07, hereafter). This allows us to compare two inherently different models, particularly with respect to vertical mixing.

The aim of the study is, by using the model results and the observations in concert, to identify and improve the weaknesses of the model in representing the FBC overflow dynamics, mixing and entrainment, and to quantify the influence of oscillations on the plume descent rate and mixing. The numerical model, the turbulence closure, and the forcing are described in Section 2. The observational data set is summarized in Section 3. Subsequently, a comparison of the turbulence closures is given in Section 4, followed by a detailed comparison with observations in Section 5. The downstream evolution of the overflow volume transport, the plume path and its dynamics are presented. Low-frequency (4–4.5 days) oscillations seen in the model are supported by frequency-domain analysis of time series recorded by moored instruments and discussed using stability analysis. Further discussion (Section 6) include the model performance and the role of the mesoscale variability in enhanced descent rate and mixing of the overflow plume.

2. The numerical model

2.1. Bergen ocean model

In this study, we use the Bergen ocean model (BOM, Berntsen, 2000). BOM is a σ-coordinate (terrain-following) ocean model with non-hydrostatic capability. Considering the relatively low resolution applied here, the hydrostatic version of the model was chosen. The governing equations are the same as for the Princeton Ocean Model (POM) (Blumberg and Mellor, 1987; Mellor, 1996), but the numerical methods are different. For advection of momentum and density a TVD-scheme with a superbee limiter described in Yang and Przekwas (1992) is applied. The model is mode split with a method similar to the splitting described in Berntsen et al. (1981) and Kowalik and Murty (1993). The solution is propagated in time using single time step methods. For the depth-integrated momentum and continuity equations a predictor–corrector method is applied.

In σ-coordinate models the calculation of the internal pressure can introduce large errors near steep topography (Haney, 1991; Berntsen, 2002; Berntsen and Furnes, 2005). Mellor et al. (1994) showed, by studying the discretization error for the second-order internal pressure method used in POM, that the error will decrease with increasing the vertical and horizontal resolution. In Berntsen and Thiem (2007) and Berntsen and Oey (2009) it is shown that the internal pressure gradient errors may be further reduced by using the fourth order method suggested in McCalpin (1994). This fourth order method is applied in the present study. Running the model

with the FBC set-up used in this study without external forcing (inflow of dense water), the internal pressure is estimated to induce a flow over the sill of less than 1% of the mean forced overflow.

2.2. Turbulence model

Spurious mixing resulting from the step topography in z-coordinate models is eliminated by applying terrain-following coordinates. This makes it possible to introduce turbulence closure schemes in the vertical as opposed to RL07, who applied only numerical mixing in the vertical for the density and tracer, and a constant viscosity for the momentum. RL07 applied the Leith scheme (Leith, 1968, 1996) for the horizontal viscosity. For the present study the Smagorinsky scheme (Smagorinsky, 1963) has been applied. The Leith scheme has also been implemented, but no considerable difference was found between the two schemes. In the vertical, the Mellor and Yamada (1982) 2-1/2 level scheme (MY2.5), or alternatively the General Ocean Turbulence Model (GOTM, Umlauf et al., 2006), is applied to parameterize the subgrid-scale processes. In GOTM, a generic two-equation model for different turbulence closures (Umlauf and Burchard, 2003), has been implemented. The following equations are solved for the turbulent kinetic energy, k, and a generic variable, $\psi = \left(c_\mu^0\right)^p k^m l^n$,

$$\frac{\partial k}{\partial t} + u_i \frac{\partial k}{\partial x_i} = \frac{\partial}{\partial z}\left(\frac{K_m}{\sigma_k}\frac{\partial k}{\partial z}\right) + P + G - \varepsilon, \tag{1}$$

$$\frac{\partial \psi}{\partial t} + u_i \frac{\partial \psi}{\partial x_i} = \frac{\partial}{\partial z}\left(\frac{K_m}{\sigma_\psi}\frac{\partial \psi}{\partial z}\right) + \frac{\psi}{k}(c_1 P + c_3 G - c_2 \varepsilon), \tag{2}$$

where tensor notation is used. By changing the exponents p, m, and n, the different turbulence closure schemes are reproduced. ψ is used to calculate the turbulent length scale, l, using the coefficient c_μ^0 based on experimental data for unstratified channel flow with a log-layer solution (Warner et al., 2005). The coefficients c_1 and c_2 are selected consistent with von Karman's constant and with experimental observations for decaying homogeneous, isotropic turbulence (Wilcox, 2006). The parameter c_3 changes magnitude and sign: negative (c_3^-) and positive (c_3^+) for stable and unstable stratification, respectively. σ_k and σ_ψ are the turbulent Schmidt numbers for k and ψ, respectively. The shear and buoyancy production, P and G, can be expressed according to

$$P = -\langle u'w'\rangle \frac{\partial u}{\partial z} - \langle v'w'\rangle \frac{\partial v}{\partial z} = K_m M^2, \tag{3}$$

$$G = -\frac{g}{\rho_0}\langle \rho' w'\rangle = -K_h N^2, \tag{4}$$

where u and v are the mean horizontal velocity components and u', v', w' and ρ' are the turbulent fluctuations of the velocity and density components, g is the gravitational acceleration, ρ_0 is a reference density and

$$M^2 = \left(\frac{\partial u}{\partial z}\right)^2 + \left(\frac{\partial v}{\partial z}\right)^2, \quad N^2 = -\frac{g}{\rho_0}\frac{\partial \rho}{\partial z} \tag{5}$$

are the squared shear and the squared buoyancy frequency. With ψ from Eq. (2), the turbulent dissipation rate per unit mass, ε, can be computed according to

$$\varepsilon = \left(c_\mu^0\right)^{3+p/n} k^{3/2+m/n} \psi^{-1/n}. \tag{6}$$

Choosing appropriate values of p, m and n, a number of closure models can be recovered (e.g., k–ε, k–ω and MY2.5 ($k-l$), Warner et al., 2005). In this study, GOTM is set up for the k–ε and the k–ω turbulence closure models, and the MY2.5 scheme implemented in BOM is used. The eddy viscosity, K_m, and eddy diffusivity, K_h, are then computed as

$$K_m = c_\mu k^{1/2} l, \quad K_h = c'_\mu k^{1/2} l, \tag{7}$$

where c_μ and c'_μ are stability functions describing the effects of shear and stratification. A number of stability functions have been suggested. Here we use the Canuto-A (Canuto et al., 2001), for the k–ε and k–ω turbulence closures and Galperin et al. (1988) stability functions for the MY2.5 closure. Experimenting with different closures using different stability functions, Ilicak et al. (2008) find no discernible differences between k–ε and k–ω models with Canuto-A or Canuto-B stability functions when evaluated against the Red Sea outflow observations. The MY2.5 scheme with the Galperin stability function, however, produced too large eddy diffusivities.

2.3. Model set-up

The domain covers the Faroe Bank Channel system (the Faroe–Shetland Channel, the Wyville–Thomson Basin and the Faroe Bank Channel), the Iceland–Faroe Ridge, and the Iceland Basin (see Figs. 1 and 2). The domain, bathymetry and forcing are identical to RL07 for comparison with their simulations of the FBC overflow using the z-level model MITgcm. In this idealized simulation, the Coriolis parameter is constant and atmospheric forcing and tides are neglected. The bathymetry is a smoothed and gridded version of Smith and Sandwell (1997), kindly provided by S. Legg (personal communication, 2009). The topography is rotated 45° counterclockwise with respect to true north. In the vertical, there are 32 layers with increasing resolution toward the bottom, resulting in a vertical resolution averaged over the deepest five cells, of 2.2 m, 8.7 m and 21.8 m at 200 m, 800 m (comparable to the sill depth), and 2000 m, respectively. This allows for a better representation of the overflow at the expense of the surface layers. In the horizontal, the resolution is 2 km. All boundaries are closed except the northern entrance to the Faroe–Shetland Channel. Here, the dense water is introduced with a constant speed below a depth of 600 m using a flow relaxation scheme (FRS, Martinsen and Engedahl, 1987) such that the transport just outside the FRS-zone (across Section S1, Fig. 2) is between 2.5 and 2.7 Sv, consistent with RL07 who prescribed 2.6 Sv at the northern entrance. This inflow is counteracted by an outflow above a depth of 300 m. The density of the dense inflow is $\sigma_\theta = 28.07\ \mathrm{kg\,m^{-3}}$, marked with a passive tracer, τ, of unit concentration. Initially, the channel is filled with dense water ($\sigma_\theta = 28.07\ \mathrm{kg\,m^{-3}}$) below a depth of 825 m. The background stratification is identical to that in RL07 which is determined from observations of Mauritzen et al. (2005). This profile is based on a linear fit to the waters between the surface mixed layer and the bottom plume from a measured density profile reported in Mauritzen et al. (2005). When averaged between 200 and 1000 m depth, this linear background profile is $0.01\ \mathrm{kg\,m^{-3}}$ denser than the exponential background density profile obtained from our 2008 survey (Section 3) used in Fer et al. (2010). This difference is negligible and, to be consistent with RL07, we adopt their background profile. Our observations at Section A show an overflow plume density of $28.06\ \mathrm{kg\,m^{-3}}$. Using the linear background density profile, the density anomaly at 800 m depth is approximately $0.6\ \mathrm{kg\,m^{-3}}$. Hence the difference between our observations and the prescribed inflow forcing constitutes less than 2% of the density anomaly and is negligible. Again, to be consistent with RL07, we adopt their forcing of $28.07\ \mathrm{kg\,m^{-3}}$.

The data are stored for further analysis at Sections A–F (Fig. 2, identical to the observational sections) at 2 h intervals and at Sections S1–S4 at 9 min intervals. In total, four different runs have been executed using different turbulence closures summarized in Table 1. The first simulation, run0, is conducted with constant eddy viscosity of $2.0 \times 10^{-4}\ \mathrm{m^2\,s^{-1}}$ and zero eddy diffusivity, identical to RL07's control run. The other three runs, run1 to run3, employ second order turbulence closures.

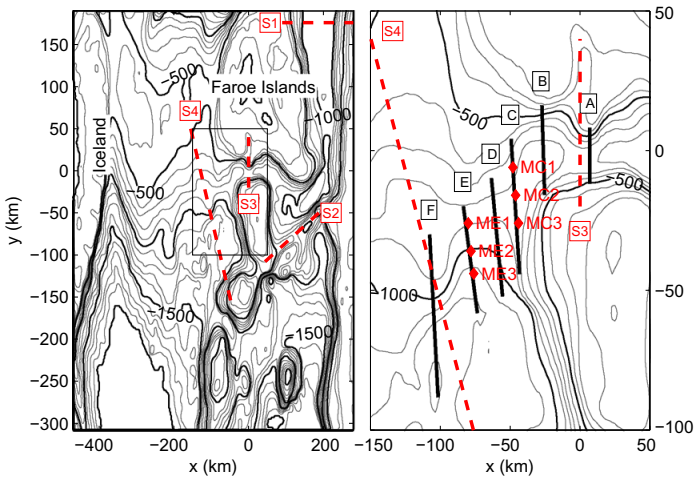

Fig. 2. Gridded topography of the domain with the origin located at the FBC sill. Red dashed lines mark the Sections S1–S4 where the volume transport is calculated. The rectangle marks the sill region with observation sections and the mooring locations shown in detail on the right. Sections A–F (black lines) correspond to the sections in Fer et al. (2010). Mooring locations MC1–MC3 and ME1–ME3 are shown by red diamonds.

Table 1
List of parameter settings for different numerical runs. The volume transport, Q, is given for Section S1. K_m and K_h are the eddy viscosity and diffusivity, respectively.

Run	Q (Sv)	K_m ($m^2\ s^{-1}$)	K_h ($m^2\ s^{-1}$)
run0	2.7	2.0×10^{-4}	0
run1	2.5	MY2.5	MY2.5
run2	2.5	k–ε	k–ε
run3	2.5	k–ω	k–ω

3. Observational data

Observations were made during a cruise of RV Håkon Mosby in early June 2008. Profiles of hydrography and currents were collected along six sections (marked A–F in Fig. 2). Additionally, turbulence in the water column was sampled using a loosely tethered vertical microstructure profiler (VMP2000, Rockland Scientific International). Details of the sampling and the instrumentation used are given in Fer et al. (2010). The data set includes 4 m vertical resolution horizontal velocity profiles and 1 m vertical resolution profiles of hydrography, dissipation rate of turbulent kinetic energy, and the eddy diffusivity. Observations from the ship are supplemented by time series of horizontal currents from moored instruments in the period from 14 May to 18 July 2008 covering the cruise period in 2008. Horizontal currents are sampled by Aanderaa Rotor Current Meters and RD-Instruments 300 kHz workhorse acoustic Doppler current profilers.

4. Comparison of turbulence closures

4.1. Transport

Following RL07, the boundary of the plume is prescribed by a cutoff concentration, $\tau = 0.1$, of the passive tracer. The volume transport of water with $\tau > 0.1$ through sections across the sill (S3), approximately 100 km downstream (S4) and across the WTR (S2) is calculated for each run (sections are marked by dashed lines in Fig. 2). The corresponding time series for each run is shown in Fig. 3. Additionally along plume transport is calculated by integrating the plume transport in the direction of the mean plume velocity through y-planes. Fig. 4 shows the along plume transport for all runs together with one standard deviation envelope for run2. The mean values at the sill and at 100 km downstream of

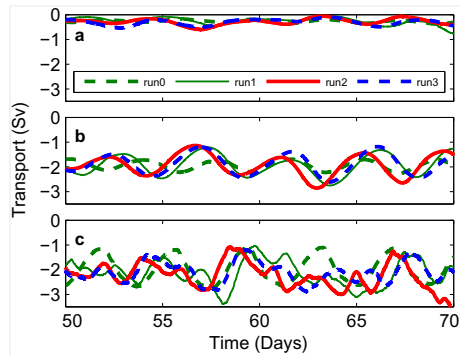

Fig. 3. Time series of volume transport through (a) Section S2 (across WTR), (b) the FBC sill section (S3), and (c) Section S4 approximately 100 km downstream of the sill for all runs.

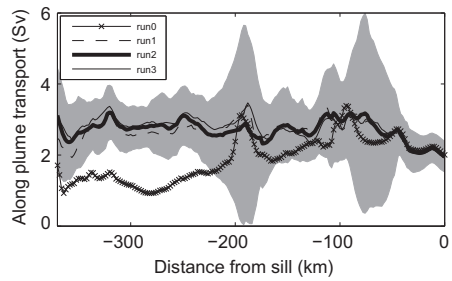

Fig. 4. Volume transport in the direction of the mean plume velocity through y-planes along the plume. The shading is ±1 standard deviation of the transport from run2.

the sill are tabulated in Table 2. The transport out of S4 is 0.6–0.8 Sv smaller than the along plume transport at $x = -100$ km, possibly due to positioning of the section where the bifurcation in the topography at Section S4 may cause the plume to diverge at this position.

The average dense water transport across the WTR section, approximately 0.3 Sv, is similar for all runs but run0 shows significantly less variability (Table 2). The transport over the FBC sill crest is one order of magnitude larger. The mean transport over the sill crest is approximately 2 Sv for all runs but the variability in the second-order closure runs, comparable to each other, is twice as large as in run0. From the sill to 100 km downstream the plume transport increases by 44–52% due to entrainment, with no discernible difference between the constant viscosity case (run0) and the second-order turbulence closures. However, the similarity between run0 and the other runs is only seen in the first 50 km and at ~100 and ~200 km which both coincides with local maxima in the constant viscosity case transport (Fig. 4). For the majority of the downstream part, the run0 transport is significantly lower compared with the other runs. In general the results from the second-order closures are similar; the difference between individual runs is insignificant compared with the variability.

Table 2
Observed volume transport with uncertainties and modelled volume transport with variability (1 std) of the overflow water at the sill crest, approximately 100 km downstream of the sill and at the Wyville–Thomson Ridge. The uncertainty (observations) and one standard deviation (models) are given when available.

	Sill	100 km	WTR
Observations			
Duncan et al. (2003)[a]	1.9	1.9	–
Mauritzen et al. (2005)	2.4 ± 0.2	3.6 ± 0.2	–
Hansen and Østerhus (2007)	2.1 ± 0.2	–	–
Fer et al. (2010)	2.4	2.2	–
Sherwin et al. (2008)	–	–	0.3
Models			
RL07	1.50 ± 0.27	2.38 ± 1.06	0.27 ± 0.16
run0	2.00 ± 0.18	2.92 ± 0.95	0.27 ± 0.05
run1	1.95 ± 0.43	2.88 ± 1.00	0.25 ± 0.14
run2	1.95 ± 0.44	2.97 ± 1.11	0.28 ± 0.12
run3	1.91 ± 0.42	2.75 ± 0.66	0.31 ± 0.11

[a] Volume transport of water with $T < 7$ °C. Downstream section is at about 81 km.

4.2. Plume path

The influence of turbulence closures on the path of the overflow plume is examined by comparing the tracer-weighted plume path

$$y(x) = \frac{\int y\tau(x,y,z)\,dy\,dz}{\int \tau(x,y,z)\,dy\,dz}, \tag{8}$$

time-averaged from day 50 to 70. Fig. 5 shows the plume path for different closure models, plotted over the topography. The plume paths are in general robust to the choice of second-order turbulence closure. The path from run0, however, clearly separates from the corresponding paths for the other runs at approximately 50–100 km downstream of the sill which stands out as an important section for the mixing of the overflow with the ambient water. Farther downstream, the path for run0 is shallower and higher up on the slope. In run0 the constant vertical viscosity is weak and results in a reduced Ekman layer thickness and consequently less downslope transport of dense water.

4.3. Turbulence and mixing

The mean values and the variability of the eddy diffusivity, K_h, and the dissipation rate, ε, for runs 1–3 are tabulated in Table 3 for the interface region (within ±50 m of the overflow plume interface) and for the bottommost 90 m. The largest difference is seen in K_h in the vicinity of the interface where the diffusivity varies within a factor of three between the runs. The variability is largest in run1, however, in all runs the variability greatly exceeds the mean value, emphasizing the intermittent nature of mixing in the interface. The latter is also true for ε. In the interface, the mean and standard deviation of ε vary within a factor of two between the runs, less than that in K_h. Remarkably, in the bottommost 90 m ε is identical between runs. The results are found to be not very sensitive to the choice of the turbulence closure, in agreement with Ilicak et al. (2008). Also consistent with Ilicak et al. (2008) the MY2.5 scheme (run1) leads to larger K_h, particularly for the stratified interface region.

As a result of the similarities in diffusivity, dilution of the time-averaged and tracer-weighted plume density is comparable for runs 1–3 (Fig. 6). Tracer-weighted density is calculated according to

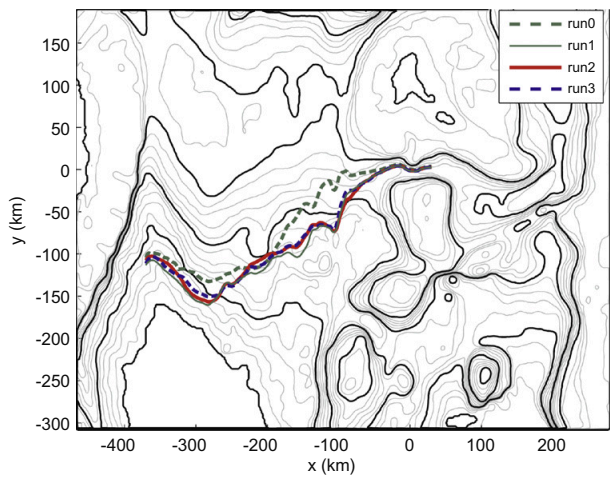

Fig. 5. Average tracer-weighted plume path (Eq. (8)) for different runs. Isobaths are drawn at 100 m intervals with every 500 m shown with thick traces.

Table 3
Mean and standard deviation of the vertical eddy diffusivity and the dissipation rate of TKE within ± 50 m of the overflow plume interface and in the bottommost 90 m derived for the three runs using different second order closures. Observed values with uncertainties are also given.

	K_h ($m^2\ s^{-1}$)		ε ($W\ kg^{-1}$)	
	Mean	SD	Mean	SD
$z_i \pm 50$ m				
Observed	8.7×10^{-4}	4.0×10^{-4}	1.0×10^{-7}	0.7×10^{-7}
run1	2.9×10^{-4}	13.5×10^{-4}	0.9×10^{-8}	2.6×10^{-8}
run2	1.7×10^{-4}	5.9×10^{-4}	1.4×10^{-8}	5.5×10^{-8}
run3	0.7×10^{-4}	2.4×10^{-4}	0.7×10^{-8}	2.5×10^{-8}
0–90 m HAB				
Observed	$(0.6 \pm 0.5) \times 10^{-1}$		$(7.0 \pm 3.0) \times 10^{-7}$	
run1	1.1×10^{-1}	0.8×10^{-1}	1.3×10^{-6}	1.1×10^{-6}
run2	0.8×10^{-1}	0.5×10^{-1}	1.3×10^{-6}	1.0×10^{-6}
run3	0.9×10^{-1}	0.7×10^{-1}	1.3×10^{-6}	1.0×10^{-6}

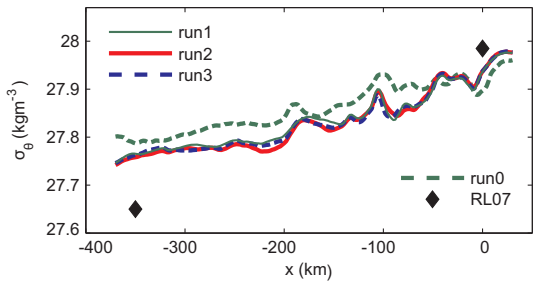

Fig. 6. Average tracer-weighted plume density. Black diamonds are values from Riemenschneider and Legg (2007) (from their Fig. 12(b) and Fig. 13).

$$\rho(x) = \frac{\int \rho\tau(x,y,z)\,dy\,dz}{\int \tau(x,y,z)\,dy\,dz}, \tag{9}$$

and then averaged in time (from day 50 to 70). In run0 the plume dilutes relatively less downstream of 50 km than the plumes produced in other runs. The plume densities in the last three experiments are consistent. Having established that second-order closures behave similarly, we compare the density fields at selected sections between run0 and run3. These sections correspond to the observational sections to facilitate the comparison with Section 5.2 (Fig. 8). The density in Fig. 7 is averaged over the period from day 50 to 70. The mean and variability (one standard deviation over the 20 days) of the position of the $\sigma_\theta = 27.65\ kg\ m^{-3}$ surface is also shown (see Section 5.2). After crossing the sill in the Faroe Bank Channel, the overflow is confined by the steep topography in the channel (Sections A and B), and about 50 km downstream of the sill, the plume descends the Faroe–Iceland slope (Sections C and F). Downstream of the sill, run3 gives a thicker plume interface and higher variability compared with run0, while at the sill the constant vertical viscosity in run0 leads to a diffusive interface.

5. Comparison with observations

In the following, we use the results from run2 to compare with the observational data.

5.1. Transport

Compared with observations, the modelled transport at the sill is within 20% of the observed transports (Table 2). The increase in transport between the sill and the section downstream at 100 km is approximately 50%, comparable to Mauritzen et al. (2005). Observations of both Duncan et al. (2003) and Fer et al. (2010) are undersampled with respect to the low-frequency variability and comparison of volume transport between individual sections is not representative of the entrainment and mixing. Overall observations reveal large variability of about 1 Sv from one occupation of the section to the next (see Mauritzen et al. (2005)). Like the oscillations downstream of the sill, the oscillations with a period of 4–4.5 days in the transport at the sill, clearly visible in Fig. 3, is also supported by observations (Saunders, 1990; Hansen and Østerhus, 2007) reporting variation with a period of 3–6 days.

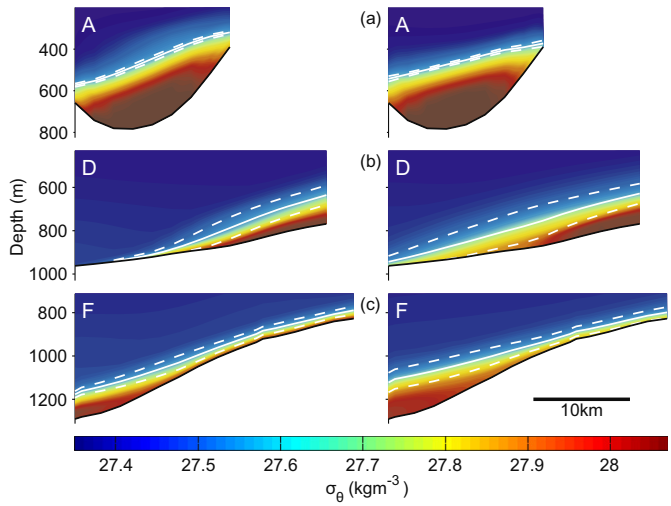

Fig. 7. Time-averaged (days 50–70) density from run0 (left column) and run3 (right column) at (a) Section A, (b) Section D and (c) Section F. The white solid line is the $\sigma_\theta = 27.65\ kg\ m^{-3}$ isopycnal, used to identify the plume in observations. One standard deviation of the interface position over the averaging period is marked by the broken lines.

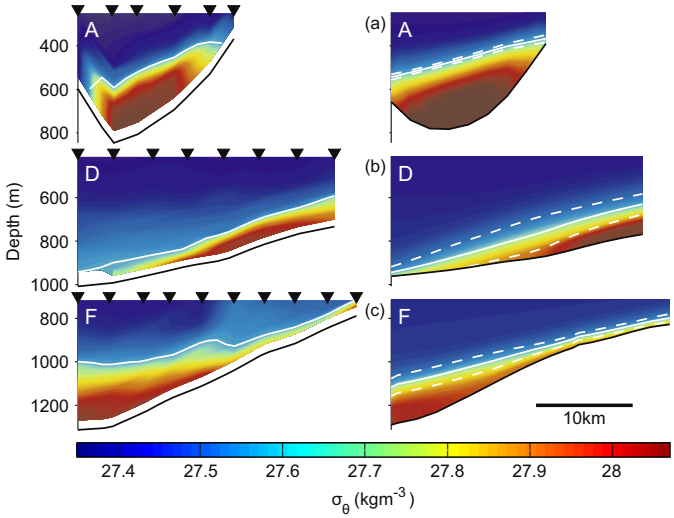

Fig. 8. Observed density (left column) and time-averaged (days 50–70) density from the model, run2, at (a) Section A, (b) Section D and (c) Section F (right column). The white solid line is the $\sigma_\theta = 27.65$ kg m^{-3} isopycnal, used to identify the plume in observations. For the model results, one standard deviation of the interface position over the averaging period is marked by the broken lines.

5.2. Density sections

Observed distribution of density is compared with density from the model run2 at the corresponding sections averaged over day 50-70 (Fig. 8). The daily averaged sections of the modelled plume have a core comparable to the observations, but with a relatively thin interface layer between the relatively well-mixed bottom layer and the ambient (not shown). Because of the inherent variability in the overflow plume, instantaneous observation-model section comparison is not conclusive (there are times when the agreement is excellent or poor). We therefore compare the model sections that are averaged over 20 days and illustrate the mean and variability (one standard deviation over the 20 days) of the position of the $\sigma_\theta = 27.65$ kg m^{-3} surface (Fig. 8). In this representation, the interface thickness is large as a result of averaging, not representative of the daily averages or snapshots. With increasing downstream distance, the observations show an increasingly diluted interface. This dilution is not captured by the model and, together with direct comparisons in Section 5.3, shows the lack of sufficient mixing at the interfacial layer in the σ-coordinate model.

5.3. Turbulence and mixing

The survey-averaged vertical profiles of observed density, along plume velocity, dissipation rate and the diapycnal eddy diffusivity reported in Fer et al. (2010) are compared with the model results (Fig. 9). The averaging is done for plume stations (with $\sigma_\theta > 27.65$ kg m^{-3}), relative to the plume interface and relative to the bottom (height above bottom, HAB). Vertical averaging length relative to the interface is 10 m for the observations and 25 m for the model data. Relative to the bottom, the model has sufficient vertical resolution, and the averaging bin length is set to 10 m for both the observations and the model. In general, the model reproduces the observed vertical structure reasonably well. The discrepancies, especially in density and velocity near the bottom, are likely partly due to the averaging in time, but they are also affected by the undersampling in observations. The relatively slow flow of light and thin plume higher on the slope extending for tens of kilometers (see, e.g., Section F in Fig. 8) bias the model HAB-average profiles.

In the bottommost 60 m the turbulent closure performs exceptionally well (lower panels in Fig. 9c and d). However, in the interior of the plume, the model overestimates the dissipation rate and the eddy diffusivity by up to one order of magnitude. Above the interface, both the dissipation rate and the vertical eddy diffusivity drop rapidly to levels well below the observations. This is due to the unresolved processes in the interfacial layer and discussed in Section 6.

The diffusivity and dissipation for different runs can be compared with the observed values (all listed in Table 3). The observed values are significantly larger than the model values in the interface region ($z_i \pm 50$ m). Unfortunately the measurements cannot be used to evaluate the performance of different closures because the uncertainty in ε is a factor of two and that in K_ρ can be as large as a factor of 4, greater than the differences between the closures. Furthermore, bottom averages in observations do not cover the bottommost 10 m where enhanced ε is expected.

5.4. Hydraulic control

Results from direct measurements of turbulence (Fer et al., 2010) and mixing inferred from overturning length scales Mauritzen et al. (2005) conclude that the largest mixing and entrainment rates are observed in the hot spot between 60 and 100 km from the sill. A detailed analysis of observations suggest that the exchange at the sill, to the first order, is hydraulically controlled with a critical section between 20 and 90 km of the sill crest (Girton et al., 2006). The Froude number can be used to judge hydraulic criticality. Following RL07, the local Froude number of the flow is defined as

$$\mathrm{Fr} = \frac{U}{\sqrt{g' d}}, \tag{10}$$

where d is the thickness of the plume, U is the vertically averaged plume velocity and g' is the reduced gravity defined as

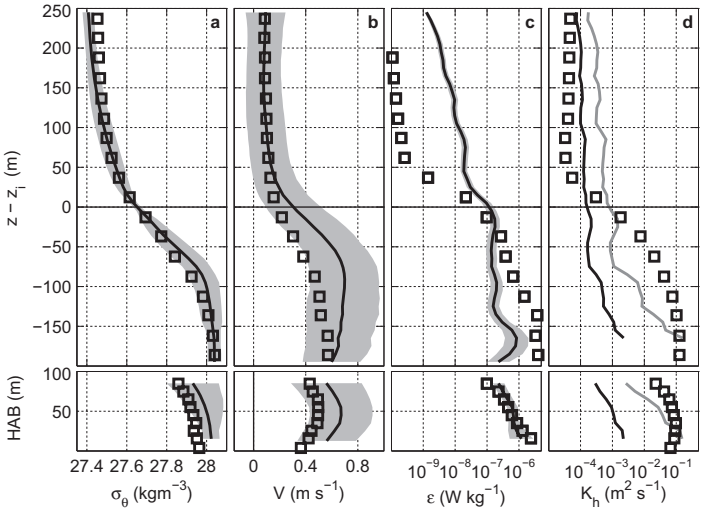

Fig. 9. Vertical profiles of observed (solid lines) and modelled (squares) (a) density σ_θ, (b) along plume velocity, V, (c) dissipation rate, ε, and (d) the eddy diffusivity, K_h, averaged in vertical bins with respect to the interface position $z - z_i$ (upper panels) and with respect to the height above bottom, HAB (lower panels). The bin length is 10 m for the observations and the HAB panels of the model data whereas 25 m for $z - z_i$ panels of the model data. The shading in the observations is ±1 standard deviation. The observed profiles of the eddy diffusivity in (d) are inferred from dissipation rate measurements using constant mixing efficiency (gray line) and the formulation of Shih et al. (2005) (black line) (see Fer et al. (2010) for details).

$$g' = g\frac{\frac{1}{d}\int_0^d(\rho(z)-\rho_{amb})\,dz}{\rho_0} \tag{11}$$

where ρ_{amb} and ρ_0 are the ambient density (in the layer above the boundary of the plume) and a reference density. The Froude number is then averaged in the y-direction, weighted by the area of the plume cross-section at location y at time t

$$\mathrm{Fr}(x,t) = \frac{\int \mathrm{Fr}(x,y,t)d(y,t)\,dy}{\int d(y,t)\,dy}, \tag{12}$$

where $d(y,t)$ is the depth of the plume. In Fig. 10a, the Froude number along the plume, averaged in the y-direction is shown for run2. Another measure of the Froude number is the composite, two-layer Froude number, G_w (Pratt, 2008) defined by

$$G_w^2 = \frac{1}{\frac{1}{w_I}\int_0^w \frac{g'D_1}{V_1^2}\,dx} + \frac{1}{\frac{1}{w_I}\int_{x_L}^{x_R} \frac{g'D_2}{V_2^2}\,dx}, \tag{13}$$

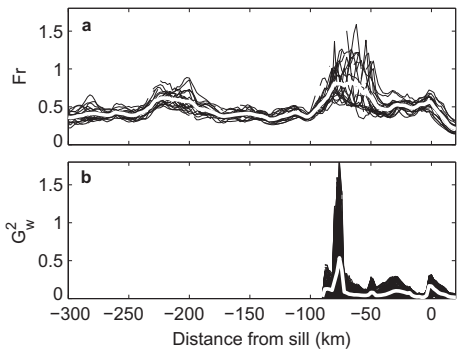

Fig. 10. (a) Froude number (Eq. (10)) along the plume for run2 applying the k–ε turbulence model. (b) The composite Froude number, G_w^2, (Eq. (13)) calculated along the overflow only to a downstream distance of 90 km. $G_w^2 = 1$ is the critical condition for the flow.

where w_I is the width $x_R - x_L$ of the interface between the two layers and w is the width at top of the upper layer (see Fig. 1 of Pratt (2008)). Here $D_{1,2}$ and $V_{1,2}$ are the thickness and the velocity of the two layers. The condition for the hydraulic criticality of a two layer flow with transverse variations in both layer velocities and thickness is given by $G_w^2 = 1$. We calculate G_w^2 from 30 km upstream of the sill to 90 km downstream (Fig. 10b). Frequent occurrence of $G_w^2 \geqslant 1$ at about 80 km downstream of the sill crest suggests that the flow is hydraulically controlled by a critical section there, in agreement with Girton et al. (2006). This location is also in remarkable agreement with Fer et al. (2010) who obtain $G_w^2 \sim 1$ at Section D with significant entrainment velocity and increase in the descent rate of the plume.

5.5. Oscillations

Highly regular sub-inertial oscillations have been previously observed in the near-bottom current meter records downstream of the FBC sill crest (Geyer et al., 2006). Both earlier numerical simulations (Ezer, 2006; Riemenschneider and Legg, 2007) and our transport time series at different sections (Fig. 3) show similar oscillations. The data from moored instruments (Section 3) are used to present frequency domain descriptions from Sections C and E with three moorings each, located close to, upslope, and downslope of the core, respectively. We note that the observations reported by Geyer et al. (2006) are within 5–30 m from the bottom whereas our measurements show, for the first time, the presence of the oscillations up to 200 m HAB (the height of the mooring). The frequency spectra (Fig. 11) for the along slope velocity component calculated at different heights above the bottom from current measurements at moorings MC1–MC3 (Section C) and ME1–ME3 (Section E) show elevated energy levels at frequencies corresponding to periods between 80 and 114 h (3.3–4.8 days). The energy typically increases from the upslope side of the overflow to the downslope side in both sections. This is in accordance with the model results showing the largest variability at the downslope side of the overflow. While the MC array of moorings have oscillations dominating at about 114 h period, the ME array contains more var-

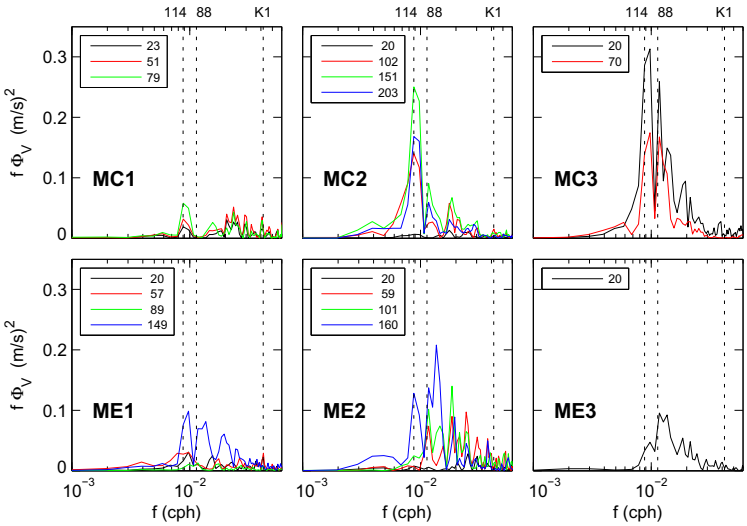

Fig. 11. Variance-preserving frequency spectra for the along slope velocity component calculated from moored current measurements at moorings (upper panels) MC1–MC3 and (lower panels) ME1–ME3. Frequency, *f*, is in cycles per hour (cph). Spectra are shown for selected height above the bottom given in legends. Dashed lines mark 114 h, 88 h, and the K1 tidal period.

iance at shorter periods. For moorings 1 and 2 of each array, the energy is generally increasing with height above bottom, but in MC3 the highest energy levels, both at the mooring location and for the whole section, are found at the bottommost current meter. For ME3, data are available only 20 m above bottom. Although not encountering the highest levels of the ME array, the energy level inferred from this current meter is significantly higher compared with the other bottom current meters at this mooring array and is close to the maximum levels. The variance enhanced in the highlighted frequency bands typically vanishes in the bottommost current meter records, likely as a consequence of the frictional boundary layer.

The oscillation period in the model is about 4–4.5 days (run2), comparable to the observations. In Fig. 12 the time versus along-path evolution of the overflow density at the plume interface is shown. The period of 4–4.5 days is apparent and most prominent between approximately 50 and 100 km downstream of the sill. This corresponds to the area where the overflow exits the channel and enters the Faroe–Island slope (50 km downstream), and a bifurcation in the topography approximately 100 km downstream resulting in a more complex flow structure. From the sill and 50 km downstream, the overflow is confined within the Faroe Bank Channel constituting a different flow regime compared with the flow on the slope. In Fig. 13 this is illustrated by plotting the mean height of the plume (averaged from day 50 to 70) and its variation over one oscillation period at positions 28, 60, and 80 km downstream of the sill.

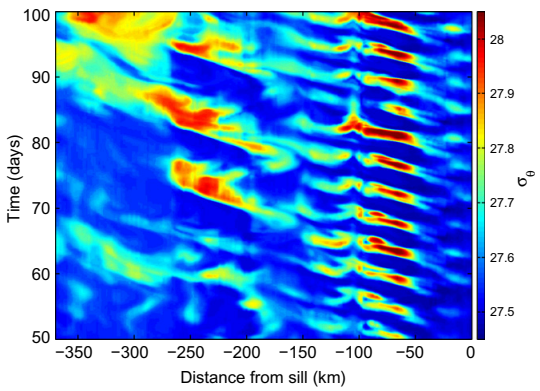

Fig. 12. Density at the time-averaged position of the plume interface, defined by $\tau = 0.1$, along the mean position of the plume on the slope plotted against time. The section ends at the FBC sill ($x = 0$ km).

6. Discussion

6.1. Model performance

The overflow of dense water through the Faroe Bank Channel and onto the Faroe–Iceland slope is studied using the σ-coordinate ocean model, BOM. Despite the unresolved topography and bottom roughness, which influences the mixing and entrainment in a dense overflow (Özgökmen and Fischer, 2008), the mixing in the bottom boundary layer is found to be in remarkable agreement with direct measurements of turbulence. However, compared with the observations, the level of turbulence and mixing is too low in the interfacial layer and in the stratified layer above the overflow (Section 5.3). In the vicinity of the plume-ambient interface, the model diffusivity decreases rapidly from enhanced values in the bottom layer by up to three orders of magnitude (Fig. 9). Initial test runs, not reported in this paper, resulted in significantly less mixing in the interface and above. Guided by the observed profiles, we prescribed a minimum TKE level of 5×10^{-7} m^2 s^{-2} to compensate for the unresolved processes, and constrained the turbulent length scale (Galperin et al., 1988). Without this limitation on the length scale and the TKE, the dissipation rate and the vertical eddy viscosity drop to minimum levels immediately above the overflow. This may be due to unresolved processes in the interfacial layer and the lack of tides in the model. The second order turbulence closure models employed here compute the turbulent diffusivity as a func-

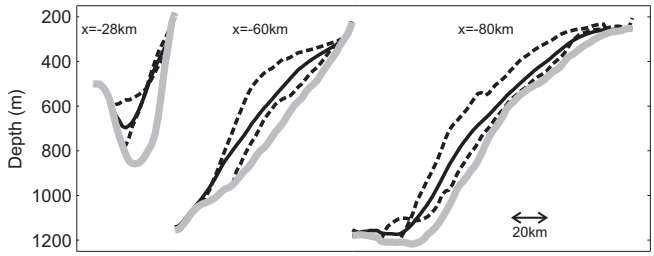

Fig. 13. The extent of the plume defined by $\tau = 0.1$ at sections 28, 60 and 80 km downstream of the sill crest. The solid black line is the mean plume thickness from day 50 to 70 and the dashed lines are the maxima and minima over one oscillation period. The solid grey line is the bottom.

tion of the gradient Richardson number, $\mathrm{Ri} = N^2/M^2$, where the buoyancy frequency, N, and shear, M, are defined in Eq. (5). Mixing will collapse for Ri greater than a finite critical threshold, typically less than unity. Data from various sources (see Canuto et al., 2008, and references cited therein) including our own measurements point toward significant mixing for Ri > 1, and considerable advances are made in developing models with no finite critical Ri (Canuto et al., 2008; Umlauf, 2009). The shear production of TKE in layers with large Ri can be, for example, due to the vertical transport of TKE from neighboring regions by turbulent motions (Umlauf, 2009) or due to the presence of internal waves (Baumert and Peters, 2009). According to Baumert and Peters (2009), for 0.25 > Ri > 0.5, both shear instability and internal wave-turbulence transition will coexist and contribute to mixing. The lack of sources of mixing for large Ri is clearly a deficiency of the model.

The grid size, especially in the horizontal, used in the present set of studies is too coarse to capture the transports of TKE, to represent internal waves, and the mixing due to these processes (Bergh and Berntsen, 2009; Berntsen et al., 2009). One should also bear in mind that in exercises like the present, the small scale (subgrid scale) topography is not captured, and the associated form drag, wave drag, and mixing are not parameterized (see for instance Lott and Miller (1997)). Using the observed average vertical profiles of density and velocity given in Fig. 9, Fer et al. (2010) infer Ri between 0.6 and 1 in the entire interfacial layer and less than unity in the entire bottom boundary layer (with Ri < 0.25 in the bottommost 25 m), at scales comparable to the vertical resolution of the model. Observations also show a pattern with enhanced ε in the interface where the stratification is also enhanced (Fer et al., 2010), indicating possible influence of internal wave induced mixing. It is noteworthy that the model profiles of dissipation and diffusivity in the bottommost 25 m, where observations suggest Ri < 0.25, capture the observations, hence the turbulence closures perform satisfactorily when the TKE generation mechanism is resolved.

6.2. Comparison with RL07

A shortcoming of ocean circulation models is their representation of dense overflows from polar and marginal seas and the associated entrainment and mixing processes. Particularly z-level models at coarse resolution excessively mix the hydrographic properties of the overflows as a result of the step topography. In a regional simulation study of the FBC overflow, RL07 has shown that a traditional z-level ocean model can simulate the FBC overflow reasonably well when zero vertical diffusivity and a constant vertical viscosity are prescribed. They found, however, the amount of mixing to be very sensitive to the grid resolution and to the vertical viscosity. Due to the advection scheme, numerical diffusion mixes the advected tracer field to preserve smoothness. This leads, fortuitously, to mixing in places that coincide with large shear and Froude numbers. In our σ-coordinate model, the small scale noise due to the steps in the topography for the z-level model is reduced and state-of-the-art turbulence closures are implemented. In our simulations mixing in the interface between the plume and the ambient is weaker, for all runs, compared with both the results from the z-level model and with the observations. This is likely due to unresolved processes at the interface (Bergh and Berntsen, 2009; Berntsen et al., 2009, see Section 6.1) and may be improved by increased horizontal resolution or parameterization of these processes.

Average transport is contrasted to model results of RL07 in Table 2. The transport at the sill is within 20% of the observed transports, in better agreement than the z-level set-up that underestimates the transport at the sill by up to 40%. The increase in along plume transport from the sill crest to 100 km downstream is about 10% lower than that in RL07, demonstrating the lower mixing in our simulations. This is also evident in the average tracer-weighted density reduction downstream of the sill, clearly lower, by about 50% from the sill to $x = -350$ km, in our simulations compared with RL07's results.

The along-path evolution of the Froude number is comparable to that inferred from the level model. Both models show similarly elevated Fr within approximately 100 km downstream from the sill, particularly between 50 and 80 km where the time mean value reaches 0.76 for run2 and 0.50 for run0 (same set up as RL07's control run). Downstream of 200 km, the Froude numbers produced with the present σ-coordinate model are smaller than those in RL07, and they lack the corresponding trend.

6.3. Does the mesoscale variability affect the descent rate and mixing?

To illustrate how the low-frequency variability of the overflow affects the dynamics and mixing of the plume, an ensemble average over oscillation events during the period from day 50 to 70 is calculated at two selected sections, 28 and 60 km downstream of the sill, in the channel and on the slope, respectively (see Fig. 13 for sections showing the topography). For the averaging, data are extracted in 6-day windows centered at times of local transport maximum events. The average and the variability over ensembles of the plume thickness, the bottom depth at the tracer weighted position of the overflow and the section-averaged dissipation rate are displayed in Fig. 14. The amplitude of the bottom depth oscillations of the plume core position (i.e., the tracer weighted position) is about 50 m at the section closest to the sill and by more than 100 m at the section farthest downstream. In the channel ($x = -28$ km), the plume covers the deepest part of the section at all times (see Fig. 13), hence the tracer-weighted bottom depth does not vary significantly. On the slope, on the other hand, eddies lead to periodic cross-isobath descent of the dense water deeper on

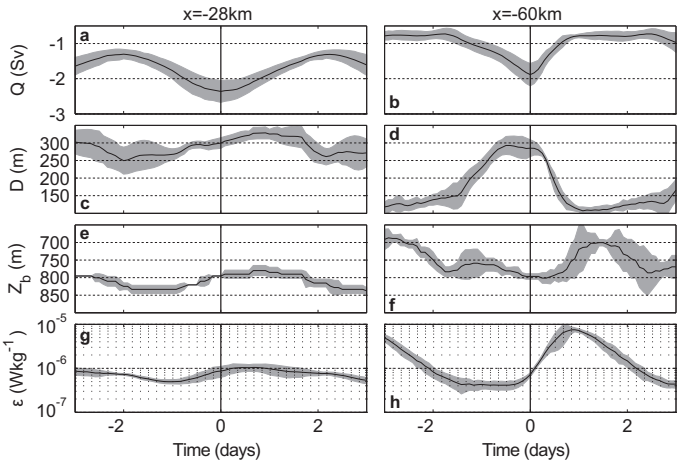

Fig. 14. Ensemble averages of (a and b) the overflow transport, Q, (c and d) overflow thickness, D, (e and f) bottom depth at the tracer integrated position of the overflow, Z_b, and (g and h) the dissipation rate averaged over the section, over the oscillations between day 50 and 70 for sections at (left panels) $x = -28$ km and (right panels) $x = -60$ km.

the slope. Overall, this leads to a descent rate (see Fig. 15) which cannot simply be explained by the balance of buoyancy, drag and the Coriolis force acting on a slab of plume as discussed in Fer et al. (2010). The dissipation rate is also clearly affected by the oscillations changing by more than a factor of 2 and 10 for the section at 28 and 60 km downstream of the sill, respectively.

The regular oscillations are a prominent feature of the FBC overflow and are very important for the mixing of the overflow. The regularity of the oscillations decreases as the overflow leaves the FBC and enters the Iceland–Faroe slope. Similar oscillations are observed elsewhere, e.g., in the Filchner overflow, Antarctica (Darelius et al., 2009), the Denmark Strait overflow (Käse et al., 2003). It is difficult to pinpoint a single mechanism causing the oscillations. Pratt et al. (2008) have shown that the change in curvature of a hydraulically controlled channel flow alone can lead to such variability. Results from a detailed stability analysis (Appendix A) are not conclusive, but indicate that downstream of the sill the most unstable mode has a typical wavelength greater than 40 km. The growth rate increases with decreasing curvature of the channel with an indication of increased periods at approximately 70 km downstream of the sill.

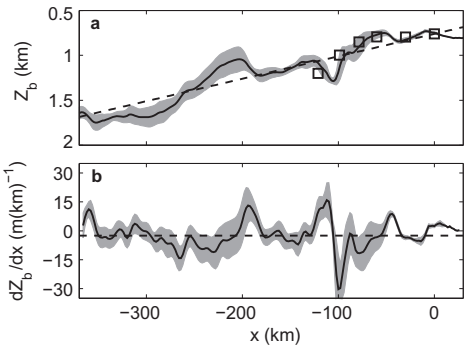

Fig. 15. Downstream evolution of (a) bottom depth at the tracer weighted position of the overflow and (b) the descent rate of the plume, dZ_b/dx along the plume path. The squares in (a) are the observed values reported in Fer et al. (2010). The dashed lines correspond to a descent rate of 1/400 (Killworth, 2001).

7. Summary

Regional simulations of the dense overflow through the Faroe Bank Channel and along the Faroe–Island slope are conducted using the σ-coordinate Bergen ocean model with idealized forcing in the absence of wind and tides. Results are compared with observations of hydrography, currents and turbulence conducted in 2008 (Fer et al., 2010). The observations comprise shipboard data (profiles of horizontal velocity, hydrography, dissipation rate of turbulent kinetic energy, and eddy diffusivity), and 2-month long time series of horizontal currents from moored instruments. The simulations comprise four runs including one with constant eddy viscosity and followed by three experiments with second-order closure models (MY2.5, k–ε and k–ω). The terrain-following coordinate system is suitable for overflow modelling. It eliminates the numerical mixing problem induced by the step topography of z-level models, and allows for introducing state-of-the-art turbulence closure models. Barring the constant eddy viscosity run, the results are found to be robust to the choice of the turbulence model.

In general, the model reproduces the salient features of the overflow plume reasonably well. The transport at the sill is within 20% of the observed transports (Hansen and Østerhus, 2007), in better agreement than a recent z-level model study (Riemenschneider and Legg, 2007) that underestimates the transport at the sill by up to 40%. The dissipation rate and eddy diffusivity dictated by the turbulent closure in the bottommost 60 m compare exceptionally well with the direct turbulence measurements. In this range, the gradient Richardson number is small and the production of turbulent kinetic energy is well resolved. In the interior of the plume, the model overestimates the dissipation rate and the eddy diffusivity by up to one order of magnitude. Turbulence then drops rapidly in the interfacial layer to levels well below the observations. This is due to the unresolved processes in the interfacial layer where the Richardson number is around unity. Entrainment, judged from the increase in volume transport from the sill region to 100 km downstream is weaker for all runs when compared with the observations and the results from the z-level model. The lack of

entrainment emphasizes the importance of unresolved mixing in the interface.

The region between 50 and 100 km downstream of the sill crest is found to be important for the mixing and entrainment of the overflow water with the adjacent water masses. Here, the two-layer composite Froude number (Pratt, 2008) frequently exceeds unity, suggesting a critical section for hydraulic control of the flow, in agreement with Girton et al. (2006). This location is also identified as a hot-spot for mixing and entrainment both from turbulent overturn analysis (Mauritzen et al., 2005) and from direct turbulence measurements (Fer et al., 2010).

The model develops low-frequency oscillations between 50 and 100 km downstream of the sill, where the overflow exits the channel and enters the Faroe–Island slope. The oscillations have a period of about 4–4.5 day. These eddies are also seen in the simulations of Riemenschneider and Legg (2007) and Ezer (2006) and are comparable to the observations from moored instruments reported here, covering up to 200 m from the bottom. The period is slightly longer than the 3.7 day observed in the near bottom (within 20 m from the bottom) current records (Geyer et al., 2006). The regular oscillations have a strong impact on the mixing and the descent rate. They are associated with periodic rapid cross-isobath descent of the plume and with enhanced levels of dissipation rate that will lead to strong mixing with ambient water masses as the plume enters the Faroe–Island slope. Similarly enhanced mixing and rapid descent can be expected in other major overflows which manifest comparable mesoscale eddies and low frequency fluctuations (e.g., Filchner outflow, Antarctica, Darelius et al., 2009 and Denmark Strait overflow, Käse et al., 2003).

Acknowledgements

We thank U. Riemenschneider and S. Legg for kindly providing the bathymetry and forcing they used in their simulations of the Faroe Bank Channel overflow. We also thank two anonymous reviewers whose comments have significantly improved the paper. This work is funded through the Academia agreement between the Norwegian University of Science and Technology and Statoil ASA, and partly by the Research Council of Norway, through the Bipolar Atlantic Thermohaline Circulation (BIAC) project.

Appendix A. Stability analysis

The shallow water equations for a vertically integrated dense overflow plume are:

$$\begin{aligned}
&\frac{\partial u}{\partial t}+u\frac{\partial u}{\partial x}+v\frac{\partial u}{\partial y}-fv=-g'\frac{\partial}{\partial x}(b+d),\\
&\frac{\partial v}{\partial t}+u\frac{\partial v}{\partial x}+v\frac{\partial v}{\partial y}+fu=-g'\frac{\partial}{\partial y}(b+d),\\
&\frac{\partial d}{\partial t}+\frac{\partial}{\partial x}(ud)+\frac{\partial}{\partial y}(vd)=0,
\end{aligned} \tag{14}$$

where the Cartesian coordinate system (x,y) is oriented with the x-axis along the direction of the along plume flow and the y-axis across the overflow plume. u and v are current components along the x- and y-directions, respectively, d is the overflow plume depth, $b = b(y)$ is the undisturbed bottom elevation, f is the Coriolis parameter, and g' the reduced gravity, $g' = g(\Delta\rho/\rho_0)$, where g is the acceleration of gravity, $\Delta\rho$ the difference in density of the overflow and the ambient water, and ρ_0 a reference density.

To investigate the stability, perturbations are introduced to the steady flow:

$$\begin{aligned}
u&=\bar{u}+u',\\
v&=v',\\
d&=\bar{d}+d',
\end{aligned}$$

where $\bar{u}$ and $\bar{d}$ are the initial velocity and plume depth, respectively. We assume a steady, geostrophically balanced along channel flow, $\bar{u}=\bar{u}(y)$, and a locally negligible along channel variation of the mean plume depth, i.e., $\bar{d}=\bar{d}(y)$. Substitution into the shallow water Eqs. (14) and linearization gives:

$$\begin{aligned}
&\frac{\partial u'}{\partial t}+\bar{u}\frac{\partial u'}{\partial x}+v'\frac{d\bar{u}}{dy}-fv'=-g'\frac{\partial d'}{\partial x},\\
&\frac{\partial v'}{\partial t}+\bar{u}\frac{\partial v'}{\partial x}+fu'=-g'\frac{\partial d'}{\partial y},\\
&\frac{\partial d'}{\partial t}+\bar{u}\frac{\partial d'}{\partial x}+\bar{d}\frac{\partial u'}{\partial x}+v'\frac{d\bar{d}}{dy}+\bar{d}\frac{\partial v'}{\partial y}=0.
\end{aligned} \tag{15}$$

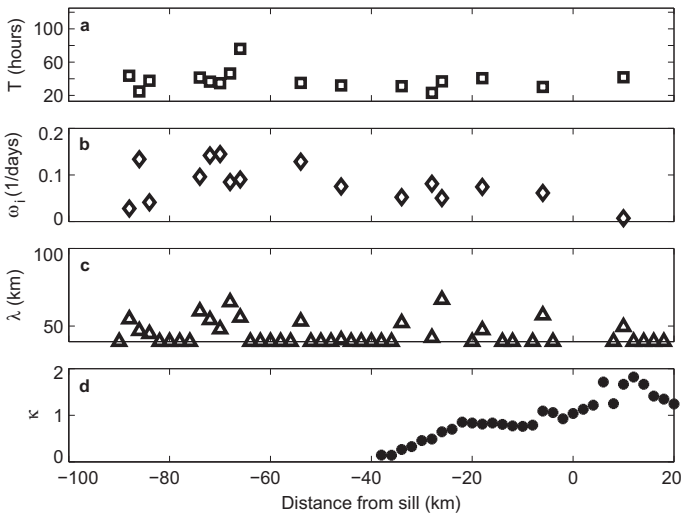

Fig. 16. Downstream evolution of (a) period, (b) growth rate, (c) the wave length of the most unstable modes from stability analysis, and (d) the non-dimensional cross-channel curvature from parabolic fit to the topography.

We are interested in the stability and thus search for normal modes of the form

$$\begin{aligned} u' &= \hat{u}(y)\cos(kx-\omega t),\\ v' &= \hat{v}(y)\sin(kx-\omega t),\\ d' &= \hat{d}(y)\cos(kx-\omega t), \end{aligned} \tag{16}$$

where k is a real wave number, ω the angular velocity, and the phase speed is given by $c = \omega/k$, the wave length $\lambda = 2\pi/k$, and the period $T = 2\pi/\omega$. Substitution into the linearized equations for the perturbations gives:

$$\begin{pmatrix} g'k & \bar{u}k & f-\frac{d\bar{u}}{dy}\\ g'\frac{d}{dy} & f & \bar{u}k\\ \bar{u}k & \bar{d}k & -\frac{d}{dy}\bar{d} \end{pmatrix}\begin{pmatrix}\hat{u}\\ \hat{v}\\ \hat{d}\end{pmatrix} = \omega\begin{pmatrix}\hat{u}\\ \hat{v}\\ \hat{d}\end{pmatrix}. \tag{17}$$

This represent an eigenvalue problem for ω given a wavenumber k and the steady, geostrophically balanced (assumed) velocity field, $\bar{u}$, and thickness, $\bar{d}$, of the overflow. The problem (Eq. (17)) is solved for ω by discretizing in the y-direction with central differences on a space staggered grid.

Fig. 16 shows the period, growth rate and wavelength of the most unstable mode. The lower panel in Fig. 16 shows a non-dimensional measure of the cross-channel curvature (Pratt et al., 2008), $\kappa = 2\alpha g'/f^2$, where α is the coefficient of a parabolic fit to the channel geometry. At approximately 30 km downstream of the sill the channel widens and the parabolic fit gradually fails, thus the curvature is only calculated until 40 km downstream of the sill. In 21 out of 71 sections a mode with higher growth rate at short wavelengths appeared which we exclude by setting a lower limit on the wavelengths of 40 km (indicated in Fig. 16 by a wavelength of 40 km, but no growth rate or period). As the plume flows along the slope, the complex flow structure is associated with increasing variability including occasional reversal or nearly stagnant plume on the deep side of the slope. Due to this irregular flow, the numerically solved stability analysis which requires fairly smooth plume thickness and velocity structure becomes more uncertain.

References

Baumert, H.Z., Peters, H., 2009. Turbulence closure: turbulence, waves and the wave-turbulence transition. Part 1: vanishing mean shear. Ocean Sci. 5, 47–58.

Bergh, J., Berntsen, J., 2009. Numerical studies of wind forced internal waves with a non-hydrostatic model. Ocean. Dynam. 59, 1025–1041.

Berntsen, J., 2000. Users guide for a modesplit σ-coordinate numerical ocean model. Tech. Rep. 135, Department of Applied Mathematics, University of Bergen, Johs. Bruns gt.12, N-5008 Bergen, Norway, 48p.

Berntsen, J., 2002. Internal pressure errors in sigma-coordinate ocean models. J. Atmos. Ocean. Technol. 19, 1403–1414.

Berntsen, J., Furnes, G., 2005. Internal pressure errors in sigma-coordinate ocean models – sensitivity of the growth of the flow to the time stepping method and possible non-hydrostatic effects. Cont. Shelf Res. 25, 829–848.

Berntsen, J., Oey, L.-Y., 2009. Estimation of the internal pressure gradient in σ-coordinate ocean models: comparison of second-, fourth-, and sixth-order schemes. Ocean Dynam. Online First, doi:10.1007/s10236-009-0245-y.

Berntsen, J., Thiem, Ø., 2007. Estimating the internal pressure gradient errors in a σ-coordinate ocean model for the Nordic Seas. Ocean Dynam. 57, 417–429.

Berntsen, H., Kowalik, Z., Sælid, S., Sørli, K., 1981. Efficient numerical simulation of ocean hydrodynamics by a splitting procedure. Model. Ident. Control 2, 181–199.

Berntsen, J., Xing, J., Davies, A.M., 2009. Numerical studies of flow over a sill: sensitivity of the non-hydrostatic effects to the grid size. Ocean. Dynam. 59, 1043–1059.

Blumberg, A., Mellor, G., 1987. A description of a three-dimensional coastal ocean circulation model. In: Heaps, N. (Ed.), Three-Dimensional Coastal Ocean Models, Coastal and Estuarine Series, vol. 4. American Geophysical Union, pp. 1–16.

Borenäs, K.M., Lundberg, P.A., 1988. On the deep-water flow trough the Faroe-Bank Channel. J. Geophys. Res. 93, 1281–1292.

Canuto, V.M., Cheng, A.H., Dubovikov, M.S., 2001. Ocean turbulence. Part I: one-point closure model-momentum and heat vertical diffusivities. J. Phys. Oceanogr. 31, 1413–1426.

Canuto, V.M., Cheng, Y., Howard, A.M., Esau, I.N., 2008. Stably stratified flows: a model with no Ri(cr). J. Atmos. Sci. 65, 2437–2447.

Cenedese, C., Whitehead, J.A., Ascarelli, T.A., Ohiwa, M., 2004. A dense current flowing down a sloping bottom in a rotating fluid. J. Phys. Oceanogr. 34, 188–203.

Cooper, L.H.N., 1955. Deep water movements in the North Atlantic as a link between climatic changes around Iceland and biological productivity of the English Channel and Celtic Sea. J. Mar. Res. 14, 347–362.

Darelius, E., Smedsrud, L.H., Østerhus, S., Foldvik, A., Gammelsrød, T., 2009. Structure and variability of the Filchner overflow plume. Tellus 61A, 446–464.

Dickson, R., Brown, J., 1994. The production of North-Atlantic deep water – sources, rates and pathways. J. Geophys. Res. 99 (C6), 12319–12341.

Duncan, L.M., Bryden, H.L., Cunningham, S.A., 2003. Friction and mixing in the Faroe Bank Channel outflow. Oceanol. Acta 26, 473–486.

Ezer, T., 2006. Topographic influence on overflow dynamics: idealized numerical simulations and the Faroe Bank Channel. J. Geophys. Res. 111. doi:10.1029/2005JC003195.

Fer, I., Lemmin, U., Thorpe, S.A., 2001. Cascading of water down the sloping sides of a deep lake in winter. Geophys. Res. Lett. 28, 2093–2096.

Fer, I., Lemmin, U., Thorpe, S.A., 2002. Winter cascading of cold water in Lake Geneva. J. Geophys. Res. 107. doi:10.1029/2001JC000828.

Fer, I., Voet, G., Seim, K.S., Rudels, B., Latarius, K., 2010. Intense mixing of the Faroe Bank Channel overflow. Geophys. Res. Lett. 37, L02604. doi:10.1029/2009GL041924.

Galperin, B., Kantha, L.H., Hassid, S., Rosati, A., 1988. A quasi-equilibrium turbulent energy model for geophysical flows. J. Atmos. Sci. 45, 55–62.

Geyer, F., Østerhus, S., Hansen, B., Quadfasel, D., 2006. Observations of highly regular oscillations in the overflow plume downstream of the Faroe Bank Channel. J. Geophys. Res. 111. doi:10.1029/2006JC003693.

Girton, J.B., Pratt, L.J., Sutherland, D.A., Price, J.F., 2006. Is the Faroe Bank Channel overflow hydraulically controlled? J. Phys. Oceanogr. 36, 2340–2349.

Haney, R.L., 1991. On the pressure gradient force over steep topography in sigma coordinate ocean models. J. Phys. Oceanogr. 21, 610–619.

Hansen, B., Østerhus, S., 2000. North Atlantic–Nordic Seas exchanges. Prog. Oceanogr. 45, 109–208.

Hansen, B., Østerhus, S., 2007. Faroe Bank Channel overflow 1995–2005. Prog. Oceanogr. 75, 817–856.

Hansen, B., Turrell, W.R., Østerhus, S., 2001. Decreasing overflow from the Nordic Seas into the Atlantic Ocean through the Faroe Bank Channel since 1950. Nature 411, 929–930.

Høyer, J.L., Quadfasel, D., 2001. Detection of deep overflows with satellite altimetry. Geophys. Res. Lett. 28 (8), 1611–1614.

Ilicak, M., Özgökmen, T.M., Peters, H., Baumert, H.Z., Iskandarani, M., 2008. Performance of two-equation turbulence closures in three-dimensional simulations of the Red Sea overflow. Ocean Modell. 24, 122–139.

Käse, R.H., Girton, J.B., Sanford, T.B., 2003. Structure and variability of the Denmark Strait overflow: model and observations. J. Geophys. Res. 108 (C6). doi:10.1029/2002JC001548.

Killworth, P.D., 2001. On the rate of descent of overflows. J. Geophys. Res. 106 (C10), 22267–22275.

Kowalik, Z., Murty, T.S., 1993. Numerical modeling of ocean dynamics. Advanced Series on Ocean Engineering, vol. 5. World Scientific, Singapore.

Leith, C., 1968. Diffusion approximation for two-dimensional turbulence. Phys. Fluids 10, 1409–1416.

Leith, C., 1996. Stochastic models of chaotic systems. Physica D 98, 481–491.

Lott, F., Miller, M., 1997. A new subgrid-scale orographic drag parametrization: its formulation and testing. Quart. J. Roy. Meterorol. Soc. 123, 101–127.

Martinsen, E., Engedahl, H., 1987. Implementation and testing of a lateral boundary scheme as an open boundary condition in a barotropic ocean model. Coast. Eng. 11, 603–627.

Mauritzen, C., Price, J., Sanford, T., Torres, D., 2005. Circulation and mixing in the Faroese Channels. Deep-Sea Res. I 52, 883–913.

McCalpin, J.D., 1994. A comparison of second-order and fourth-order pressure gradient algorithms in a σ-coordinate ocean model. Int. J. Numer. Meth. Fluids 18, 361–383.

Mellor, G.L., 1996. Users guide for a three-dimensional, primitive equation, numerical ocean model. Tech. Rep., Princeton University.

Mellor, G.L., Yamada, T., 1982. Development of a turbulence closure model for geophysical fluid problems. Rev. Geophys. Space Phys. 20, 851–875.

Mellor, G.L., Ezer, T., Oey, L.-Y., 1994. The pressure gradient conundrum of sigma coordinate ocean models. J. Atmos. Ocean. Technol. 11, 1126–1134.

Özgökmen, T.M., Fischer, P.F., 2008. On the role of bottom roughness in overflows. Ocean Modell. 20, 336–361.

Perkins, H., Hopkins, T.S., Malmberg, S.-A., Poulain, P.-M., Warn-Varnas, A., 1998. Oceanographic conditions east of Iceland. J. Geophys. Res. 103 (C10), 21531–21542.

Prater, M.D., Rossby, T., 2005. Observations of the Faroe Bank Channel overflow using bottom-following RAFOS floats. Deep-Sea Res. II 52, 481–494.

Pratt, L.J., 2008. Critical conditions and composite Froude numbers for layered flow with transverse variations in velocity. J. Fluid Mech. 605, 281–291.

Pratt, L.J., Riemenschneider, U., Helfrich, K.R., 2007. A transverse hydraulic jump in a model of the Faroe Bank Channel outflow. Ocean Modell. 19, 1–9.

Pratt, L.J., Helfrich, K.R., Leen, D., 2008. On the stability of ocean overflows. J. Fluid Mech. 602, 241–266.

Riemenschneider, U., Legg, S., 2007. Regional simulations of the Faroe Bank Channel overflow in a level model. Ocean Modell. 17, 93–122.

Saunders, P.M., 1990. Cold outflow from the Faroe Bank Channel. J. Phys. Oceanogr. 1, 29–43.

Saunders, P.M., 1992. Combining hydrographic and shipborne ADCP measurements. Deep-Sea Res. 39, 1417–1427.
Sherwin, T.J., Griffiths, C.R., Inall, M.E., Turrell, W.R., 2008. Quantifying the overflow across the Wyville–Thomson Ridge into the Rockall Trough. Deep-Sea Res. I 55, 396–404.
Shih, L.H., Koseff, J.R., Ivey, G.N., Ferziger, J.H., 2005. Parameterization of turbulent fluxes and scales using homogeneous sheared stably stratified turbulence simulations. J. Fluid Mech. 525, 193–214.
Smagorinsky, J., 1963. General circulation experiments with the primitive equations, I. The basic experiment. Mon. Weather Rev. 91, 99–164.
Smith, W.H.F., Sandwell, D.T., 1997. Global seafloor topography from satellite altimetry and ship depth soundings. Science 277, 195–196.
Umlauf, L., 2009. The description of mixing in stratified layers without shear in large-scale ocean models. J. Phys. Oceanogr. 39, 3032–3039.
Umlauf, L., Burchard, H., 2003. A generic length-scale equation for geophysical turbulence models. J. Mar. Res. 61, 235–265.
Umlauf, L., Burchard, H., Bolding, K., 2006. GOTM – Source code and Test Case Documentation, Version 4.0.
Warner, J.C., Sherwood, C.R., Arango, H.G., Signell, R.P., 2005. Performance of four turbulence closure methods implemented using a generic length scale method. Ocean Modell. 8, 81–113.
Wilcox, D.C., 2006. Turbulence Modeling for CFD. DCW Industries, Inc., La Canada, CA.
Yang, H.Q., Przekwas, A.J., 1992. A comparative study of advanced shock-capturing schemes applied to Burgers equation. J. Comput. Phys. 102, 139–159.

Paper III:

Mixing in the stratified interface of the Faroe Bank Channel overflow: the role of transverse circulation and internal waves

Mixing in the stratified interface of the Faroe Bank Channel overflow: the role of transverse circulation and internal waves

Knut S. Seim[1] and Ilker Fer[2, 3]

K. S. Seim, Department of Marine Technology, Norwegian University of Science and Technology, O. Nielsens vei 10, Tyholt, 7491 Trondheim, Norway.

I. Fer, Geophysical Institute, University of Bergen, Allégaten 70, 5007 Bergen, Norway. (Ilker.Fer@gfi.uib.no)

[1]Department of Marine Technology,
Norwegian University of Science and
Technology, Trondheim, Norway

[2]Geophysical Institute, University of
Bergen, Bergen, Norway

[3]Corresponding author

Abstract. The overflow of cold water across the Faroe Bank Channel sill is a significant volume flux of dense water to the North Atlantic Ocean. Using observations of hydrography, current and microstructure from a one-week cruise and 2-month long time series from moored instruments, we address the role of transverse circulation and internal waves in mixing in the stratified typically 100 m thick plume-ambient interface. The streamwise momentum budget is dominated by a balance between the pressure gradient and bottom friction, i.e., entrainment stress is negligible. The transverse momentum budget is in geostrophic balance, and the transverse velocity variability is governed by the isotherms ("internal" streamwise pressure gradient) relative to the bottom slope ("external" streamwise pressure gradient). The ageostrophic component of the transverse velocity at the interfacial layer, due to entrainment stress, nearly balances the "external" pressure gradient. The transverse geostrophic flow in the interfacial layer is opposed by the bottom Ekman transport in the frictional boundary layer. The shear associated with the interfacial jet contributes in reducing the gradient Richardson number and hence enhances dissipation rates in the interfacial layer. Convective overturning events observed on the upslope side suggest a link between the transverse circulation and the vertical mixing on the upper part of the slope. Several independent threads of evidence support the secondary circulation as an important mixing mechanism for the overflow plume. The amount of internal wave dissipation in the ambient above the plume and also in the interfacial layer is estimated. In the ambient, dissipation rates inferred from

fine-scale shear and density profile measurements are in good agreement with direct measurements, supporting internal wave breaking as a dominant mechanism for dissipation of turbulent energy. In the interfacial layer, spectral distribution of internal wave field inferred from the mooring data is energetic. In addition to shear-induced mixing and entrainment in the interfacial layer, we find that internal wave breaking is likely to be important for the dissipation of turbulent energy and should not be ignored.

1. Introduction

The southward export of cold, dense water from the Nordic Seas to the North Atlantic across the Greenland-Scotland ridge and the associated water mass transformation are an important part of the Atlantic Meridional Overturning Circulation. About one third of this export is through the Faroe Bank Channel (FBC, Fig. 1), the deepest passage from the Nordic Seas, in form of a bottom-attached dense plume (overflow hereafter)[*Hansen and Østerhus*, 2007]. Under the influence of pressure gradient, bottom friction, and the Earth's rotation, the overflow descends the Iceland-Faroe slope and mixes with overlaying water [*Saunders*, 2001; *Mauritzen et al.*, 2005; *Fer et al.*, 2010b]. The FBC region is one of the most studied overflow regions and has been the main focus of several projects and field studies, see *Borenäs and Lundberg* [1988]; *Hansen and Østerhus* [2000]; *Saunders* [2001]; *Borenäs and Lundberg* [2004]; *Hansen and Østerhus* [2007] for detailed reviews of the FBC overflow. Since 1995, the overflow has been monitored by moorings at the sill crest [*Hansen and Østerhus*, 2007]. Here we concentrate on one prominent feature that influences the dynamics and mixing of the overflow plume: the thick stratified interfacial layer.

Using recent observations which form a subset of the data presented in this paper, *Fer et al.* [2010b] report the following salient features of the plume, including its vertical and turbulence structure: i) the overflow plume has a typical speed of 0.5 - 1 $\mathrm{m\,s^{-1}}$, reaching a maximum of 1.35 $\mathrm{m\,s^{-1}}$ as it exits the FBC and enters the Iceland-Faroe Slope; ii) in the vertical a well-mixed, 70$\pm$35 m thick, bottom layer (BL) is separated from the overlaying water by a 120$\pm$60 m thick interfacial layer (IL), and iii) the dissipation rate of turbulent

kinetic energy, ε, is enhanced in BL and IL, but is significantly less in the core of the plume. Here we hypothesize that the presence of a thick IL has significant consequences for the dynamics of the overflow, particularly for the mixing with the overlaying water. Thick and stratified interfacial layers have previously been observed in other major overflows [*Peters and Johns*, 2005; *Girton and Sanford*, 2003; *Price et al.*, 1993].

Seim et al. [2010], comparing results from a regional simulation of the FBC overflow with the observations of *Fer et al.* [2010b], have pointed at the inadequacy of state-of-the-art turbulence closures in representing the mixing in the IL; model dissipation rates were up to 2 orders of magnitude less than the observations. The authors link the underestimated mixing in the IL to unresolved processes, such as transport of turbulent kinetic energy, TKE, [*Umlauf*, 2009], mixing due to breaking internal waves [*Baumert and Peters*, 2009], and the lack of sources of mixing for Richardson numbers (Ri) above a finite threshold set in turbulence closures. In most overflows intense mixing occurs at localized regions where low gradient Richardson numbers and large bulk Froude numbers (Fr) are co-located, suggesting that the turbulent kinetic energy source for vertical mixing is the kinetic energy of the mean flow [*Baringer and Price*, 1997]. In the case of the FBC overflow this happens between 50 and 100 km downstream of the sill; turbulence, however, is energetic along the path of the plume despite low Fr and Ri in the order of unity. Data from various sources (see e.g. *Canuto et al.* [2008]) including our own measurements show evidence for significant mixing, although $\mathrm{Ri} > 0.25$. According to *Baumert and Peters* [2009], the internal wave-turbulence transition will co-exist with the shear instability and contribute to mixing for $0.25 < \mathrm{Ri} < 0.5$. Recent models are developed which do not

impose a finite critical Ri [*Canuto et al.*, 2008; *Umlauf*, 2009]. In this paper we attempt to estimate the contribution of internal-wave induced mixing in the stratified IL.

Sections of density distribution of the FBC overflow show pinching of the isopycnals at the Faroe Bank side (southwest wall) and their spread toward the northeast wall of the channel [*Borenäs and Lundberg*, 1988; *Saunders*, 1990; *Borenäs and Lundberg*, 2004]. This is proposed to be explained by a secondary cross-channel circulation, first observed in expendable current profiler drops at the FBC sill [*Johnson and Sanford*, 1992]. The large stress at the bottom causes a significant southwest, cross-stream Ekman flow in the frictional bottom boundary layer (BBL, note that this is different than and can be shallower than the well-mixed BL) opposed by a northeast flow of similar magnitude in the IL. This secondary circulation with opposite flows at the top and bottom of the overflow suggests a spiral character in the overflow leading to considerable mixing and warming [*Johnson and Sanford*, 1992]. The spiral character of a dense overflow confined in a channel has later been confirmed in laboratory experiments [*Darelius*, 2008], and the importance of the bottom friction for the downward steering of dense water has been emphasized in theoretical work on rotating bottom gravity currents [*Wåhlin*, 2002, 2004; *Darelius and Wåhlin*, 2007; *Umlauf and Arneborg*, 2009b]. Similar dynamics has been observed in the well-mixed BL of the North Atlantic deep western boundary current [*Stahr and Sanford*, 1999]. Analysing data from a channelized, shallow rotating gravity current in the western Baltic Sea, *Umlauf and Arneborg* [2009a, b] find the mechanism of "frictional control" [*Wåhlin*, 2002, 2004], to be supported by their measurements. A nearly geostrophically-balanced jet in the interface, transporting interfacial fluid to the right of the down-channel flow, is found to have important implications for the development

of the density field and the entrainment process. Further investigation of this shallow gravity current with a series of idealized numerical experiments show that the secondary circulation laterally advects the entrained ambient water and ultimately mixes in the bottom layer on the opposite side of the channel [*Umlauf et al.*, 2010]. This shallow gravity current is characterized by Ekman numbers in the order of unity and subcritical Froude numbers, fundamentally different from the deep FBC overflow with Ekman numbers one order of magnitude smaller. Similar dynamics, however, has been observed in the FBC overflow [*Fer et al.*, 2010b], where the secondary circulation is suggested to enhance the mixing of the plume. In this paper, we describe the secondary circulation in the FBC overflow and discuss its role in mixing.

In this study we use a data set from a survey of the FBC overflow conducted in June 2008, including hydrography, current and turbulence measurements, and two-months long time series from moored instruments to study the processes at the thick IL, with focus on the secondary circulation and role of internal waves in mixing of the plume. The measurements, sampling and processing details are described in Section 2. We present and discuss the dynamics of the secondary circulation, its cross-slope structure and its role in mixing in Section 3. Subsequently, the internal wave energy in the interfacial layer and the wave dissipation in the ambient and in the interfacial layer are discussed (Section 4). Conclusions are drawn at Section 5.

2. Measurements

2.1. Sampling

Measurements were made during the cruise of R.V. Håkon Mosby between 29 May and 8 June 2008, and as time series from moored instruments deployed in the period 14

May to 18 July 2008. The data set obtained during the cruise includes vertical properties of hydrography and velocity from 63 casts with a conductivity-temperature-depth (CTD, Sea-Bird Electronics SBE911+) package equipped with a pair of down and up-looking lowered acoustic Doppler current profilers (LADCP's, RD-Instruments 300 kHz Workhorse), and of turbulence profiles from 90 casts with a vertical microstructure profiler (VMP, Rockland Scientific Instruments). The VMP can profile down to 2000 m and is equipped with accurate pumped SBE-CTD sensors, a pair of airfoil shear probes used for measuring the dissipation rate of turbulent kinetic energy (ε), and fast response temperature and conductivity sensors. The turbulence and slow sensors sampled at 512 Hz and 64 Hz, respectively, at a nominal profiling speed of $0.6\,\mathrm{m\,s^{-1}}$. Stations are taken at six cross-sections along the path of the overflow plume starting from the sill crest (Sec. A) to about 120 km downstream of the sill (Sec. F, Fig. 1), and at two stations, about 12-h long each, with repeated VMP/CTD/LADCP co-located with the moorings. Two moorings, CM and EM, are positioned approximately in the center of Sec. C and Sec. E respectively, about 60 km and 100 km downstream of the sill, recording for 2 months duration. The instrument details of the moorings are given in Table 1. The CM mooring was equipped with two Aanderaa RCM7 currentmeters at 20 and 100 m height above bottom (HAB), one downward looking ADCP (RDI 300 kHz Workhorse) at 200 m HAB and a number of temperature (SBE39 and RBR TR-1050) and CTD (SBE37 MicroCAT) loggers at different levels. The EM mooring had a similar set-up, but with an upward looking ADCP (RDI 300 kHz Workhorse) at 50 m HAB and RCM7 currentmeters at 20 and 160 m HAB (see Table 1). The sampling rate was 1 min for SBE and RBR, 5 min for ADCPs and

10 min for RCM7s. The ADCPs averaged ensembles of 50 profiles every 6 s, and profiled at 2 m vertical depth bins.

2.2. Processing details and layer definitions

The velocity profiles from the LADCP are calculated as 4 m vertical averages using the inverse method [*Visbeck*, 2002] constrained by accurate shipboard navigation and bottom tracking by the LADCP. In order to obtain as synoptic as possible section property distributions, velocity profiles are detided using a barotropic tidal model [*Egbert et al.*, 1994] for the European Shelf at 1/30° resolution. Tidal velocity is within 3 to 34% (18% on the average) of the maximum velocity at a given station [*Fer et al.*, 2010b]. Neither the estimates of stress nor the shear vertical wavenumber spectra shown later are influenced by detiding. The profiles of ε are obtained from the shear probes of VMP as 1 m vertical averages, by integrating the vertical wavenumber spectrum of shear and assuming isotropy. The noise level in ε measurements based on shear probe data in quiet sections of the water column was 10^{-10} W kg^{-1}.

We adopt right-handed Cartesian co-ordinates with positive x, y and z directed toward upstream (hence the streamwise, downstream component is -u), to the right looking downstream, and up, respectively. The velocity profiles inferred from LADCP are rotated into streamwise (-u) and transverse (v) components with respect to the direction of the maximum velocity in the bottom 200 m. The depth of the plume interface, z_i, and the plume thickness are inferred from the σ_θ =27.65 kg m^{-3} isopycnal [*Mauritzen et al.*, 2005]. The well-mixed BL thickness is estimated as the height above bottom where the density difference from the bottommost value exceeds 0.01 kg m^{-3}. The stratified IL is defined

as the layer between the top of BL and the depth above the interface where $\partial\sigma_\theta/\partial z$ first drops below $5\times10^{-4}\,\mathrm{kg\,m^{-4}}$ [*Fer et al.*, 2010b, see Fig. 2].

2.3. Mooring motion

Due to strong and highly variable currents, the moored instruments are regularly displaced from their target depth with maximum vertical displacements of about 20 m (Fig. 3a). In Fig. 3 the co-variability of the vertical displacement with passage of cold pulses of overflow is illustrated by showing the vertical displacement together with the temperature measured at 150 m HAB at the CM mooring. The instrument is knocked down into the BL from its nominal position in the IL when strong negative displacement occurs. The periodicity of the signal suggests that the low temperature incidents (and negative displacement due to strong currents) are due to thickening of the overflow plume associated with the mesoscale variability apparent in both measurements [*Seim et al.*, 2010; *Mauritzen et al.*, 2005; *Geyer et al.*, 2006] and numerical simulations [*Seim et al.*, 2010; *Riemenschneider and Legg*, 2007; *Ezer*, 2006]. The influence of mooring motion on vertical displacement calculations are discussed in Sec. 4.2. The mesoscale variability apparent in the present data set is the topic for an ongoing study and will not be addressed here.

3. Secondary circulation

3.1. Dynamics

Johnson and Sanford [1992] attributed the pinching of the isotherms in the FBC overflow to a transverse, secondary circulation in the overflow. The large bottom stress exerted on the overflow gives rise to a cross-flow transport of about 1/16 of the overflow transport

in the bottom layer and a transport of similar magnitude in the opposite direction in the interfacial layer associated with strong shear and mixing [*Johnson and Sanford*, 1992]. Later studies of dense water flow in channels link the cross-channel flow in the interfacial layer to the along-channel tilt of isopycnals [*Wåhlin*, 2004; *Umlauf and Arneborg*, 2009b] resulting in a transverse geostrophic flow. Such an idealized geostrophically-balanced dense water flow and its structure are illustrated in Fig. 4. In these simplified models the flow is stationary and the interfacial slope coincide with the bottom slope (in cross-channel direction in *Wåhlin* [2004] and in along-channel direction in *Umlauf and Arneborg* [2009b]). Downstream of the FBC sill crest, the dense plume flows along the Iceland-Faroe slope and is no longer a channel flow; we use streamwise and transverse directions in analogy with down-channel and cross-channel directions. Following *Umlauf and Arneborg* [2009b] we assume stationary flow, negligible horizontal mixing and negligible advection except for advection of the streamwise momentum to obtain the shallow-water equations:

$$\frac{\partial u^2}{\partial x} + \frac{\partial uw}{\partial z} - fv = \int_z^\infty \frac{\partial b}{\partial x}\, d\hat{z} - \frac{1}{\rho_0}\frac{\partial \tau_x}{\partial z}\,, \tag{1a}$$

$$fu = \int_z^\infty \frac{\partial b}{\partial y}\, d\hat{z} - \frac{1}{\rho_0}\frac{\partial \tau_y}{\partial z}\,, \tag{1b}$$

where f is the Coriolis parameter, τ_x and τ_y denote the horizontal components of the vertical flux of momentum, and b is the buoyancy with respect to the background density, ρ_0:

$$b = -g\frac{\rho - \rho_0}{\rho_0}\,.$$

Here ρ and g denote the density and the acceleration of gravity. Different from *Umlauf and Arneborg* [2009b] who assumed identical streamwise slope of bottom and interface, we

retain variable streamwise interface slope, i.e., *Umlauf and Arneborg* [2009b] approximate the pressure gradient in Eq. (1a) by $-bS_x$, where S_x is the along-channel bottom slope.

The mean profiles of streamwise and transverse velocity components, temperature, T, and buoyancy frequency, N, inferred from mooring data are shown in Fig. 5. Also shown are the profiles of T and N averaged over 7 CTD casts within 8 km of the mooring position, collected during the June 2008 cruise. The comparison suggests that, although limited by the short duration of the cruise, survey-mean profiles (see Fig. 10) will be representative of time-mean properties averaged over the mesoscale variability not resolved by the cruise data. The velocity profiles from CM (Fig. 5a) clearly show the signature of the secondary circulation: a weak flow of about 100 m thick, stratified IL to the right of streamwise velocity opposed by a return current at 20 m HAB, consistent with the Ekman flow in the frictional boundary layer. The results presented here, however, also show that the assumptions of stationarity and identical bottom/interfacial slopes will fail in the case of the FBC overflow. In Fig. 6, the time evolution of the streamwise slope of the interfacial layer, estimated from the mean slope of the 3 and 6 °C isotherms between moorings CM and EM, is shown together with the transverse velocity averaged in the layer between the two isotherms. The slope of IL, and correspondingly the transverse geostrophic velocity, is highly variable in time, and the magnitude of this variability is comparable to the streamwise bottom slope. In this region, the temperature-salinity relation is tight, and isotherms are representative of isopycnals (density inferred from a third degree polynomial fitted to temperature is accurate to within an r.m.s. error of $0.01\,\mathrm{kg\,m^{-3}}$). Within this layer, using density from T, we compute the geostrophic transverse velocity by integrating

the thermal wind shear:

$$v_g = \frac{1}{f}\int_{z_{iso3}}^{z} \frac{\partial \overline{b}}{\partial x}\, d\hat{z}\,, \tag{2}$$

where v_g is referenced to the measured transverse velocity at $z = z_{iso3}$ and $\overline{b}$ is the 48-hour low-pass filtered buoyancy. The resulting geostrophic velocity has two contributions: due to the tilt of the isotherms parallel to the streamwise bottom slope (the assumption made by *Wåhlin* [2004] and *Umlauf and Arneborg* [2009b]) with little variation in time, and a highly variable component due to the "internal" pressure gradient (tilt of the isotherms deviating from the bottom slope) (Fig. 7). The measured transverse velocity oscillates with the tilt of the isotherms with peak values exceeding $30\,\mathrm{cm\,s^{-1}}$ to the right (and $20\,\mathrm{cm\,s^{-1}}$ to the left) of the streamwise flow. The mean transverse velocity is $3.8\,\mathrm{cm\,s^{-1}}$ directed to the right of the streamwise velocity. The geostrophic velocity in the layer, v_g, is significantly larger than the observed transverse velocity. On the average $v_g = 16.3\,\mathrm{cm\,s^{-1}}$, with a contribution from the bottom slope ("external" pressure gradient) of $2\,\mathrm{cm\,s^{-1}}$. This difference between the measured transverse velocity and v_g indicates that the velocity is reduced by the entrainment stress in the interfacial layer resulting in a transverse Ekman transport due to the streamwise flow. This ageostrophic transport in the interface opposes v_g. The reduction in the transverse velocity due to interfacial stress approximately balances the transverse flow due to the tilt of the isotherms parallel to the streamwise bottom slope. The transverse velocity variability is thus governed by the tilt of the isotherms deviating from the bottom slope (i.e. "internal" pressure gradient).

3.2. Cross-slope structure

Stahr and Sanford [1999] present a 2-D conceptual model of flow within the BBL and BL to explain their observations of the deep western boundary current at the Blake Outer Ridge. They observed a cross-slope asymmetry in the structure of the boundary layers and the along-slope velocity, the latter causing a cross-slope divergence of the bottom Ekman layer transport advecting light water down-slope. This process, possibly also together with convection, leads to a thickening of the BL. The mean upwelling from the convergence drives a weak up-slope return flow of the Ekman transport, which keeps density uniform throughout the BL. The cross-slope dynamical structure presented by *Stahr and Sanford* [1999] seems to offer a plausible explanation of the cross-stream structure of the secondary circulation of the FBC overflow (Fig. 8). In Fig. 8b LADCP/CTD observations along Sec. C show that the downslope (to the left of the streamwise flow) transverse velocity in the BL is opposed by a transverse flow in the IL. The maximum BL transverse velocity along the section is also associated with the maximum in the streamwise velocity. A successive convergence in the transverse velocity is expected together with a thickening of the well-mixed layer (BL, congruent to the bottom mixed layer in *Stahr and Sanford* [1999]). Here the location of thickening of the BL coincides with the velocity maximum but is not downslope of the maximum as anticipated from the conceptual model. We attribute this discrepancy to the mesoscale variability of the overflow; occupation of the section, about 10 hours, will be influenced by this variability. The core of the dense overflow plume, associated with the largest buoyancy anomaly (Fig. 8d), is located in the vicinity of the velocity maximum. The largest negative buoyancy anomaly is farther downslope. As the secondary circulation transports this dense water upslope along isopycnals in the

IL, it stratifies the interface and suppresses the vertical movement and thus thickening of the plume. Farther upslope, convective mixing, induced by relatively light interface water brought under the plume by bottom Ekman transport, will tend to thicken the plume. While this is not observed at the upslope stations at Sec. C (Fig. 8a), the mooring data reveal the presence of convective overturning and well-mixed layers on the slope (Section 3.4).

3.3. Bottom versus entrainment stress

By integrating Eq. (1a) and assuming that the buoyancy varies linearly inside the interface of thickness d_i, *Umlauf and Arneborg* [2009b] express the interfacial transverse transport, q_i, in nondimensional form as

$$\frac{q_i}{U d_i} \approx -E_k \left(\frac{1}{2} - \frac{r_E}{r_d} \right) , \tag{3}$$

where U is the vertically-integrated streamwise plume velocity, E_k is the Ekman number and r_E and r_d are the ratios of the entrainment stress to the total down-channel stress and of interface thickness to total overflow thickness, respectively. The former ratio is given by $r_E = E/(C_d + E)$, where E is the entrainment parameter and C_d is the drag coefficient for a quadratic bottom friction law. According to Eq. (3) q_i has a geostrophically balanced contribution and an oppositely directed contribution due to entrainment. The transverse transport obeys a purely geostrophic balance if $r_E/r_d \ll 1$. For thick interfaces $r_d = O(1)$ the requirement is that the entrainment has to be weak compared to bottom friction ($r_E \ll 1$). Applying the drag coefficient, $C_d = 3.7 \times 10^{-3}$, and the entrainment velocity, $w_E = 5.8 \times 10^{-5}\,\mathrm{m\,s^{-1}}$, reported by *Fer et al.* [2010b], a conservative estimate for the ratio of entrainment stress to total stress is $r_E = 0.03$, assuming $r_d \sim 1$. Thus, according to the

CTD/LADCP measurements, the Ekman transport due to entrainment has a negligible effect on the total transport and the transverse interfacial transport is in geostrophic balance. In our observations, the geostrophically balanced component explains 80% of the variability in the measured transverse velocity. The streamwise momentum budget is dominated by a balance between the pressure gradient and bottom friction, whereas the transverse momentum budget is in geostrophic balance.

To investigate the influence of the time variability on the streamwise stress, we estimate the streamwise, vertically-integrated pressure gradient according to

$$P_x = \int_{z_b}^{z_{iso6}} \frac{\partial p}{\partial x}\, dz = \int_{z_b}^{z_{iso6}} \left(\rho_0 \int_{z}^{z_{iso6}} \frac{\partial b}{\partial x}\, d\hat{z} \right) dz\,. \tag{4}$$

The pressure gradient varies with the inherent 3-4 day mesoscale oscillations (Fig. 9). On the average P_x=2.8 Pa and the pressure gradient is nearly balanced by the survey-averaged bottom stress $\tau_b = 2.1 \pm 0.4$ Pa [*Fer et al.*, 2010b]. In the mean, steady state, i.e., the imbalance is not used for accelerating the flow, the entrainment stress is thus of negligible importance.

3.4. Role in mixing

In the vicinity of each of the two moorings, CM and EM, two VMP time series stations were occupied during the 2008 survey. The secondary circulation structure is clearly visible in the average velocity profiles (Fig. 10b). Time series are too short to capture the mesoscale variation, but the contrast in profiles illustrates the strong influence of the streamwise flow on the transverse circulation. While the EM station experiences high streamwise velocity (Fig. 10b) as the overflow thins (Fig. 10a) subsequent of a maximum in plume thickness, the CM station shows lower velocities as the plume thickens. The evo-

lution in plume thickness and the flow strength are also confirmed with the mooring time series (not shown). The high streamwise velocity is associated with enhanced transverse circulation, particularly in the interface layer.

The average gradient Richardson number, Ri= N^2/S^2 where $N^2 = -g/\rho(\mathrm{d}\rho/\mathrm{d}z)$ is the buoyancy frequency-squared, and $S^2 = u_z^2 + v_z^2$ is the shear-squared. The average 4-m Ri calculated at 4-m vertical separation from CTD/ADCP profiled (Ri_{4m}, Fig. 10c) and the dissipation rate (Fig. 10d) from the VMP measurements show that dissipation level is enhanced at EM where Ri_{4m} is less than unity and frequently less than 0.25, the threshold when shear instabilities occur in stratified flows. Shear is enhanced in the stratified IL at both stations. At EM, the sheared-transverse jet in the IL further reduces Ri_{4m}, favoring shear-induced mixing and large dissipation rates in the IL. Average Ri_{4m} between 70-160 m HAB at EM (the range in IL where the shear is strong both in u and v) is 0.4. When calculated using the shear from the streamwise component of the velocity alone ($S^2 = u_z^2$), average Ri_{4m} increases to 0.7, by about 75%. Secondary circulation enhances the shear and contributes to reducing Ri.

In addition to enhancing shear-induced mixing, the secondary circulation favors convective mixing in the upslope edge of the plume. Approximately 10 km upslope from CM, at 686 m water depth, an additional mooring sampled temperature at 1 min intervals at 8 levels between 25-110 m HAB. Using the temperature difference between the uppermost and bottommost sensors (ΔT) we identify periods of well-mixed layers ($|\Delta T| < 0.01$ K) and convective conditions ($\Delta T <$ -0.01 K). Well-mixed and convective conditions on the slope correspond to periods when the transverse velocity in IL is directed onslope (positive), suggesting a link between transverse circulation and vertical mixing on the upper

part of the slope. In total 39 periods were detected with a total duration of 7.3 day (out of a total record of 63.8 day, i.e. 9%) when the deepest 110 m on the slope was well-mixed in temperature. While 8 of these periods were of duration longer than 10 h (14 $\pm$ 4 h), the remaining lasted for 2 $\pm$ 1.8 h. For the mixed conditions, depth average temperature was less than 1.5 °C at all times and was colder than zero for 54% of the total duration. During the well-mixed periods 42 convective events were detected, with 6 lasting longer than 4 h (6.3 $\pm$ 2.9 h), however, typical duration of the convective events were about 2 h. The mean separation between the convective periods was approximately 3.5 day, correlating with the mesoscale variability.

4. Internal waves

4.1. Wave energy in the interfacial layer

Internal waves can exist in the thick, stratified IL and can contribute to the mixing of the FBC overflow. In Fig. 11, the spectral distribution of the mean total baroclinic velocity of the layer between the 3 and 6° C isotherms is shown at CM, inferred from the ADCP. This instrument, installed in a spherical buoy, experienced tilt (from vertical) less than 5° at all times, returning high-quality data. The baroclinic velocities are approximated by removing the vertically-averaged velocity (including velocity measurements at all levels). The mean spectra of total velocity (i.e. spectrum of twice the HKE density) are then formed by averaging the spectra from all ADCP bins within the 3-6° C layer. This range is well-resolved by the ADCP but is only about half the total extent of IL (see Fig. 2). Spectra are computed for the north and east component of velocity using 2048 point (7.1 day) half-overlapping Hanning segments giving 18 degrees of freedom. The total spectrum is then formed by adding the two components, $\Phi_V = \Phi_u + \Phi_v$. The average spectrum

in the layer (18 ADCP levels) has 324 degrees of freedom for the calculation of the 95% confidence interval. The average spectrum at EM is also calculated, however, the ADCP installed in an in-line frame experienced significant tilt ($> 15^\circ$ for 60% of the record). The average spectrum at EM (not shown) calculated using the portion of the time series with good data (times when both pitch and roll $< 15^\circ$) is similar, both in magnitude and in shape, to that of CM. For reference, the Garrett-Munk (GM) [*Garrett and Munk*, 1972] internal wave spectrum is also shown in Fig. 11, calculated using the local f and N. For all frequencies above the semi-diurnal frequency the velocity variance distribution at both moorings is more energetic than the GM internal wave spectrum and decreases with frequency at a fairly constant rate in agreement with the GM slope. As the buoyancy frequency is approached, both spectra flatten to white noise.

Based on the current measurements from both RDI-ADCP and RCM7, the kinetic energy associated with the two selected frequency bands, the "inertial/semi-diurnal tide" band and the "internal wave" band (marked in Fig. 11), is calculated by integrating the total velocity spectra over the corresponding band. A vertical profile of the baroclinic kinetic energy for the CM mooring is presented in Fig. 12. The upper part of the interfacial layer (150-190 m, see Figs. 2 and 5a) clearly stands out as highly energetic in the internal wave frequency band, both with respect to the corresponding GM energy and relative to that in the near-inertial band.

4.2. Influence of mooring motion

The total velocity spectra and the inferred energy levels are expected to be influenced by the mooring motion in response to mesoscale oscillations. Using spectra from three independent data sets at CM, we estimate the spectral signature and energy level associ-

ated with the mooring motion. The measurements used are the pressure and temperature recorded by the microcat at 150 m HAB and the vertical velocity from the 2-m thick ADCP bin centered at 150 m HAB. In Fig. 13a the vertical displacement spectra, Φ_ζ, are shown for the displacement, ζ, calculated from the pressure measurement and from the temperature measurement using the mean vertical temperature gradient (from the mean T-profile shown in Fig. 5). At the level where the spectra are calculated, the mean temperature gradient is $\mathrm{d}T/\mathrm{d}z = 4.4\times\ 10^{-2}\,^\circ\mathrm{C\,m^{-1}}$ and the buoyancy frequency is $N =$ 3.2 cycles per hour (cph, 1 cph $= (2\pi/3600)\,\mathrm{s^{-1}}$). The variance of the T-derived vertical displacement is significantly larger compared to the actual mooring displacement (from pressure) for all frequencies. We conclude that despite occasional significant motion of the mooring the isotherm displacement spectra are not corrupted.

Another independent comparison is the spectrum of the vertical velocity measured by the RDI-ADCP and that inferred from the vertical displacement recorded by the microcat pressure sensor (Fig. 13b). Supporting the conclusion from the isotherm vertical displacement spectrum, the variance of the vertical velocity is significantly larger compared to the vertical velocity spectrum associated with mooring motion, estimated from pressure. Following *Levine et al.* [1997], error in displacement variance due to mooring motion can be quantified as $e = \langle d'^2\rangle + [T_{err}/\langle \mathrm{d}T/\mathrm{d}z\rangle]^2$ where T_{err} is a typical temperature measurement error (here set to 0.01 °C). A signal-to-noise ratio, SNR, defined as the displacement variance inferred from T divided by e, using 12-hour high-passed data, calculated over 3-h segments, show that 6% of the data has SNR < 5, and on average SNR is about 250.

4.3. Wave energy dissipation in the ambient

We hypothesize that a dominant mechanism for dissipating turbulent energy in the stratified ambient, above the overflow plume, is internal wave breaking. In a slowly varying internal wave field, the rate of energy dissipation due to wave breaking approximately equals the net energy transfer toward smaller scales [e.g., *Gregg*, 1989]. Using vertical profiles of velocity and density resolved at fine scales (order of meters), the viscous dissipation rate of TKE (ε) can be inferred. In essence this is done by comparing and scaling the observed levels of shear and strain, the vertical derivative of isopycnal displacements ζ_z, to the GM levels. The most recent form of the finescale parameterization can be expressed as [*Gregg et al.*, 2003]:

$$\varepsilon_{IW} = \varepsilon_0 \left(\frac{N}{N_0}\right)^2 \left(\frac{0.1}{k_c}\right)^2 \left(\frac{1+1/R_\omega}{4/3}\right) \left(\frac{2}{R_\omega - 1}\right)^{1/2} L(f,N)\,, \tag{5}$$

where $\varepsilon_0 = 6.7 \times 10^{-10}\,\mathrm{W\,kg^{-1}}$ is the background dissipation level for GM conditions, and L contains the latitude dependence:

$$L(f,N) = \frac{f\,\mathrm{arccosh}(N/f)}{f_{30}\,\mathrm{arccosh}(N_0/f_{30})}\,.$$

N is the local buoyancy frequency, f is the local inertial frequency, $N_0 = 5.2 \times 10^{-3}\,\mathrm{s^{-1}}$ ($\equiv 3\,\mathrm{cph}$) is the reference stratification and f_{30} is the inertial frequency at 30° latitude. In Eq. (5), the term with R_ω corrects for the variation in the ratio of N-normalized shear variance to strain variance (shear-strain ratio)

$$R_\omega = \frac{\langle V_z^2 \rangle}{N^2 \langle \zeta_z^2 \rangle}.$$

Here and in the following the variance of x is denoted by $\langle x^2 \rangle$. For the GM model $R_\omega = 3$, $N = N_0$, $f = f_{30}$ and $k_c = 0.1$ cpm, and all correction and scaling terms cancel out leading to $\varepsilon = \varepsilon_0$, i.e., very weak dissipation. The significant figure in ε_0 is not representative of the accuracy of this parameterization, which is approximately a factor of two. The cutoff vertical wavenumber, k_c, is the wavenumber up to which the integrated shear variance is approximately $0.7N^2$. Consequently, the ratio of average observed and GM spectral levels at wavenumbers less than k_c is $0.1/k_c$. The higher this elevation above GM the higher the dissipation.

At the repeat stations co-located with EM and CM, in addition to the microstructure profiles, we collected 2 and 4, respectively, CTD/LADCP casts. The two casts at EM were taken only 6 h apart and did not resolve the semidiurnal cycle, whereas the station duration at CM was about 15 h. Above the plume and below the upper 100 m (in the ambient and below the surface layer), we calculate the vertical wavenumber (k_z) shear spectra from LADCP and strain spectra from CTD profiles between 100 and 610 m depth (i.e. 128 data points for 4-m sampled LADCP and 512 data points for 1-m sampled CTD). We obtain spectra of shear $\Phi_{shear} = (2\pi k_z)^2 \Phi_V$, and strain $\Phi_{strain} = (2\pi k_z)^2 \Phi_\zeta$, from the spectra of total velocity (Φ_V) and vertical displacement (Φ_ζ) calculated as averages over half-overlapping 64 and 256 point (256 m) long segments. This gives 12 and 24 degrees of freedom, respectively, for EM and CM. Vertical displacement profiles are calculated relative to the station mean density profile. The shear spectra are normalized by the average N^2 in the corresponding segment. Resulting spectra are shown in Fig. 14 together with the GM spectra. The GM spectra are white (constant with k_z) and decay with -1 slope after $k_c = 0.1$ cpm. This roll-off moves to lower wavenumbers as the energy increases

[*Polzin et al.*, 1995], shown for the observed shear level by the dashed lines in Fig. 14. The average shear spectra from both stations are consistent with the roll-off until the instrumental noise begins to contaminate the spectra at about $1/k_z = 50\,\mathrm{m}$. All spectra suggest whitening at low wavenumbers. While the shape of shear and strain spectra are consistent at EM, the strain spectrum at CM is white out to higher wavenumber compared to the shear spectrum.

In application of Eq. (5) we infer k_c as the first wave number where the integrated N-normalized shear spectrum reaches 0.7. For both stations, this is reached at $k_z = 0.0078\,\mathrm{cpm}$, corresponding to a wavelength of 128 m. Variance of shear and strain are then calculated by integrating the corresponding spectrum to k_c, to obtain R_ω. At EM, shear and strain are comparable ($R_\omega = 1.7$), whereas at CM shear is significantly more energetic ($R_\omega = 6.9$). Note, however, EM sampling is of 6 hour duration and is biased. Because the variances are obtained by integrating to 128 m wavelength, the noise contamination is negligible. Finescale parameterization leads to dissipation rates of $2.8\times10^{-8}\,\mathrm{W\,kg^{-1}}$ and $5.4\times10^{-9}\,\mathrm{W\,kg^{-1}}$ for EM and CM, respectively. Dissipation rate measured by the microstructure profiler, averaged in the same depth range, is $4.4\times10^{-9}\,\mathrm{W\,kg^{-1}}$ and $2.4\times10^{-9}\,\mathrm{W\,kg^{-1}}$, with 95% confidence limits of the maximum likelihood estimator from a lognormal distribution $[4.\ 4.8]\times10^{-9}\,\mathrm{W\,kg^{-1}}$ $[2.3\ 2.6]\times10^{-9}\,\mathrm{W\,kg^{-1}}$. The agreement between the observed dissipation and that inferred from Eq. (5) is within 50% at CM. At EM, on the other hand, ε_{IW} is about 6 times the observed value. This can partly be attributed to the lack of sampling throughout the semidiurnal cycle. Furthermore N-normalized shear variance can be dominated by noise in weak stratification

[*Kunze et al.*, 2006; *Fer et al.*, 2010a]. At EM the mean stratification is weak with $N = 0.0012\,\mathrm{s}^{-1}$ (0.69 cph), close to noise level. At CM, $N \sim$1.2 cph.

The finescale parameterization assumes that energy is transferred from large to small scales through nonlinear wave-wave interactions. In the ambient above the plume this assumption might hold, but will fail near the sloping bottom boundary layer where other processes dominate the scale transformation [*Polzin*, 2004], close to internal wave generation sites, and for internal hydraulic phenomena such as internal hydraulic jumps and direct breaking of internal tides.

4.4. Wave energy dissipation in the interfacial layer

Keeping in mind that the energy transfer through the wave spectrum spectral domain in IL can be dominated by different processes due to non-GM shear (e.g. entrainment and mixing at the plume-ambient interface, influence of secondary circulation, mesoscale subinertial shear etc.), we naively apply the wave dissipation model of *Henyey et al.* [1986] to the CM mooring data. This is encouraged by the GM-like shape of the total velocity frequency spectrum (Fig. 11) in IL (or more accurately, between 3-6 °C isotherms). The motivation here is not to evaluate or test the parameterization, but to get an estimate of the amount of dissipation rate that can be attributed to internal wave-induced mixing. We follow *Wijesekera et al.* [1993] in applying the model, and the reader is referred to their paper for a detailed review of the wave dissipation models. In terms of dimensional energy, $E = b^2 N N_0 E_{GM}$, the dissipation rate induced by the GM wave field is

$$\varepsilon_{HWF} = \left[\frac{1.67}{\pi}\right] b^{-2} N_0^{-2} f \,\mathrm{arccosh}\left[\frac{N}{f}\right] j_\star^2 \, E^2, \tag{6}$$

where $E_{GM} = 6.3 \times 10^{-5}$ is the non-dimensional GM energy level, $b = 1300\,\mathrm{m}$ is the thermocline depth scale, and $j_\star = 3$ is the vertical wavenumber bandwidth parameter. An estimate of dissipation due to observed energy level in IL is made by replacing E in Eq. (6) with E_{meas}, where the measured energy level is

$$E_{meas} = \frac{1}{2}\left[\langle\zeta^2\rangle N^2 + \langle u^2\rangle + \langle v^2\rangle + \langle w^2\rangle\right]. \tag{7}$$

The total baroclinic energy in Eq.(7) is the sum of the potential energy, PE, the horizontal kinetic energy, HKE, and that due to the vertical velocity. Each term is obtained by integrating the layer-averaged frequency spectra between f and N. The baroclinic horizontal velocity is approximated by removing the depth-average over the measurement range. The barotropic contribution to ζ is estimated from a linear fit (with zero intercept) of displacement against depth obtained from T-measurements at 200, 150, 100 and 20 m HAB. The integrated variance of horizontal velocity is about 14 times that of w, HKE = 3.1×10^{-3} m^2 s^{-2}, and the ratio of HKE to PE is about 2.2. Resulting estimate of dissipation rate due to internal waves in IL is $\varepsilon_{HWF} = 1.5 \times 10^{-9}\,\mathrm{W\,kg^{-1}}$. Averaged between 3-6 °C isotherms, the measured dissipation rate at CM (see Fig. 10d) is $\varepsilon = 1.4 \pm 0.6 \times 10^{-8}\,\mathrm{W\,kg^{-1}}$ ($\pm$ one standard deviation). The wave model accounts for about 10% of the observed dissipation rate. Note, however, that Eq. (6) is sensitive to $j_\star$, which can vary from site to site, and is not matched to our obsevations. At Yermak Plateau region north of Svalbard, *Wijesekera et al.* [1993] infer $j_\star$ between 3 and 12. In the southern part of the Plateau *Fer et al.* [2010a] infer $j_\star$ between 6 and 17. Increasing $j_\star$ from 3 to 9 will completely account for observed dissipation rate. Given the uncertainties involved in the application of this model, both in theory and in the parameters involved, we cannot draw

a firm conclusion on the amount of dissipation rate in IL due to internal waves, however we conclude that internal-wave induced mixing in IL can be significant and should not be ignored.

5. Concluding remarks

Observations of hydrography, currents and turbulence from the FBC overflow, conducted in 2008, have been analysed with emphasis on mixing in the stratified interface, addressing the role of transverse circulation and internal waves. The observations comprise profiles of velocity, hydrography, microstructure temperature and shear, and 2-month long time series of current, temperature and salinity from moored instruments. Strong temporal and spatial variability characterise the FBC overflow, and the assumption of stationarity is considered to be crude. Mesoscale oscillations have a prominent signature in the overflow strength and structure, in general, and affect the transverse circulation, in particular. The cross-stream flow near the bottom (Ekman transport) and in the interfacial layer (geostrophic transport) effectively contributes to mixing in several ways: by diluting the bottom layer of the plume, by acting as an advective source of buoyancy, by transporting IL water to the right of the streamwise flow, by reducing the Richardson number in IL, and by convection on the upper slope. Dissipation rates are more than doubled in the interfacial layer due to the transverse flow. The transverse velocity in the interfacial layer deviates slightly from a purely geostrophic flow, but a streamwise pressure gradient nearly balanced by the bottom stress, suggests that the overflow is under "frictional control" (nearly geostrophic transverse flow in the interfacial layer opposed by the Ekman transport in the bottom layer).

Above the overflow plume, in the ambient waters, the main mechanism of dissipating turbulent energy is breaking of internal waves, and can be inferred from the fine-scale parameterization of *Gregg et al.* [2003]. In the interfacial layer main mechanism of mixing is the shear-instability and entrainment associated with the swift gravity current, enhanced by the secondary circulation. However, we find that the internal wave continuum is energetic in the interfacial layer and may significantly contribute to mixing.

Acknowledgements

This work is funded through the Academia agreement between the Norwegian University of Science and Technology and Statoil ASA, and by the Research Council of Norway, through the Bipolar Atlantic Thermohaline Circulation (BIAC) project. KSS received partial support from the University of Bergen. We thank Elin Darelius for performing the mooring motion corrections and preparing the mooring data for analysis.

References

Baringer, M. O., and J. F. Price, Mixing and spreading of the Mediterranean Outflow, *J. Phys. Oceanogr.*, *27*, 1654–1677, 1997.

Baumert, H. Z., and H. Peters, Turbulence closure: turbulence, waves and the wave-turbulence transition - Part 1: Vanishing mean shear, *Ocean Sci.*, *5*, 47–58, 2009.

Borenäs, K. M., and P. A. Lundberg, On the deep-water flow trough the Faroe-Bank Channel, *J. Geophys. Res.*, *93*, 1281–1292, 1988.

Borenäs, K. M., and P. A. Lundberg, The Faroe-Bank Channel deep-water overflow, *Deep-Sea Res. II*, *51*, 335–350, 2004.

Canuto, V. M., Y. Cheng, A. M. Howard, and I. N. Esau, Stably stratified flows: a model with no Ri(cr), *J. Atmos. Sci.*, *65*, 2437–2447, 2008.

Darelius, E., Topographic steering of dense overflows: Laboratory experiments with V-shaped ridges and canyons, *Deep-Sea Res. I*, *55*, 1021–1034, 2008.

Darelius, E., and A. K. Wåhlin, Downward flow of dense water leaning on a submarine ridge, *Deep-Sea Res. I*, *54*, 1173–1188, 2007.

Egbert, G. D., A. F. Bennett, and M. G. G. Foreman, TOPEX /POSEIDON tides estimated using a global inverse model, *J. Geophys. Res..*, *99*, 24,821–24,852, 1994.

Ezer, T., Topographic influence on overflow dynamics: idealized numerical simulations and the Faroe Bank Channel, *J. Geophys. Res.*, *111*, doi:10.1029/2005JC003195, 2006.

Fer, I., R. Skogseth, and F. Geyer, Internal waves and mixing in the Marginal Ice Zone near the Yermak Plateau, *J. Phys. Oceanogr.*, *40*, 1613–1630, 2010a.

Fer, I., G. Voet, K. S. Seim, B. Rudels, and K. Latarius, Intense mixing of the Faroe Bank Channel overflow, *Geophys. Res. Lett.*, *37*, L02,604, doi:10.1029/2009GL041924, 2010b.

Garrett, C. J., and W. H. Munk, Space-time scales of internal waves, *Geophys. Fluid Dyn.*, *3*(1), 225–264, 1972.

Geyer, F., S. Østerhus, B. Hansen, and D. Quadfasel, Observations of highly regular oscillations in the overflow plume downstream of the Faroe Bank Channel, *J. Geophys. Res.*, *111*, C12,020, doi:10.1029/2006JC003693, 2006.

Girton, J. B., and T. B. Sanford, Descent and modification of the overflow plume in the Denmark Strait, *J. Phys. Oceanogr.*, *33*, 1351–1364, 2003.

Gregg, M. C., Scaling turbulent dissipation in the thermocline, *J. Geophys. Res.*, *94*(C7), 9686–9698, 1989.

Gregg, M. C., T. B. Sanford, and D. P. Winkel, Reduced mixing from the breaking of internal waves in equatorial waters, *Nature*, *422*(6931), 513–515, 2003.

Hansen, B., and S. Østerhus, North Atlantic-Nordic Seas exchanges, *Prog. Oceanogr.*, *45*, 953–954, 2000.

Hansen, B., and S. Østerhus, Faroe Bank Channel overflow 1995-2005, *Prog. Oceanogr.*, *75*, 817–856, 2007.

Henyey, F. S., J. Wright, and S. M. Flatte, Energy and action flow through an internal wave field: An eikonal approach, *J. Geophys. Res.*, *91*, 8487–8495, 1986.

Johnson, G., and T. Sanford, Secondary circulation in the Faroe Bank Channel outflow, *J. Phys. Oceanogr.*, *22*, 927–933, 1992.

Kunze, E., E. Firing, J. M. Hummon, T. K. Chereskin, and A. M. Thurnherr, Global abyssal mixing inferred from lowered ADCP shear and CTD strain profiles, *J. Phys. Oceanogr.*, *36*(8), 1553–1576, 2006.

Levine, M. D., L. Padman, R. D. Muench, and J. H. Morison, Internal waves and tides in the western weddell sea: Observations from ice station weddell, *J. Geophys. Res.*, *102*(C1), 1073–1089, 1997.

Mauritzen, C., J. Price, T. Sanford, and D. Torres, Circulation and mixing in the Faroese Channels, *Deep-Sea Res. I*, *52*, 883–913, 2005.

Peters, H., and W. E. Johns, Mixing and entrainment in the Red Sea outflow plume. Part II: Turbulence characteristics, *J. Phys. Oceanogr.*, *35*, 584–600, 2005.

Polzin, K., A heuristic description of internal wave dynamics, *J. Phys. Oceanogr.*, *34*(1), 214–230, 2004.

Polzin, K. L., J. M. Toole, and R. W. Schmitt, Finescale parameterizations of turbulent dissipation, *J. Phys. Oceanogr.*, *25*(3), 306–328, 1995.

Price, J. F., M. O. Barringer, R. G. Lueck, and G. C. Johnson, Mediterranean outflow and mixing dynamics, *Science*, *259*, 1277–1282, 1993.

Riemenschneider, U., and S. Legg, Regional simulations of the Faroe Bank Channel overflow in a level model, *Ocean Model.*, *17*, 93–122, 2007.

Saunders, P. M., Cold outflow from the Faroe Bank Channel, *J. Phys. Oceanogr.*, *1*, 29–43, 1990.

Saunders, P. M., The dense northern overflows, in *Ocean Circulation and Climate*, edited by G. S. et al., pp. 401–417, Academic, Sand Diego, Calif., 2001.

Seim, K. S., I. Fer, and J. Berntsen, Regional simulations of the Faroe Bank Channel overflow using a σ-coordinate ocean model, *Ocean Model.*, *35*, 31–44, doi: 10.1016/j.ocemod.2010.06.002, 2010.

Stahr, F. R., and T. B. Sanford, Transport and bottom boundary layer observations of the North Atlantic Deep Western Boundary Current at the Blake Outer Ridge, *Deep-Sea Res. II*, *46*, 205–243, 1999.

Umlauf, L., The description of mixing in stratified layers without shear in large-scale ocean models, *J. Phys. Oceanogr.*, *39*, 3032–3039, 2009.

Umlauf, L., and L. Arneborg, Dynamics of rotating shallow gravity currents passing through a channel. Part I: Observation of transverse structure, *J. Phys. Oceanogr.*, *39*, 2385–2401, 2009a.

Umlauf, L., and L. Arneborg, Dynamics of rotating shallow gravity currents passing through a channel. Part II: Analysis, *J. Phys. Oceanogr.*, *39*, 2402–2416, 2009b.

Umlauf, L., L. Arneborg, R. Hofmeister, and H. Burchard, Entrainment in shallow rotating gravity currents: a modeling study, *J. Phys. Oceanogr.*, *40*, 1819–1834, 2010.

Visbeck, M., Deep velocity profiling using lowered acoustic Doppler current profilers: Bottom track and inverse solutions, *J. Atmos. Oceanic Technol.*, *19*, 794–807, 2002.

Wåhlin, A. K., Topographic steering of dense currents with application to submarine canyons, *Deep-Sea Res. I*, *49*, 305–320, 2002.

Wåhlin, A. K., Downward channeling of dense water in topographic corrugations, *Deep-Sea Res. I*, *51*, 577–590, 2004.

Wijesekera, H., L. Padman, T. Dillon, M. Levine, C. Paulson, and R. Pinkel, The application of internal-wave dissipation models to a region of strong mixing, *J. Phys. Oceanogr.*, *23*(2), 269–286, 1993.

Table 1. Details for the moorings CM and EM. The instrument sensor positions are given as height above bottom (HAB).

	CM	EM
Lon/Lat	9 °11′W / 61 °41′N	9 °50′W / 61 °45′N
Depth	804 m	990 m
in/out	14.05 / 18.07.2008	14.05 / 17.07.2008
P	210, 150 m	100, 70, 50 m
T	210, 201 m 200-140, 10 m interval 148, 101, 20 m	160, 100 m 98, 70 m 60, 50, 20 m
C	201, 150, 101, 20 m	100, 70, 60 m
u/v	210-110, 2 m interval (ADCP) 100, 20 m (RCM7)	150-50, 2 m interval (ADCP) 160, 20 m (RCM7)

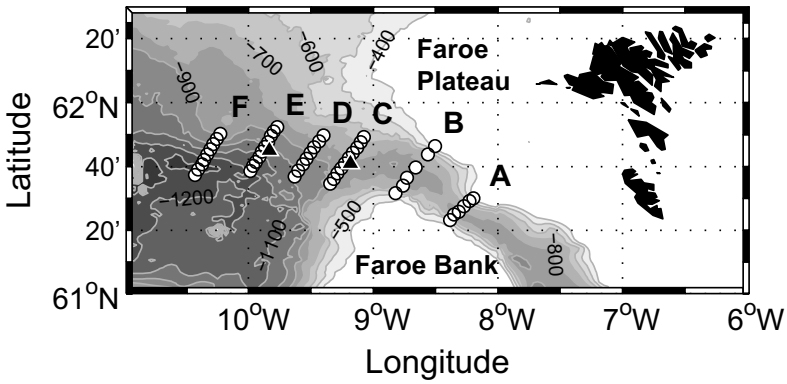

Figure 1. Map of all stations (circles) occupied during the June 2008 survey. The position of the two moorings used in this study (CM and EM) are marked with triangles.

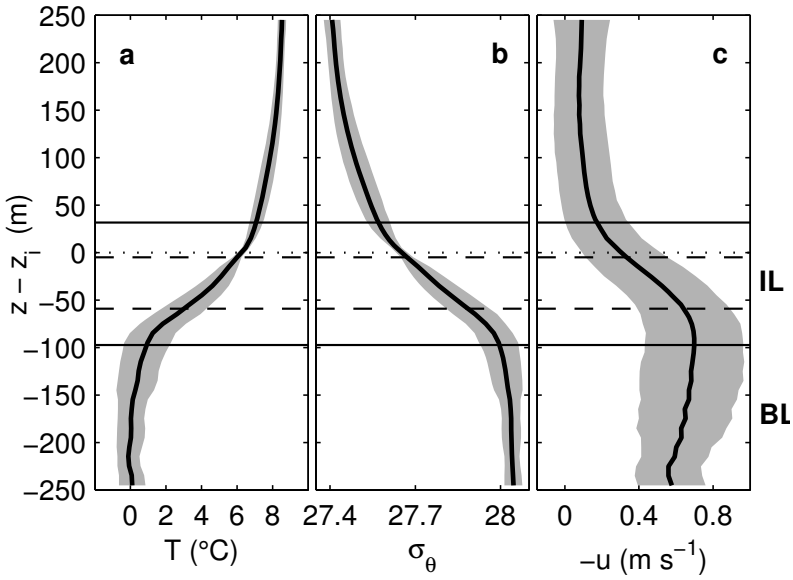

Figure 2. Survey-averaged profiles of (a) temperature, T, (b) potential density anomaly, σ_θ, and (c) streamwise velocity, $-u$, for all stations sampling the overflow. The solid lines mark the top of the interfacial layer (IL) and top of the well-mixed bottom layer (BL), the dashed lines are the 3 °C and 6 °C isotherms, and the dotted line is the plume interface z_i. Vertical axis is depth relative to z_i. Individual profiles are averaged in bins of $z - z_i = 10$ m. Grey envelopes are ± 1 standard deviation.

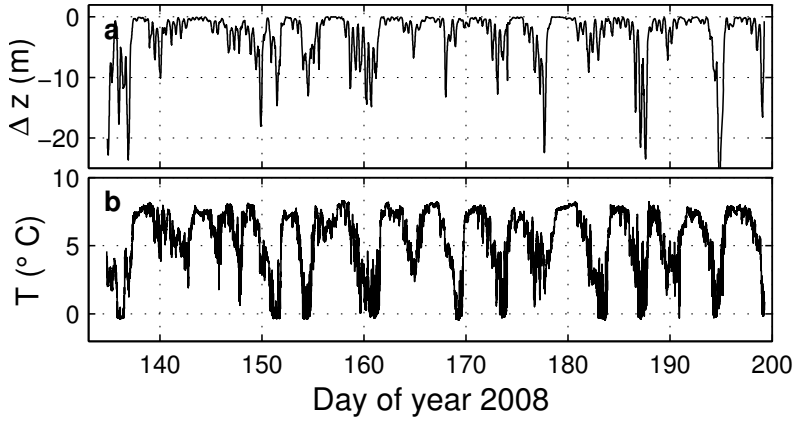

Figure 3. Variability of (a) vertical displacement of the microcat at 150 m HAB at mooring CM calculated from the measured pressure and (b) temperature recorded by the same instrument.

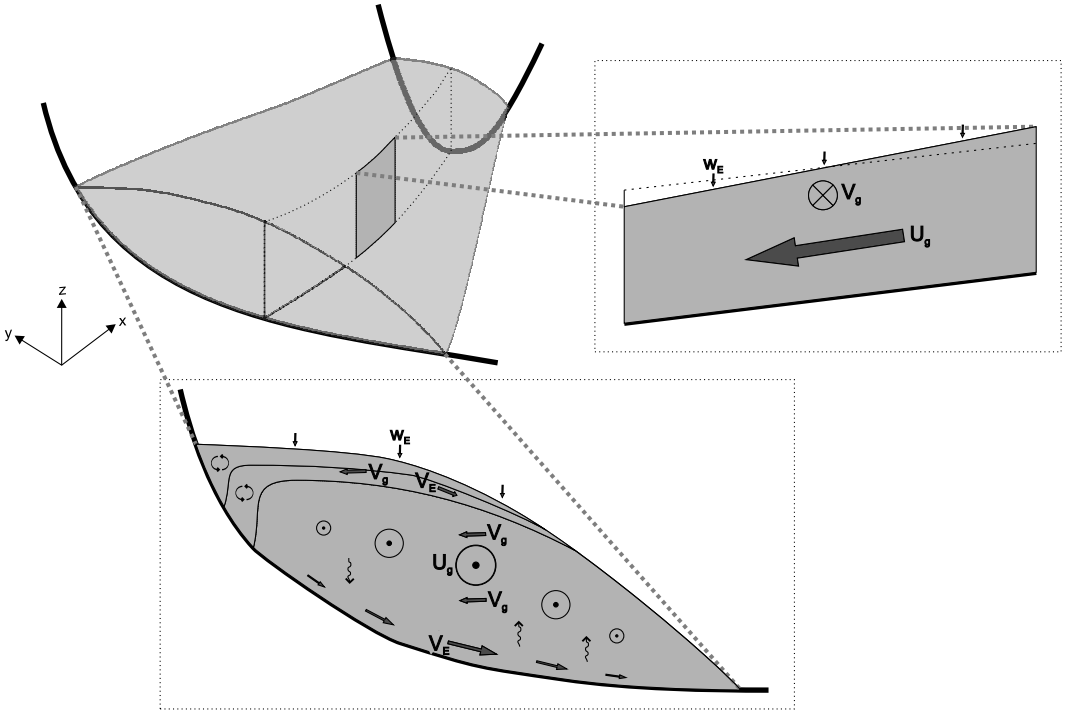

Figure 4. Illustration of the FBC overflow plume structure and the secondary circulation.

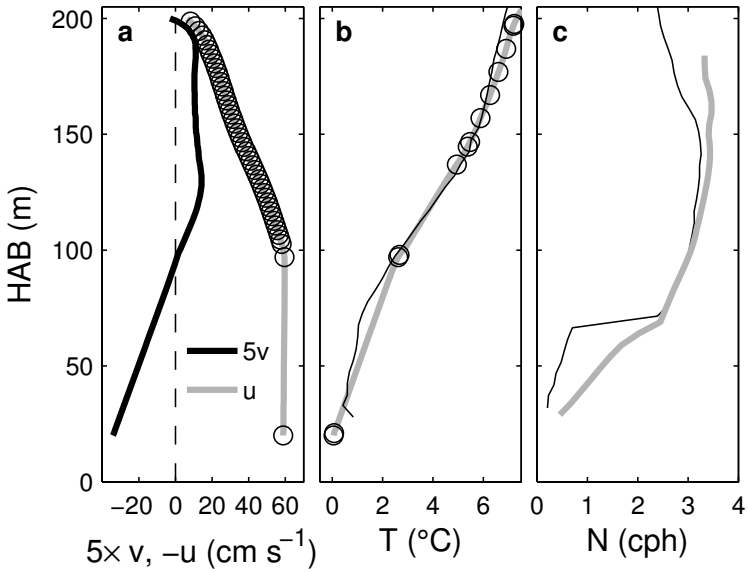

Figure 5. Mean profiles of (a) streamwise velocity, $-u$, and transverse velocity, v, multiplied by 5 for clarity, (b) temperature, and (c) buoyancy frequency, N inferred from CM mooring data. In panels b and c the profiles averaged using 7 nearby CTD casts are also shown (black). Circles mark the nominal levels (time mean positions) where measurements are available.

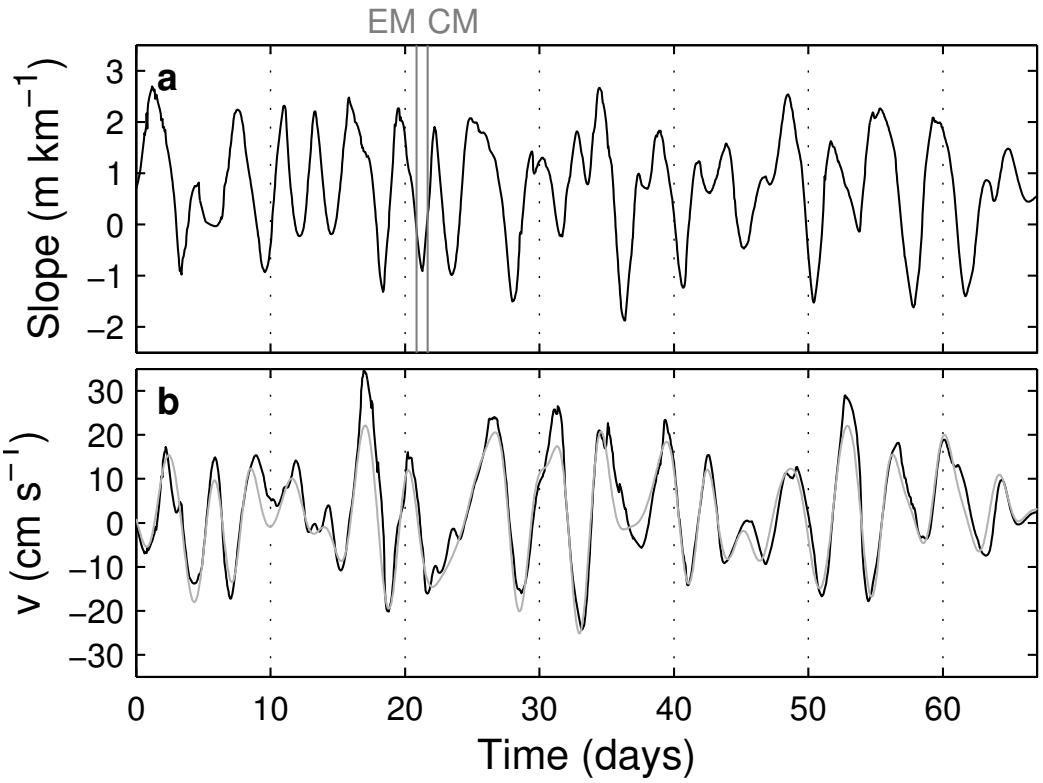

Figure 6. Time evolution of (a) the mean streamwise slope of the 3 and 6 °C isotherms between moorings CM and EM, (b) mean transverse velocity (over both moorings) averaged between 3 and 6 °C isotherms (black) and from the 3 °C isotherm to the upper extent of the ADCP range (grey). Vertical lines in a) mark the start time of time series stations at EM and CM.

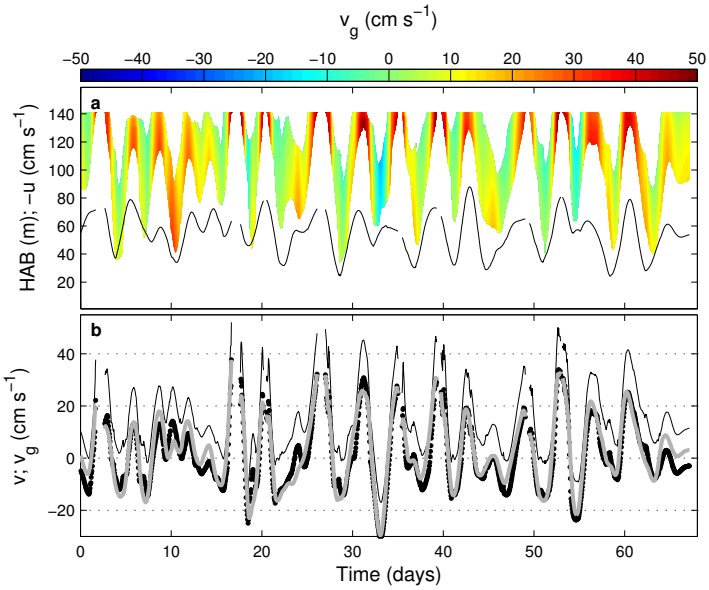

Figure 7. Time evolution of (a) vertical distribution of the geostrophically-balanced transverse velocity v_g (color) together with the streamwise velocity $-u$ (black) averaged over the layer between 3 and 6 °C isotherms, and (b) vertical mean of v_g calculated from the slope of isotherms between moorings CM and EM (black), the measured average transverse velocity, v (grey) and v_g with the contribution from the bottom slope removed (dotted).

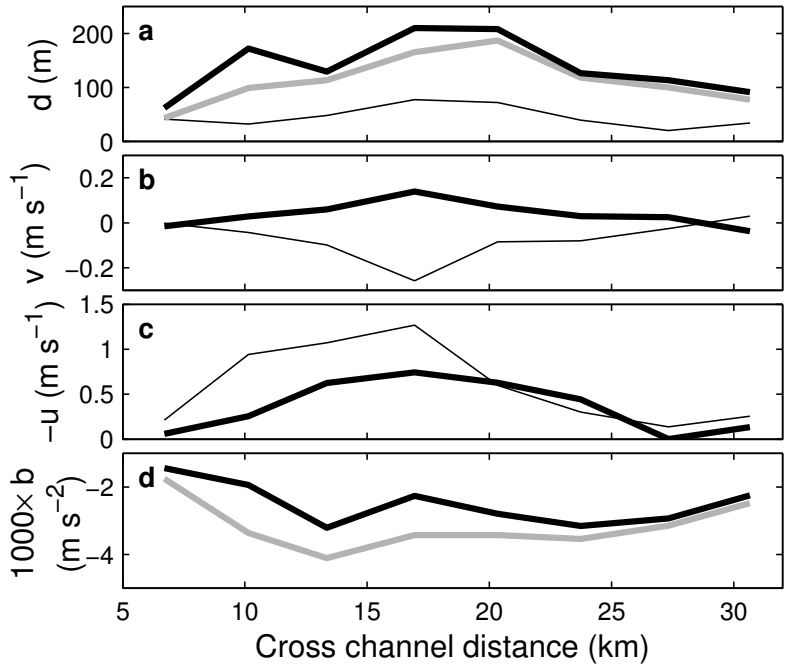

Figure 8. Distribution of (a) top of BL (thin), plume interface (grey), and top of IL (thick black), (b) average transverse velocity, v, and (c) average streamwise velocity, $-u$, in BL (thin) and IL (thick), and (d) buoyancy, b, averaged over the plume thickness (defined by the plume interface, grey) and over IL (black) along Section C. Distance is relative to the deepest station on the Faroe-Island Slope; no plume water was detected in the first two stations. Faroe Bank is on the left and Faroe Plateau is on the right.

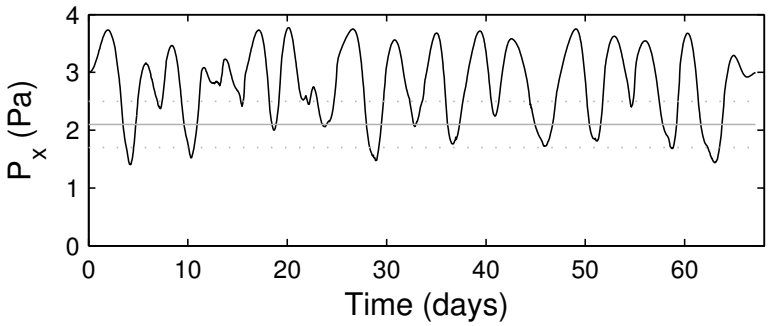

Figure 9. Vertically-integrated streamwise pressure gradient, P_x, calculated according to Eq. (4), between moorings CM and EM. Horizontal grey lines show the survey-averaged bottom stress τ_b (solid) with uncertainty (dashed) inferred from the May 2008 cruise.

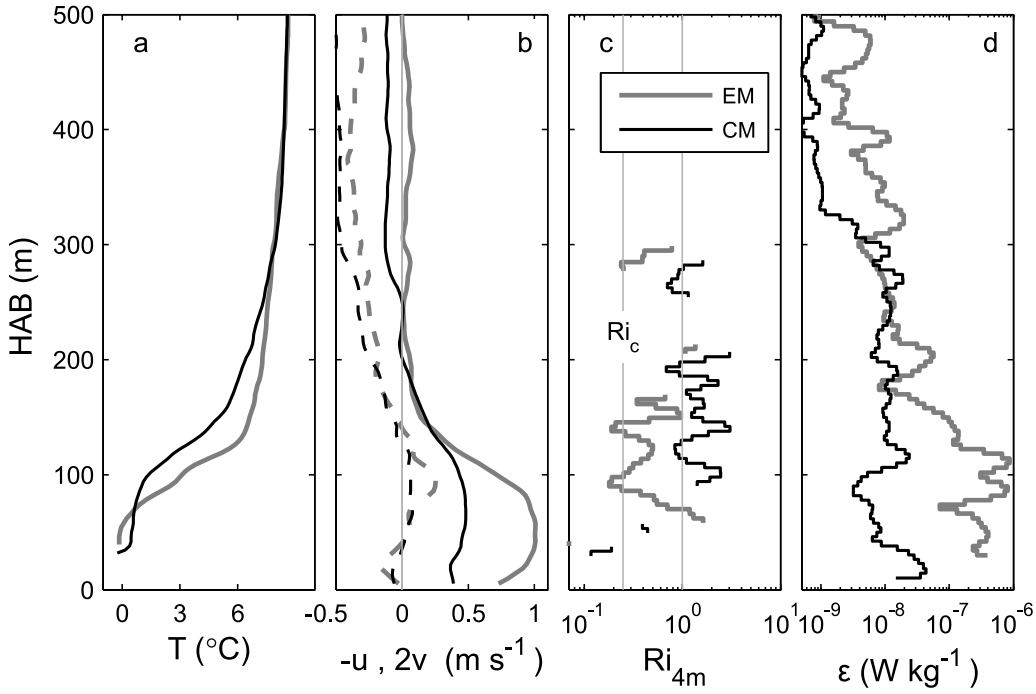

Figure 10. Average profiles of (a) temperature, (b) streamwise ($-u$) and transverse (v, dashed, multiplied by two for clarity) components of the velocity, (c) 4-m gradient Richardson number, and (d) the dissipation rate, ε, collected at the EM (black) and CM (grey) time series stations. All casts are averaged with respect to height above bottom (HAB) in 4-m vertical bins. Ri calculations are only shown when measured buoyancy frequency and velocity are greater than imposed error thresholds of 0.5 cph and 1 cm s^{-1}, respectively. Vertical lines in (c) mark the critical $\mathrm{Ri}_c = 0.25$, and $\mathrm{Ri} = 1$.

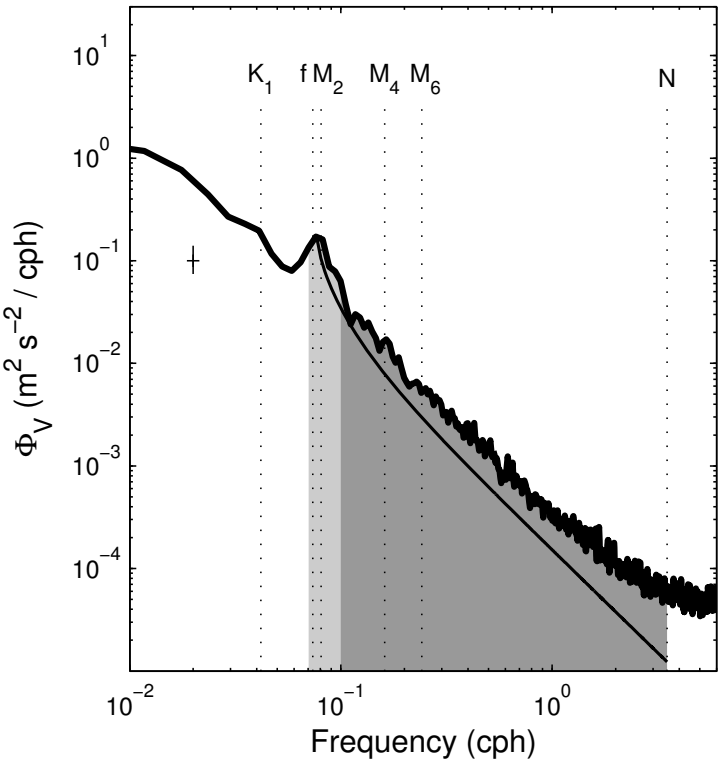

Figure 11. Horizontal baroclinic velocity spectra ($\Phi_V = \Phi_u + \Phi_v$), averaged over the layer between the 3 °C and 6 °C isotherms, calculated from the ADCP data at CM. Baroclinic velocity is estimated by removing the depth-mean velocity (from full mooring coverage) at each time. The GM velocity spectrum with a -2 slope is included for reference. The pale and dark grey shaded areas depict the frequency bands used for estimating the kinetic energy. Error bar shows the 95% condidence interval.

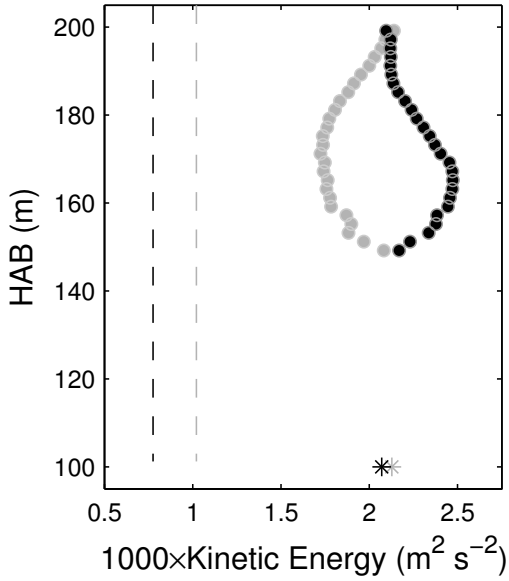

Figure 12. Kinetic energy calculated by integrating the horizontal energy spectra from the CM mooring over the near-inertial (semi-diurnal) band (grey) and the higher frequency internal wave band (black) (see Fig. 11a). Dots are from ADCP data while the stars are data from the RCM at 100 m HAB. The dashed and dotted lines are the corresponding kinetic energy for GM spectrum using local f and N.

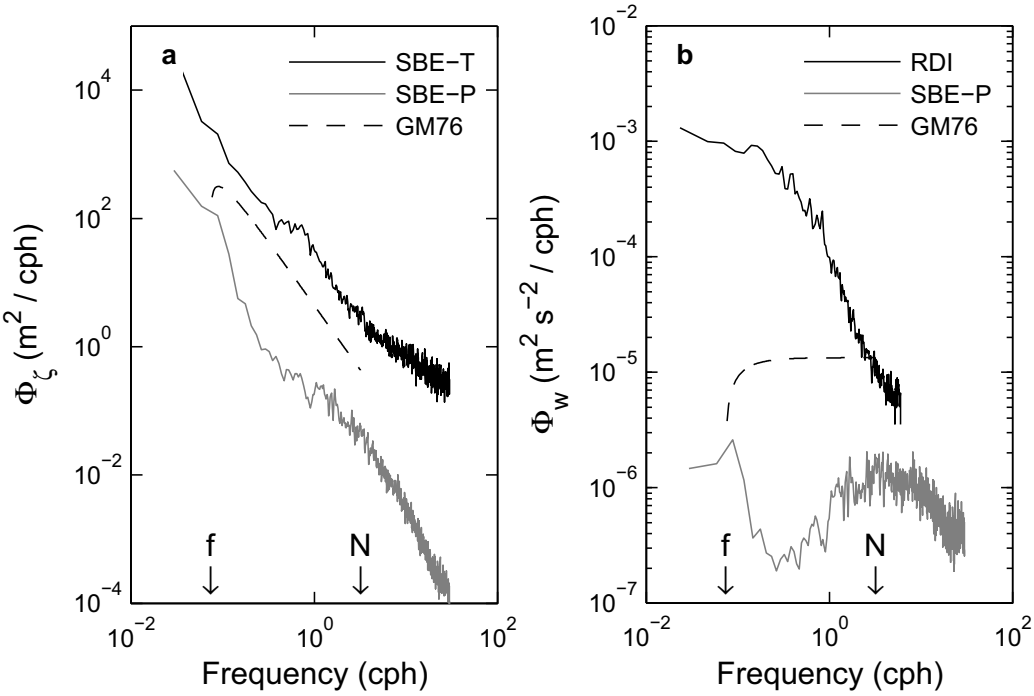

Figure 13. CM mooring (a) vertical displacement spectra calculated from temperature (black) using the mean vertical temperature gradient, and from pressure measurement (grey), (b) vertical velocity spectrum measured by RDI-ADCP (black) and inferred from pressure (grey). All measurements are approximately the same level (about 150 m HAB). The dashed lines are the GM displacement and vertical velocity spectra using local f and N.

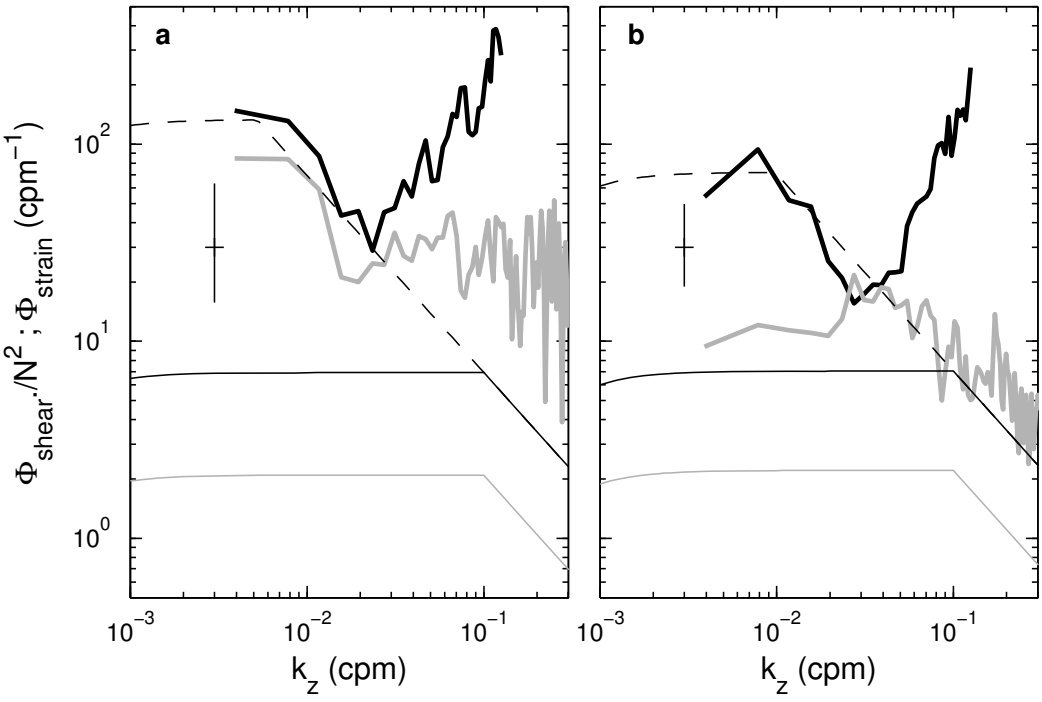

Figure 14. Spectra of shear (black) and strain (grey) obtained from the spectra of total velocity and vertical displacement respectively, using LADCP/CTD data collected during the June 2008 cruise near a) EM and b) CM. The canonical GM spectra are shown for reference, together with the GM spectra adjusted to the observed shear level and roll-off extended to k_c. The vertical lines are the 95% confidence intervals, valid for both shear and strain spectra, using 12 (EM) and 24 (CM) degrees of freedom.

Paper IV:

Stratified flow over complex topography

Stratified flow over complex topography

Knut S. Seim

Department of Marine Technology, Norwegian University of Science and Technology, Otto Nielsens vei 10, NO-7491 Trondheim, Norway

Abstract

The flow of stratified fluid over complex topography may lead to a significant drag on the fluid, exerted by the bottom obstacles. Using a 2-m resolution, three-dimensional, non-hydrostatic numerical ocean model, the drag and associated mixing on a stratified flow over real, 1-m resolution topography (interpolated to model resolution) is studied. With a typical mountain height of 12 m in 174 m water and buoyancy frequencies ranging from $0.6\times10^{-2}\,\mathrm{s}^{-1}$ to $1.2\times10^{-2}\,\mathrm{s}^{-1}$, resolving the topographic features leads to extensive drag exerted on the flow manifested through three different processes: i) gravity wave drag, ii) aerodynamic or blocked flow drag, and iii) hydraulic drag. A parameterization of the internal wave drag based on linear, two-dimensional, hydrostatic wave solutions provides satisfactory results in terms of the turbulent kinetic energy levels. The depth of the layer where the vertical momentum flux is deposited, however, is underestimated, leading to an overestimated gravity wave drag in the layer.

Email address: knut.seim@ntnu.no (Knut S. Seim)

1. Introduction

Understanding the boundary layer processes in the ocean is essential for an accurate representation of the vertical buoyancy flux in ocean general circulation models (OGCMs). In order to close the overturning circulation, the dense water masses sinking to abyssal depths across all major ocean basins have to be balanced by a buoyancy gain and an upward vertical motion. In the interior of the ocean, diapycnal mixing is the only mechanism that can increase the buoyancy of a water parcel (Thurnherr, 2006). Observations indicate a strong association between diapycnal mixing in the abyss and rough topography (Polzin et al., 1997; Ledwell et al., 2000), and that the abyssal circulations have complex spatial structures that are linked to the underlying bathymetry. Dense overflows, another important piece in the global overturning circulation, are bottom-attached flows, influenced by complex topography. Understanding and parameterizing their mixing is of crucial importance.

It has been recognized that overflows are not necessarily homogeneous, but may have a vertical density structure, typically consisting of a dense bottom layer and a so-called interfacial layer (Peters and Johns, 2005; Fer et al., 2010; Seim et al., 2010), in which internal waves can contribute to mixing (Seim and Fer, 2010). Internal wave breaking is suggested to be the dominating mechanism for dissipation of turbulent energy in the ambient above the Faroe Bank Channel overflow plume and should not be ignored in the interfacial layer (Seim and Fer, 2010). This mechanism is typically neither resolved nor parameterized in numerical model studies of such overflows. The models only account for bottom roughness through simple drag laws. Parameteri-

zations of mountain wave drag based on linear internal wave solutions have significantly improved the atmospheric general circulation models (Kim and Arakawa, 1995). In most ocean models, on the other hand, due to the lack of high resolution topographic data and limited knowledge of the interaction between topographic features and the bottom boundary layer, the effect of subgrid-scale topographic features is not parameterized.

The aim of this study is, by applying a high resolution (comparable to the typical length scale of turbulent overturns), non-hydrostatic numerical ocean model, to describe the flow of a stratified fluid past resolved complex topography, and to parameterize the wave drag exerted by unresolved topography on the flow. The background theory is given in Section 2 for homogeneous and stratified flow over topography. The numerical model and the model set-up are described in Section 3, followed by the results presented and discussed in Section 5. Conclusions are drawn at Section 6.

2. Background

2.1. Homogeneous fluid flow

The first step in studying flow over topography is to consider the flow of a homogeneous layer past isolated topography (Baines, 1995, Chap. 2). Such single layer flows are characterized by the Froude number of the undisturbed flow defined by $F_0 = U/\sqrt{gd_0}$, where U is the velocity, g is the gravitational acceleration, and d_0 is the undisturbed flow depth. In sub-critical flows ($F_0 < 1$), linear waves may propagate both upstream and downstream, whereas in super-critical flows ($F_0 > 1$) the upstream propagation is not possible. For the one-dimensional flow there is only an associated drag force on the

obstacle in the resonant case when $F_0 = 1$ (critical flow), and the upstream propagating wave remains stationary relative to the obstacle. In the two-dimensional case, there is no drag force on the obstacle for $F_0 < 1$, but a discontinuously increasing drag as F_0 increases above unity (Baines, 1995). In this hydraulic flow theory it is assumed that the flow is hydrostatic, which is a good approximation for obstacles with a long horizontal scale compared to the fluid depth such that $d_0/L \ll 1$, where L is the obstacle width, or $kd_0 \ll 1$, where k is the wave-number. For the values of $kd_0 \gg 1$, the flow generates dispersive, non-hydrostatic waves that propagate energy away from the obstacle. In general, this condition is not atypical in the ocean, particularly when considering regional scale flows such as the flow of dense overflow water over rough topography or through channel systems.

2.2. Stratified flow

Hydraulic theory is no longer applicable when the flow is stratified (due to propagating internal waves). Assuming a stable, undisturbed flow, any small disturbance may extract energy from the kinetic energy of the mean flow, generating a spectrum of internal wave modes when topography is introduced. If the width of the obstacle is sufficiently small, overturning lee waves leading to increased mixing are expected. In a flow limited with depth d_0, two significant dimensionless quantities are the mode number,

$$K = \frac{Nd_0}{\pi U}\,, \tag{1}$$

and the dimensionless obstacle height,

$$h_n = \frac{Nh}{U}\,, \tag{2}$$

where

$$N = \sqrt{-\frac{g}{\rho_0}\frac{\partial \rho}{\partial z}}\,, \tag{3}$$

is the buoyancy frequency, h is the height of the obstacle, ρ is the density and ρ_0 is a constant reference density. The dimensional obstacle height is the ratio of the vertical scale of the obstacle to the approximate vertical length scale of the waves, U/N, and is thus a measure of the non-linearity of the disturbed flow. As h_n increases, the flow is more likely to generate overturning internal waves. The critical limit of the dimensional obstacle height, h_{nc}, depends on the shape of the obstacle. Studying obstacles of general semi-elliptical shape over the whole range of aspect ratios $\gamma = h_m/a$, where h_m is the maximum obstacle height and a is the half-width of the obstacle, Huppert and Miles (1969) found h_{nc} to range from 0.67 ($\gamma = 0$; flat semi-ellipse) to 1.73 ($\gamma = \infty$; vertical barrier). Long (1955) derived a non-linear stream-function equation for a uniform infinite-depth flow over a bump and predicted $h_{nc} = 1.27$ for a semi-circle ($\gamma = 1$). In a more recent numerical study, Lamb (1994) found that h_{nc} (for $1 < K < 2$) was considerably smaller than that predicted by Long's model. For depth-limited flow the additional length-scale d_0 is introduced through K, which is the inverse Froude number with respect to the fastest internal wave mode with phase speed $c_1 = Nd_0/\pi$ relative to the fluid. When $K < 1$ (supercritical flow) linear theory gives a reasonably accurate description of the flow, in good agreement with observations (Baines, 1979). In this case the obstacle exerts no significant drag on the flow. For flows with $K > 1$ (subcritical flow), observations and numerical studies have concentrated in the range where only the first lee wave mode is present, i.e. $1 < K < 2$. The linear theory describes

the lee wave field reasonably well as long as $h_n \ll 1$, and K is not close to an integer (if $K = j$ for a positive integer j, the mean flow is critical with respect to the jth mode in the long wave length limit, see Baines (1995)). For steady flows with $K \neq j$, the pressure distribution over the obstacle is symmetric and the drag vanishes, while for $K = j$ the upstream propagating part and the steady part of the jth internal wave are in resonance, and the drag is non-zero as in the homogeneous layer case. Performing three-dimensional large-eddy simulations of a stratified oceanic flow over a "witch of Agnesi" profile with mode numbers (K) ranging from 0.89 to 2.24, Skyllingstad and Wijesekera (2004) obtained qualitatively similar results to the analytical and laboratory results of Long (1955) and Baines (1979). The strong dependence on both the mode number and the relative obstacle height was strong when free-slip condition on the lower boundary are applied. Introducing a bottom frictional drag decreased the role of lee waves and the accompanying wave drag in some cases, especially for large velocities (small K). Their results were also in agreement with Lamb (1994) in showing that obstacle height thresholds for wave breaking based on Long's equation were too high. They conclude that bottom features can have a major effect on the momentum budget of the coastal ocean without requiring significant turbulence fluxes, and that pressure drag can effectively reduce the average velocity through internal wave propagation with wave dissipation possibly occurring some distance from the source region.

2.3. Stratified flow over complex terrain

Proceeding to the more general case of three-dimensional topography, the distinction between finite and infinite depth is less significant as the

disturbances caused by a topographic feature spread out laterally as well as vertically so that the presence of an upper boundary has a minor effect locally (unless it is at a low level) (Baines, 1995). If the obstacles in a complex region all have comparable heights with $Nh/U < 1$, the disturbance field of each obstacle is approximately linear and the interaction is minimal. In this case the drag is transmitted in the form of internal gravity waves. The reference-level drag, τ_0, and the drag above the reference level, τ, may be expressed as (Palmer et al., 1986; Kim and Arakawa, 1995)

$$\tau_0 = \kappa \rho_0 N_0 U_0 h^2 \,, \tag{4}$$

$$\tau = \kappa \rho N U \delta h^2 \,, \tag{5}$$

where κ is a tunable constant dependent on the statistical properties of the topography, h is a height proportional to the standard deviation of the topography, δh is displacement wave amplitude, and ρ_0, N_0 and U_0 are the low-level density, buoyancy frequency, and the velocity component in the direction of the reference drag, all typically evaluated between the blocking height $z_b \approx h - U/N$ and the typical obstacle height h. If, on the other hand, $Nh/U > 1$ so that flow splitting and lee wave overturning occur, the interaction may be significant, and the drag by the obstacle is spread amongst three different processes; gravity wave drag (Eq. 4 and 5), hydraulic drag, associated with hydraulic flow over the topography, and aerodynamic or blocked flow drag. Linear theory may, however, still be applied if the obstacles are relatively isolated and spread out, by the linear superposition of the net effects of each obstacle and its wake (Baines, 1995).

3. The numerical model and set-up

The numerical model used in this study is the Bergen Ocean Model (BOM, Berntsen, 2000). BOM is a σ-coordinate (terrain-following) ocean model with non-hydrostatic capability. The governing equations are the same as those for the Princeton Ocean Model (POM, Blumberg and Mellor, 1987; Mellor, 1996), but the numerical methods are different. For advection of momentum and density a TVD-scheme with a superbee limiter described in Yang and Przekwas (1992) is applied. The model is mode split with a method similar to the splitting described in Berntsen et al. (1981) and Kowalik and Murty (1993). The solution is propagated in time using single time step methods. For the depth-integrated momentum and continuity equation a predictor-corrector method is applied.

3.1. Model set-up

The domain (Fig. 1) covers a 400 m $\times$ 400 m subregion of the Storegga slide region, on the continental slope west of mid-Norway. This region is selected due to its rough topography and the available high resolution (1 m) topography data collected in connection with the development of the Ormen Lange gas field. The model has a horizontal resolution of 2 m. In the vertical there are 81 layers, in 174 m water depth, resulting in a resolution of approximately 2 m (1.96-2.30 m). The boundaries at $y = 0$ m and $y = 400$ m are closed, while at both the inflow ($x = 0$ m) and outflow ($x = 400$ m) boundary, a flow relaxation scheme (FRS, Martinsen and Engedahl, 1987) is used. The FRS zone extends for 30 grid cells. To assure proper flux conservation in the domain, the topography is flattened towards the boundaries with the first 5

cells set to the mean depth and a region of 25 cells where the topography is weighted by a hyperbolic tangent function.

Initially the fluid is at rest. Two forms of stratification are studied: a linear density profile or a hyperbolic tangent density profile resembling the Faroe Bank Channel overflow (Fer et al., 2010; Seim et al., 2010) with a well mixed bottom layer and an interfacial layer of comparable thickness (Fig. 2). At the inflow boundary the velocity in the x-direction, u, is ramped up towards the background velocity u_0, over approximately twice the time a parcel needs to travel over the length of the the domain, L_x, at the background velocity. The density profile of the inflow water is set to the initial density profile. The surface elevation at the inflow boundary is relaxed towards an average of the elevation in 30 grid cells (60 m) outside the FRS zone. At the outflow boundary, density is relaxed towards the average of 30 cells outside the FRS zone, while the velocity is relaxed towards the average over the domain omitting the FRS zones. The surface elevation is relaxed towards zero elevation at the outflow boundary. Given the relatively high resolution, constant, weak diffusivity and viscosity is applied. The horizontal and vertical diffusivity is set to $1.0 \times 10^{-6}\,\mathrm{m^2\,s^{-1}}$, the horizontal viscosity is $1.0 \times 10^{-4}\,\mathrm{m^2\,s^{-1}}$ and in the vertical the viscosity is $1.0 \times 10^{-5}\,\mathrm{m^2\,s^{-1}}$.

3.2. Model runs

The results presented in this study comprise of four different cases simulating flow over resolved complex terrain with varying stratification, and a fifth simulation in which the topography and drag are parameterized. In the last run, the domain represents one grid point region (GPR) with flat bottom, and the wave drag exerted on the flow is parameterized using the

statistical properties of the resolved topography and the linear wave theory. The different simulation runs are listed in Table 1, and the high resolution topography is shown in Fig. 1. Initially the density is linear (run1 and run2) or a hyperbolic tangent profile (run3-5). The density profile and the corresponding buoyancy frequency profile are shown in Fig. 2 together with the spin-up of the velocity identical for all cases. For the two linear density profile cases, the buoyancy frequency is $5.7\times10^{-3}\,\mathrm{s}^{-1}$ (run1) and $1.0\times10^{-2}\,\mathrm{s}^{-1}$ (run2).

4. Representation of topography

Considering our domain resembling one grid point in a coarse model with a depth given by the mean value of the 1 m resolution topography, $\bar{d}$, the sub-grid-scale topography of that GPR may be represented by four parameters: the variance μ^2 (μ is the standard deviation), the (an)isotropy parameter γ, the mean-squared slope σ, and θ giving the direction of most rapid variation. Analysing the Ormen Lange topography, Hove (2003) suggested a method of estimating these parameters which is adopted in this study. The vector field $\mathbf{m}(\mathbf{x})$ as a finite difference approximation to $\nabla d(\mathbf{x})$ is given by

$$\mathbf{m}(\mathbf{x}) = \left(\frac{d(\mathbf{x}+\Delta x) - d(\mathbf{x})}{\Delta x}, \frac{d(\mathbf{x}+\Delta y) - d(\mathbf{x})}{\Delta y} \right) . \tag{6}$$

We then define the vector sum as

$$\mathbf{M} = \frac{1}{n} \sum_{\mathbf{x}} \frac{\mathbf{m}(\mathbf{x})}{|\mathbf{m}(\mathbf{x})|} , \tag{7}$$

where n is the number of grid points. Then the sub-grid-scale topography parameters are given by

$$\mu^2 = \frac{1}{A} \int \int \left(d - \bar{d}\right)^2 \, dA \,, \tag{8a}$$

$$\gamma = \sqrt{1 - |\mathbf{M}|} \,, \tag{8b}$$

$$\sigma = \frac{1}{n} \sum_{\mathbf{x}} |\mathbf{m}(\mathbf{x})| \,, \tag{8c}$$

$$\theta = \arctan\left(\frac{M_y}{M_x}\right) \,. \tag{8d}$$

In Eq. 8d M_x and M_y denote the x- and y-component, respectively, of the vector sum $\mathbf{M}$. For the domain in this study, the following parameter values are obtained: $\mu = 5.80\,\mathrm{m}$, $\sigma = 0.56$, $\gamma = 0.94$ and $\theta = 1.35$ radian. Using μ, σ, γ and θ, an obstacle representative of the entire GPR topography can be obtained with height 2μ and known shape and orientation. The actual topography is now conceptually replaced by repetitions of this representative obstacle within the computational domain. The problem of specifying the effect of the complex terrain on the flow reduces to specifying the effect of this single obstacle.

5. Results and discussion

5.1. Drag states

In Fig. 3 the domain integrated kinetic ($\mathcal{E}_k$), available potential ($\mathcal{E}_{ap}$), potential ($\mathcal{E}_p$) and background potential ($\mathcal{E}_{ps}$) energies have been calculated for both the linear (run1) and hyperbolic tangent (run3) density profiles. The domain integrated energies are calculated following Molemaker and McWilliams

(2010):

$$\mathcal{E}_k = \int_V E_k \, dx \, dy \, dz \,, \tag{9a}$$

$$\mathcal{E}_p = \int_V E_p \, dx \, dy \, dz \,, \tag{9b}$$

$$\mathcal{E}_{ps} = \int_V E_{ps} \, dx \, dy \, dz \,, \tag{9c}$$

$$\mathcal{E}_{ap} = \int_V E_{ap} \, dx \, dy \, dz \,, \tag{9d}$$

where the energy densities are defined as

$$E_k = \frac{1}{2}\left(u^2 + v^2 + w^2\right) \,, \tag{10a}$$

$$E_p = zb \,, \tag{10b}$$

$$E_{ps} = z\bar{b}_s \,, \tag{10c}$$

$$E_{aps} = \frac{\left(b_s - \bar{b}_s^2\right)}{2\delta_z \bar{b}_s} \,, \tag{10d}$$

$$E_{ap} = E_p - E_{ps} + E_{aps} \,. \tag{10e}$$

Here $b = g(1 - \rho/\rho_0)$ is the buoyancy field proportional to the density ρ and b_s is a buoyancy field resulting from sorting the density field following a technique proposed by Winters et al. (1995). A sorting algorithm is applied assigning the densest fluid to the grid boxes with the lowest vertical coordinate. Following Molemaker and McWilliams (2010), the available potential energy of the sorted buoyancy field is added in the calculation of E_ap to correct for the deviation of the available potential energy of the sorted field (dependent on the grid) from a horizontally uniform profile. The overbar denotes a horizontal average. The model was run for 14 hours until the energy stabilizes with time so that the dynamics is not dominated by the external

forcing of the model. The kinetic energy and the available potential energy stabilize within 3 hours after the spin-up of the velocity, while the potential energy needs longer time to stabilize due to the different outflow boundary condition on the density field. The results from a 2-hour period between 8.5 and 10.5 hours is selected for further investigation.

The time average of the perturbation velocity along a section at y=200 m, calculated by subtracting the average velocity in the y-direction along the section (see Eq. 11), is shown for run1 to run3 in Fig. 4, together with the density fields. In all the cases the potential density surfaces and the horizontal velocity field are significantly affected by the topography. The maximum velocities are 0.20 m s^{-1}, 0.15 m s^{-1}, and 0.17 m s^{-1} for run1, run2, and run3, respectively, and the minimum velocities are -0.05 m s^{-1}, -0.05 m s^{-1}, and -0.07 m s^{-1}. The only difference between the three cases is the stratification which has a major impact on the wave/non-wave regime of the flow, and affects the velocity maxima and the drag exerted in the water column. Different from run2 and 3, the constant buoyancy frequency in run1 is such that the non-dimensional height is less than unity (Table 1), and the flow is expected to be linear, with no overturning internal waves. To generate propagating waves, according to linear theory of two-dimensional waves, the intrinsic frequency of the waves (U/L) must be smaller than the buoyancy frequency. This leads to a limit on the horizontal length scale of the topography, $L > 2\pi N/U$, approximately 110 m for run1 and 60 m and 50 m for run2 and run3, respectively, using the background velocity u_0. This calculation supports the difference as seen particularly between run1 and run2 in that the latter supports propagating waves, while the former will generate evanescent

wave solutions as oscillations at frequencies above the buoyancy frequency are not supported. Although the mode number, K, for run1 is sub-critical for the lowest mode (K>1) and the non-dimensional mountain height is sub-critical with respect to the typical mountain height of the domain, locally h_n exceeds the critical limit. The flow is then non-linear and goes through a "hydraulic transition" which is the case in run1 (Fig. 4a). In run1 the flow is partially blocked only behind the obstacles where the critical limit is exceeded (Fig. 4a) (i.e., no discernible perturbations are seen in transects away from the "critical" obstacles). In run2 and run3, on the other hand, propagating non-linear waves are seen and the drag on the flow is distributed throughout the entire domain (not confined to a few topographic features). Nevertheless, the drag exerted on the flow by the topography in run1 is significant and comparable in magnitude to run2 and run3. This is illustrated by showing the percentage change of the horizontally averaged velocity with respect to the background velocity u_0 (Fig. 5). In run1 significant drag occurs near the depth corresponding to $Nz/u_0 = \pi$, and the average velocity is reduced by more than 20%. The largest decrease in relative velocity is due to flow blockage in run1, whereas bottom drag is largest in the bottom-most layer in run2 and run3. Internal wave drag acts at run2, decreasing continuously with increasing height above bottom. For the more realistic N-profile of run3, drag is concentrated at the pycnocline centered at a $\sim$20 m thick layer between $\pi < Nz/u_0 < 2\pi$.

A proxy is calculated for the turbulent kinetic energy (TKE) by assuming that cross-stream averages describe both the mean current and velocities associated with internal waves (Skyllingstad and Wijesekera, 2004). Com-

puting the perturbations u, v, and w by (for the u-component)

$$u' = u - \frac{1}{n_y} \sum_y u(x, y, z)\,, \tag{11}$$

where n_y is the number of grid points in the cross-stream direction, an estimate of the turbulent kinetic energy is expressed by
$TKE = 1/2(u'^2 + v'^2 + w'^2)$. The fields of TKE for run1, run2 , and run3 are shown in Fig. 6, and support the inferences from percent-change velocity profiles (Fig. 5). The maximum reduction of the background flow due to drag induced by the gravity waves observed in run3 (Fig. 5c) is restricted to the stratified zone where the buoyancy frequency is large enough for the waves to break. This is also evident in the cross-stream averaged TKE from run3 (Fig. 6b) compared to run2 where high levels of TKE is present in most of the domain. In run1, TKE is elevated closer to the bottom in the vicinity of large obstacles (not seen in the average topography). TKE integrated over the domain is $1.27{\times}10^5\,\mathrm{m^5\,s^{-2}}$, $2.80{\times}10^5\,\mathrm{m^5\,s^{-2}}$, and $0.71{\times}10^5\,\mathrm{m^5\,s^{-2}}$ for run1, run2, and run3, respectively, confirming run2 as the most turbulent. With the highest vertical mode number and non-dimensional obstacle heights well above the critical for the major topographic features, blocked flow drag at low levels and several vertical wave components are expected, both clearly visible in Fig. 4b and Fig. 5b. The maximum reduction in the velocity close to the topography is a combination of the blocked flow drag and the first of the three vertical wave components.

5.2. Mixing

Given the open boundaries, the rate of change in the domain-integrated background potential energy cannot be used as a proxy for mixing. To di-

agnose the bulk measure for mixing a method suggested by Burchard and Rennau (2008) is adopted. For a conservative tracer without any internal sources or sinks, a conservation equation for the square of the mean tracer is developed assuming that the turbulent fluxes can be parameterized as down-gradient fluxes with different diffusivities in the horizontal and in the vertical direction:

$$\begin{aligned}\partial_t\left(s^2\right)+\left(v_j\partial_j\right)\left(s^2\right)-\partial_x\left(k_h\partial_x\left(s^2\right)\right)-\partial_y\left(k_h\partial_y\left(s^2\right)\right)-\partial_z\left(k_z\partial_z\left(s^2\right)\right) \quad (12)\\ =-2k_h\left(\partial_x s\right)^2-2k_h\left(\partial_y s\right)^2-2k_z\left(\partial_z s\right)^2\equiv -D^{phys}\left(s^2\right)\,,\end{aligned}$$

where s is a tracer (in our case density), k_h and k_z the horizontal and vertical turbulent diffusivities, and the spatial partial derivative is defined as $\partial_i = \partial/\partial_{x_i}$ with indices $i,j = 1,2,3$ defining the spatial coordinates x_i ($x_1 = x$, $x_2 = y$ and $x_3 = z$). The terms on r.h.s of Eq. 12 denote the turbulent mean tracer variance decay, D^{phys}, shown to be a suitable measure for mixing. Burchard and Rennau (2008) also present a method for quantifying the numerical mixing (due to the advection scheme) in ocean models by calculating the numerically induced tracer variance decay:

$$D^{num}\left\{\left(s^n_{p,q,r}\right)^2\right\}_{i,j,k}=\frac{A\left\{\left(s^n_{p,q,r}\right)^2\right\}_{i,j,k}-\left(A\left\{s^n_{p,q,r}\right\}_{i,j,k}\right)^2}{\Delta t}\,, \qquad (13)$$

where A is the advection operator of the numerical model and Δt is the model time step. D^{num} is quantified by diagnostically applying the advection operator on the square of the tracer field and subtract the square of the advected tracer field for each time step. The resulting D^{phys} and D^{num} after applying these two methods on our results are presented in Fig. 7a-d. Strong tracer gradients and increased velocities associated with the internal

waves induce numerical mixing orders of magnitude greater than the physical mixing in some locations (compare Fig. 4 with Fig. 7). This is consistent with the results of Rennau and Burchard (2009) for the Arkona Sea. The patches of high variance decay are always associated with negative (anti-diffusive) variance decay of the same magnitude. The former is an effect of the TVD scheme limiter ensuring monotonicity, and the latter is an effect of the non-monotone, higher-order (2nd order accurate) scheme. Similar behaviour is found by Burchard and Rennau (2008). The volume-integrated variance decay is -0.3$\times10^{-3}\,\mathrm{kg^2\,m^{-3}\,s^{-1}}$ and -5.9$\times10^{-3}\,\mathrm{kg^2\,m^{-3}\,s^{-1}}$ for run1 and run3, respectively. The negative values are due to the anti-diffusive properties of the superbee-limited (TVD) advection scheme. The volume-integrated physical mixing is $1.2\times10^{-6}\,\mathrm{kg^2\,m^{-3}\,s^{-1}}$ and $3.4\times10^{-6}\,\mathrm{kg^2\,m^{-3}\,s^{-1}}$.

The vertical diffusivity associated with the numerical mixing can be estimated by $\nu_z^{num} = D^{num}/2(\partial_z s)^2$. As a result of anti-diffusive D_{num}, vertical numerical diffusivity has both negative and positive contribution presented separately in Fig. 7e-h, averaged in the cross-stream section along x. Horizontally averaged profiles are then presented for run1 and run3 (Fig. 8). The depth of the maximum vertical diffusivity is not necessarily co-located with the maximum variance decay due to the inverse dependence on the vertical tracer gradient. Particularly for run1, the maximum vertical diffusivity is associated with small $\partial_z s$, while the variance decay has maxima and minima where the velocity and gradients are large. Run3 has slightly higher numerical diffusivities compared to run1 (Fig. 7e-h and Fig. 9) and is also more strongly dominated by negative contribution. The distribution of positive and negative contributions to ν_z^{num} is obtained by counting the number of

occurrences in bins of ν_z^{num} (Fig. 9). While the opposing contributions are evenly distributed in run1, run3 shows more frequent occurrences of negative diffusion, particularly in the range $10^{-3} < \nu_z^{num} < 10^{-2}$, which densely populates the domain.

5.3. Parameterization of topographic drag

Generally the drag exerted by the topography on the flow can be described by two conceptual models, whose relevance depends on the non-dimensional mountain height (Lott and Miller, 1997). At small h_n the flow is forced over the mountain and the vertical motion of the fluid forces gravity waves. The surface stress due to these gravity waves has a magnitude given by Eq. (4) or similar expressions (Palmer et al., 1986; Kim and Arakawa, 1995; Lott and Miller, 1997). At large h_n, the vertical motion of the fluid is limited and the low level flow has to flow around the mountains, effectively reducing h in Eq. (4) and introducing a drag on the flow due to the blocked flow at low levels. Following Lott and Miller (1997) the depth of the blocked layer can be expressed as $z_b/h = \max[0, (h_n - h_{nc})/h_n]$, where h_{nc} is a critical non-dimensional mountain height of order unity. In this study $h_n < 1$ at low levels for all cases except run2, and the blocked flow drag has an insignificant contribution to the total drag on the flow, especially for the cases with a hyperbolic tangent density profile.

We have also tested an additional case with drag due to the blocked flow parameterized following Lott and Miller (1997) and using the linear density profile of run2 such that $h_n > 1$ (results not shown). This results in a blocked flow layer depth of approximately half the typical mountain height (6-7 m), and shows increased drag at the bottom and a well mixed layer with

a thickness in the order of z_b. Above the blocked layer, the magnitude of the gravity wave drag can be estimated from the vertical wave momentum flux, assuming linear, hydrostatic waves

$$\tau = -\rho_0 \overline{u'w'} = \frac{1}{2}\rho k U N \delta h^2 \,, \tag{14}$$

where the vertical wavenumber m is replaced by N/U (the hydrostatic dispersion relation is $m = N/U$ when $k^2 \ll m^2$, k being the horizontal wavenumber). Depending on the horizontal wavenumber, evanescent ($k > N/U$) or propagating ($k < N/U$) wave solutions may be expected, but only the latter results in a pressure gradient over the topography and an associated drag force. Adding the wave drag Eq. (14) of all mountains within a GPR leads to Eq. (5). For hydrostatic waves, their impact on the local static stability and shear may be combined to form a minimum local Richardson number representing the smallest Ri achieved under the influence of internal gravity waves

$$Ri_m = Ri \frac{1 - \frac{N}{U}\delta h}{\left(1 + Ri^{1/2}\frac{N}{U}\delta h\right)^2} \,. \tag{15}$$

The presence of the waves may lead to local instability in a stable background flow either by a convective overturning mechanism (numerator of Eq. (15) becomes small) or by a billow instability mechanism (denominator of Eq. (15) becomes large) (Palmer et al., 1986). By defining a critical Ri (typically $Ri_c = 0.25$) and employing a saturation hypothesis (Lindzen, 1981), the vertical distribution of the gravity wave drag is estimated. When $Ri_m < Ri_c$, instability results in turbulent dissipation of the wave such that its amplitude is reduced until it regains stability. Below this critical level $\tau = \tau_s$, from the Eliassen-Palm theorem, for vertically propagating waves in

the absence of transience and dissipation. If N is constant, the wave amplitude must increase with height as the density is reduced, until the wave becomes unstable. In the case with a hyperbolic tangent profile, $N \approx 0$ at low levels; the minimum Richardson number formulation fails in the nearly neutral stratification at low levels. Consequently a simpler scheme is applied where the wave amplitude is assumed to be equal to the typical mountain height, $\delta h = h = 2\mu$, at low levels as $N \approx \partial\rho/\partial z \approx 0$, and wave breaking is assumed to commence at the level where δh equals the saturation wave amplitude given by $\delta h_{sat} = U/N$. From Eq. (15) this corresponds to the purely convective instability limit and is a strict requirement, but due to the low buoyancy frequency at low levels, attenuation of the wave amplitude with height (evanescent modes) may be expected, and δh is probably overestimated.

We conduct two runs (run4 and run5) to test the topographic drag parameterization, each with hyperbolic tangent density profile and the Mellor and Yamada (1982) 2-1/2 level turbulence closure scheme (MY2.5). The only difference is that run4 employs the resolved topography, whereas run5 has flat bottom but includes the wave drag parameterization. Velocity and density distributions at y=200 m are contrasted in Fig. 10. As the Ri drops below the critical level (and even becomes negative by wave overturning, see Fig. 4c), the turbulence closure prohibits the overturning waves by increasing the vertical diffusivity. This results in well-mixed neutrally stratified patches visible in Fig. 10a. Otherwise the results from run4 are qualitatively similar to run3 in both velocity and density distribution (compare Fig. 4c and 10a), and the cross-stream averaged TKE (compare Fig. 6c and 11a). The only difference

between run3 and run4 is that the MY2.5 closure applied in run4 is absent in run3. When applying the gravity wave parameterization (run5), the turbulence closure is retained as it smooths the strong velocity gradients imposed by the parameterization of the wave drag. Because the domain resembles one GPR, a horizontally constant drag was applied throughout the domain, resulting in the smoother velocity (Fig. 10b) and TKE shown in Fig. 11b, where the latter is approximately two orders of magnitude smaller compared to run4 and run5. Due to the constant wave drag, the estimation of the TKE by subtracting the cross-stream averaged velocity is not applicable in the case of run5. With no significant wave activity in run5 (due to the constant drag and lack of topography), the TKE may be estimated by removing the background velocity resulting in a domain integrated TKE of $0.65\times10^5\,\mathrm{m^5\,s^{-2}}$ in better agreement with the resolved topography results ($0.71\times10^5\,\mathrm{m^5\,s^{-2}}$ for run3 and $0.76\times10^5\,\mathrm{m^5\,s^{-2}}$ for run4). The similarity between run3 and run4 is confirmed by the percentage change of the horizontally domain-averaged and time-averaged velocity relative to the background velocity (Fig. 12). In run5, although remarkably similar in the domain average TKE, the wave drag is deposited over a too shallow layer resulting in an overestimated drag and consequently a larger reduction of the velocity in the layer where the wave parameterization predicts wave breaking (Fig. 11c).

The volume-integrated variance decay of run4 and run5 is $-4.3\times10^{-3}\,\mathrm{kg^2\,m^{-3}\,s^{-1}}$ and $-1.63\times10^{-3}\,\mathrm{kg^2\,m^{-3}\,s^{-1}}$, respectively. This is the same order of magnitude as run3, but somewhat smaller due to the smoother density fields in run4 and run5. In Fig. 13 the vertical profile of the diffusivity estimated from D_{num} is shown together with the vertical diffusivity from the

turbulence closure. In contrast to the runs with constant diffusivities, the volume averaged D_{phys} is $1.4\times10^{-2}\,\mathrm{kg^2\,m^{-4}\,s^{-1}}$ for run4, several orders of magnitude larger, and approximately one order of magnitude larger compared to the numerical diffusivity. The zero numerical diffusivity near the bottom and towards the surface in run4 (and run3) is due to the vanishing vertical density gradient.

6. Concluding remarks

Numerical simulations of stratified flow over complex topography have been performed using a high-resolution, non-hydrostatic ocean model, to study the drag exerted on the flow by bottom obstacles. Several runs with various stratification but with realistic topography are discussed. A final simulation is made over flat bottom using a parameterization for the internal gravity wave drag which represents the combined effect of the real topography in terms of its statistical properties. Depending on the stratification, the drag on the flow is described by three different processes, acting separately or in combination; internal wave drag, blocked flow drag, and hydraulic drag. Three cases with a hyperbolic tangent density profile, resembling the well mixed bottom layer and the stratified interface of the Faroe Bank Channel overflow, were performed to illustrate the possible interfacial mixing caused by rough bottom topography. The simulations show that the complex bottom topography leads to wave overturning and significant mixing in the stratified interface. The drag exerted on the flow as internal waves break reduces the horizontally domain averaged velocity by up to 27% in the stratified interface, imposing a strong shear on the flow. The internal wave drag pa-

rameterization, tested on the hyperbolic tangent case, yields reasonable levels of turbulent kinetic energy and predicts wave breaking at the correct level compared to the simulation with resolved topography. The depth of the layer where the wave breaking is effective, however, is underestimated, leading to an overestimated wave drag in the layer.

Acknowledgements

This work is funded through the Academia agreement between the Norwegian University of Science and Technology and Statoil ASA. The author wishes to thank Helge Avlesen for providing the topography for the model and help with model set-up.

Baines, P. G., 1979. Observations of stratified flow over two-dimensional obstacles in fluid of finite depth. Tellus 31, 351–371.

Baines, P. G., 1995. Topographic Effects in Stratified Flows. Cambridge Monographs on Mechanics. Cambridge University Press.

Berntsen, H., Kowalik, Z., Sælid, S., Sørli, K., 1981. Efficient numerical simulation of ocean hydrodynamics by a splitting procedure. Model. Ident. Control 2, 181–199.

Berntsen, J., 2000. USERS GUIDE for a modesplit σ-coordinate numerical ocean model. Tech. Rep. 135, Dept. of Applied Mathematics, University of Bergen, Johs. Bruns gt.12, N-5008 Bergen, Norway, 48p.

Blumberg, A. F., Mellor, G. L., 1987. A description of a three-dimensional coastal ocean circulation model. In: Heaps, N. (Ed.), Three-Dimensional Coastal Ocean Models. Vol. 4 of Coastal and Estuarine Series. American Geophysical Union, pp. 1–16.

Burchard, H., Rennau, H., 2008. Comparative quantification of physically and numerically induced mixing in ocean models. Ocean Model. 20, 293–311.

Fer, I., Voet, G., Seim, K. S., Rudels, B., Latarius, K., 2010. Intense mixing of the Faroe Bank Channel overflow. Geophys. Res. Lett. 37, L02604, doi:10.1029/2009GL041924.

Hove, J., 2003. Statistical properties of the sea bottom in the ormen lange area. Tech. Rep. 3, UNIFOB, Bergen Center of Computational Science, Computational Mathematics Unit.

Huppert, H. E., Miles, J. W., 1969. Lee waves in a stratified flow. Part 3. Semi-elliptical obstacle. J. Fluid Mech. 55, 481–496.

Kim, Y.-J., Arakawa, A., 1995. Improvement of orographic gravity wave parameterization using a mesoscale gravity wave model. J. Atmos. Sci. 52, 1875–1902.

Kowalik, Z., Murty, T. S., 1993. Numerical Modeling of Ocean Dynamics. Vol. 5 of Advanced Series on Ocean Engineering. World Scientific.

Lamb, K. G., 1994. Numerical experiments of internal wave generation by strong tidal flow across a finite amplitude bank edge. J. Geophys. Res. 99, 843–864.

Ledwell, J. R., Montgomery, E., Polzin, K. L., Laurant, L. C. S., Toole, J., 2000. Evidence for enhanced mixing over rough topography in the abyssal ocean. Nature 403, 179–182.

Lindzen, R. S., 1981. Turbulence and stress owing to gravity wave and tidal breakdown. J. Geophys. Res. 86 (C10), 9707–9714.

Long, R. R., 1955. Some aspects of the flow of stratified fluids. III. Continuous density gradients. Tellus 7, 341–357.

Lott, F., Miller, M. J., 1997. A new subgrid-scale orographic drag parametrization: Its formulation and testing. Quarterly Journal of the Royal Meterorological Society 123, 101–127.

Martinsen, E. A., Engedahl, H., 1987. Implementation and testing of a lateral

boundary scheme as an open boundary condition in a barotropic ocean model. Coast. Eng. 11, 603–627.

Mellor, G. L., 1996. Users guide for a three-dimensional, primitive equation, numerical ocean model. Tech. rep., Princeton University.

Mellor, G. L., Yamada, T., 1982. Development of a turbulence closure model for geophysical fluid problems. Rev. Geophys. Space Phys. 20, 851–875.

Molemaker, M. J., McWilliams, J. C., 2010. Local balance and cross-scale flux of available potential energy. J. Fluid Mech. 645, 295–314.

Palmer, T. N., Shutts, G. J., Swinebank, R., 1986. Allevation of a systematic westerly bias in circulation and numerical weather prediction models through an orographic gravity-wave drag parameterization. Quart. J. Roy. Meteor. Soc. 112, 1001–1039.

Peters, H., Johns, W. E., 2005. Mixing and entrainment in the Red Sea outflow plume. Part II: Turbulence characteristics. J. Phys. Oceanogr. 35, 584–600.

Polzin, K. L., Toole, J. M., Ledwell, J. R., Schmitt, R. W., 1997. Spatial variability of turbulent mixing in the abyssal ocean. Science 276, 93–96.

Rennau, H., Burchard, H., 2009. Quantitative analysis of numerically induced mixing in a costal model application. Ocean Dynam. 59, 671–687.

Seim, K. S., Fer, I., 2010. Mixing in the stratified interface of the Faroe Bank Channel overflow: the role of transverse circulation and internal waves. submitted to J. Geophys. Res.

Seim, K. S., Fer, I., Berntsen, J., 2010. Regional simulations of the Faroe Bank Channel overflow using a σ-coordinate ocean model. Ocean Model. 35, 31–44.

Skyllingstad, E. D., Wijesekera, H. W., 2004. Large-eddy simulation of flow over two-dimensional obstacles: High drag states and mixing. J. Phys. Oceanogr. 34, 94–112.

Thurnherr, A. M., 2006. Diapycnal mixing associated with an overflow in a deep submarine canyon. Deep-Sea Res. II 53, 194–206.

Winters, K. B., Lombard, P. N., Riley, J. J., D'Asaro, E. A., 1995. Available potential energy and mixing in density-stratified fluids . J. Fluid Mech. 289, 115–128.

Yang, H. Q., Przekwas, A. J., 1992. A comparative study of advanced shock-capturing schemes applied to Burgers equation. J. Comput. Phys. 102, 139–159.

Table 1: Parameters for different experiments.

Run	Dens. prof.	$u_0(m\,s^{-1})$	$N(s^{-1})$	h_n	K
run1	linear	0.1	5.7×10^{-3}	0.7	3.2
run2	linear	0.1	1.0×10^{-3}	1.2	5.8
run3	tanh	0.1	1.2×10^{-2} [e]	1.2[a]	5.4 (3.1[b])
run4[c]	tanh	0.1	1.2×10^{-2} [e]	1.2	5.4 (3.1)
run5[d]	tanh	0.1	1.2×10^{-2} [e]	1.2	5.4 (3.1)

[a] h_n is calculated where N is non-zero (50 to 100 m).

[b] If d_0 is taken to be the depth of the dense water (below 75 m).

[c] With turbulence closure.

[d] With turbulence closure and gravity wave drag parameterization.

[e] Maximum buoyancy frequency.

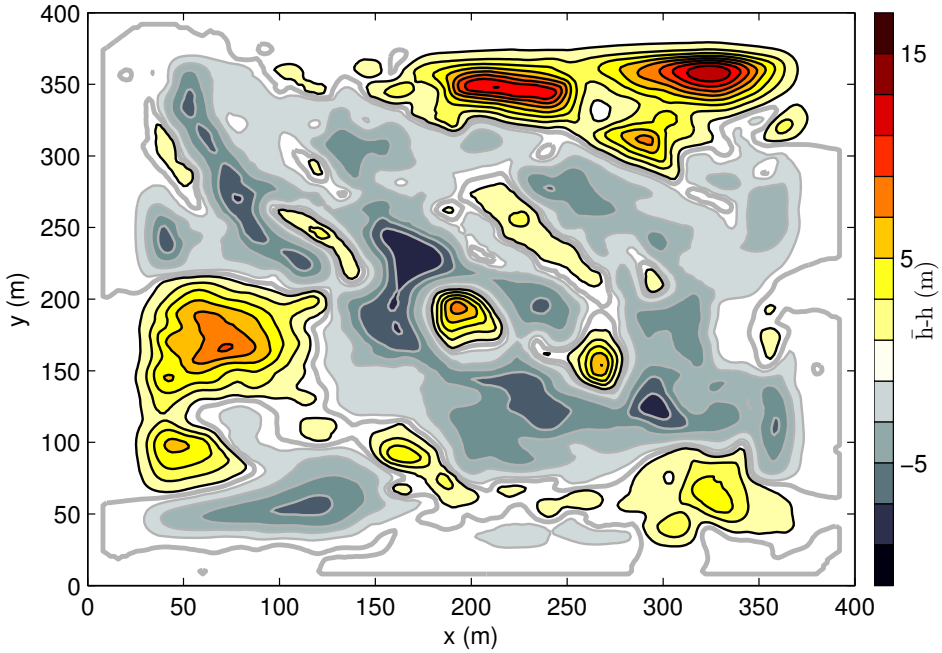

Figure 1: Bottom topography deviation from mean depth. Positive deviations (crests) are contoured in warm colours and black lines, while negative deviations (troughs) are contoured in cool colours and grey lines. The white color marks the interval between -1 and 1 m and the thick grey line is the zero contour.

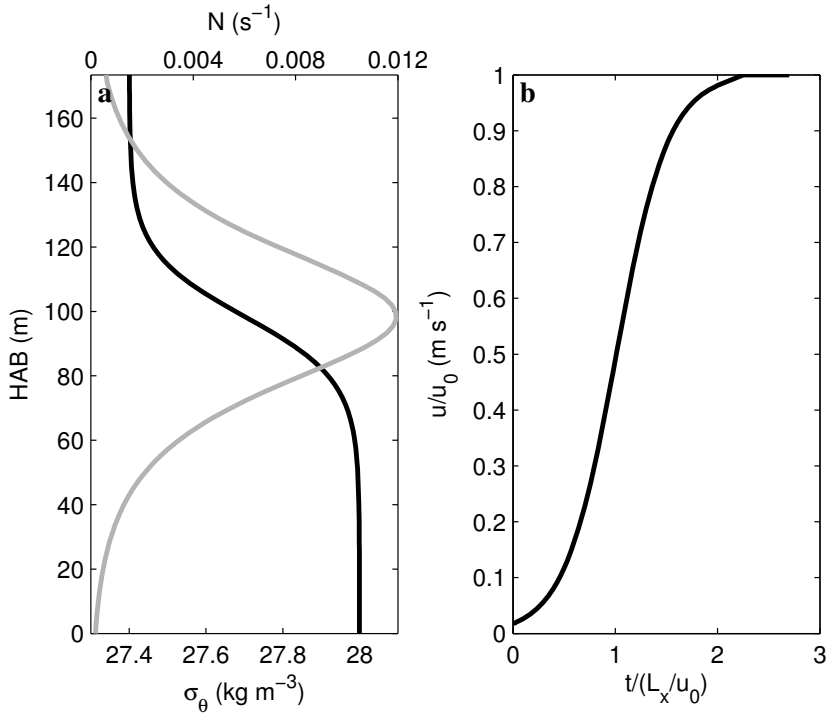

Figure 2: (a) Initial hyperbolic tangent density (black) and buoyancy frequency (grey) profile, and (b) spin up of the inflow velocity with time towards the background velocity u_0. The time is non-dimensional and L_x is the length of the domain in the x-direction.

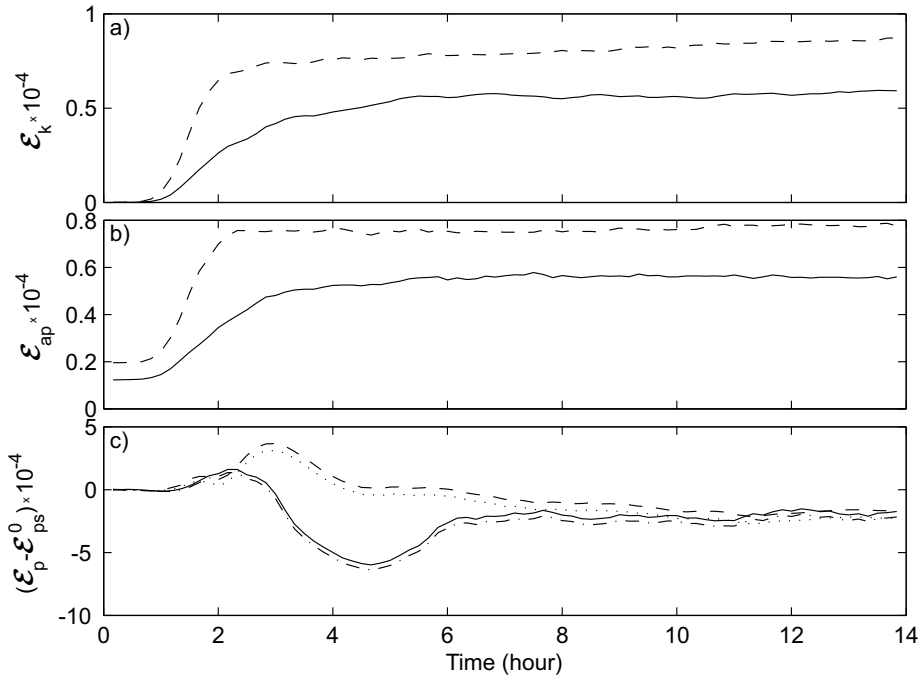

Figure 3: Time evolution of the domain integrated (a) kinteic energy ($\mathcal{E}_k$), (b) available potential energy ($\mathcal{E}_{ap}$) and (c) potential energy ($\mathcal{E}_p$) relative to the initial background potential energy ($\mathcal{E}^0_{ps}$), for run1 (dashed) and run2 (solid). In (c) background potential energy ($\mathcal{E}_{ps}$) relative to $\mathcal{E}^0_{ps}$ is also shown (run1, dotted; run3, dash-dot).

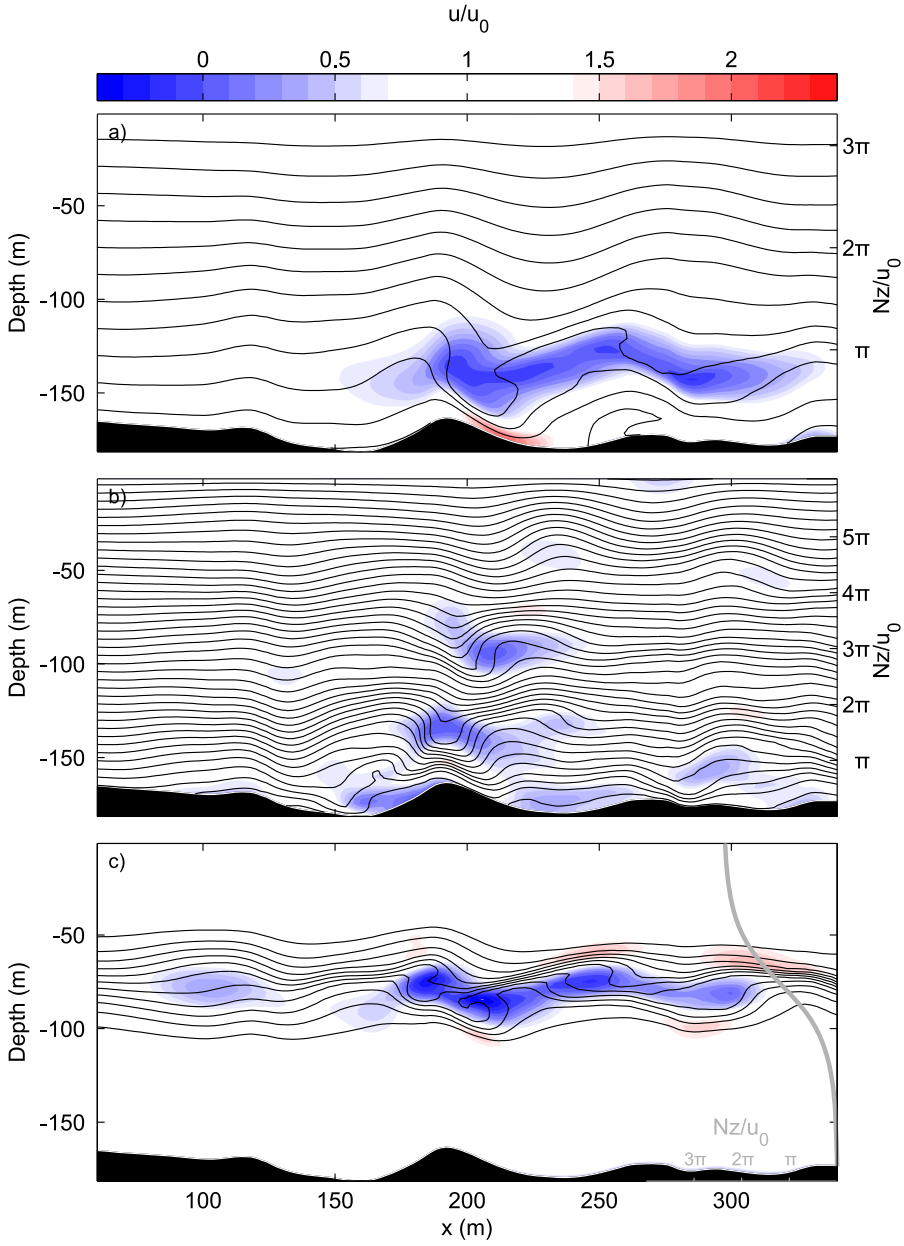

Figure 4: Vertical cross section of potential density and the horizontal velocity, u, normalized by u_0 for (a) run1, (b) run2, and (c) run3, at y=200 m averaged over the period from approximately 8.5 to 10.5 hours. For (a) and (b), with N=constant, the vertical axis on the right is the vertical phase of a linear wave solution with vertical wave number $k = N/u_0$. The profile of Nz/u_0 is shown for (c). Density contours are drawn with 0.05 kg m^{-3} intervals.

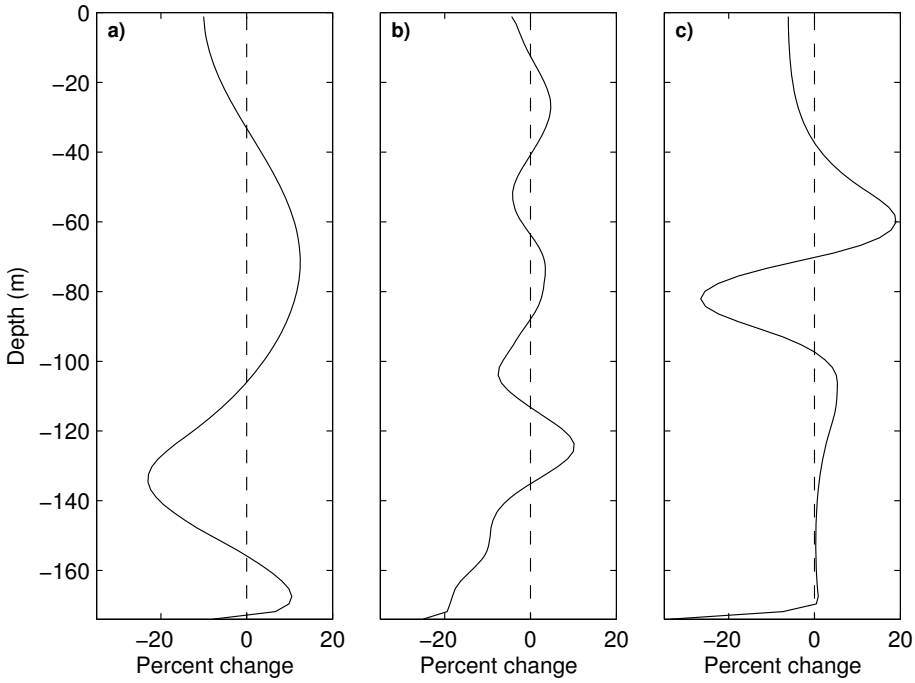

Figure 5: Vertical profile of the percent change of the horizontally domain averaged and time averaged (8.5 to 10.5 hours) u component of velocity relative to the background velocity u_0 for (a) run1, (b) run2, and (c) run3.

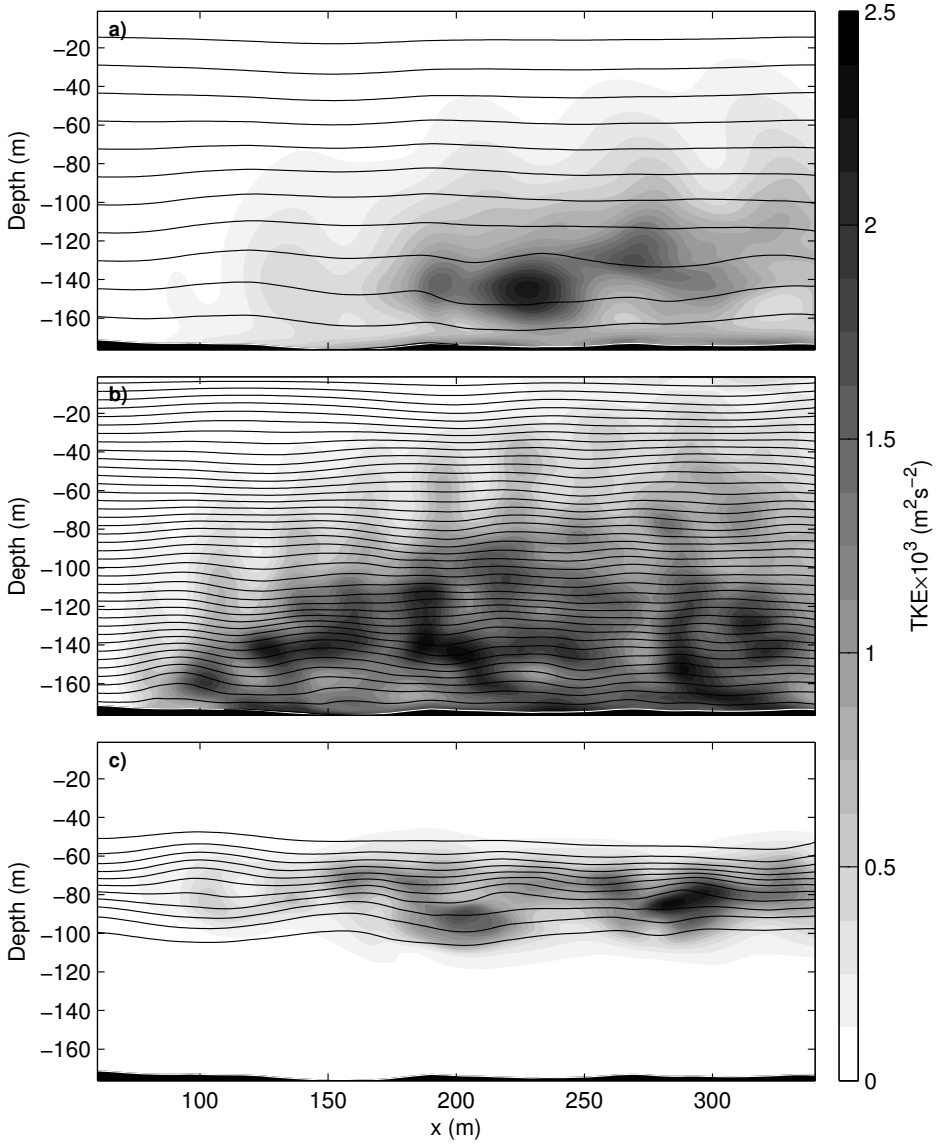

Figure 6: Cross-stream average of potential density and TKE averaged in time between 8.5 and 10.5 hours for (a) run1, (b) run2, and (c) run3.

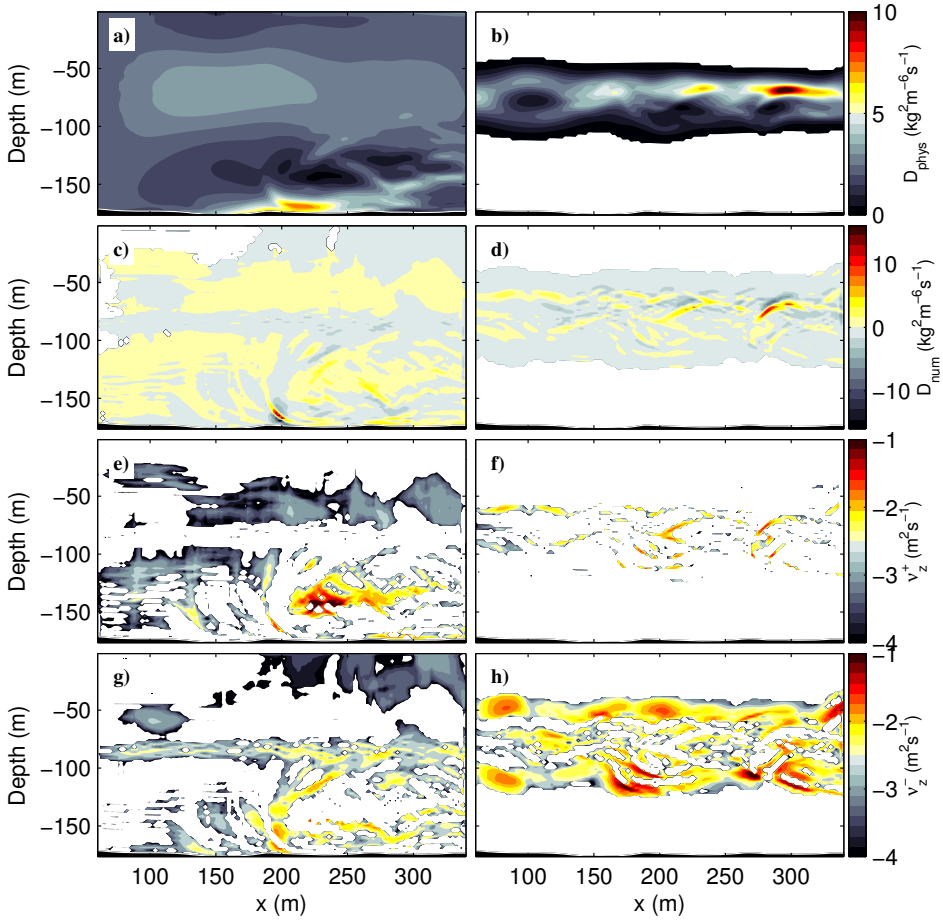

Figure 7: Physical mixing calculated according to Eq. 12 from (a) run1 ($10^{11} \times D_{phys}$) and (b) run3 ($10^{10} \times D_{phys}$), numerical mixing calculated according to Eq. 13 from (c) run1 ($10^7 \times D_{num}$) and (d) run3 ($10^6 \times D_{num}$), (e-f) positive and (g-h) negative numerical viscosity from run1, and run3, respectively. In (b) $10^{10} \times D_{phys} < 0.1$ is marked with white colour for clarity.

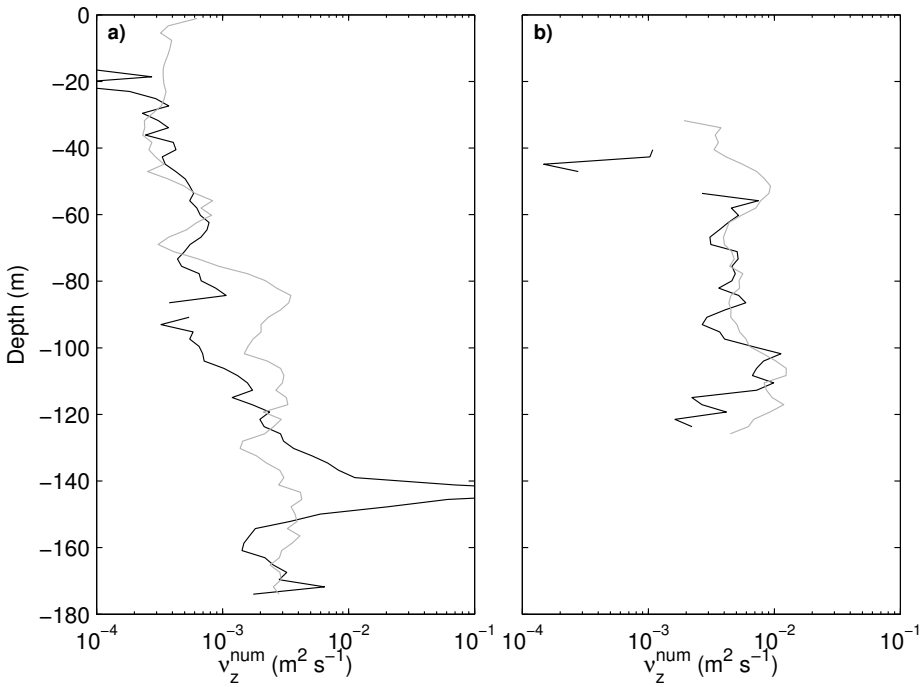

Figure 8: Vertical profile of the vertical diffusivity from (a) run1 and (b) run3, calculated from the volume-averaged D_{num}, time averaged between 8.5 to 10.5 hours. Positive (black) and negative (gray) contributions are shown separately. One data point for run1 at ∼145 m depth is off the scale with $\nu_z^{num} \sim 1\,\mathrm{m}^2\,\mathrm{s}^{-1}$.

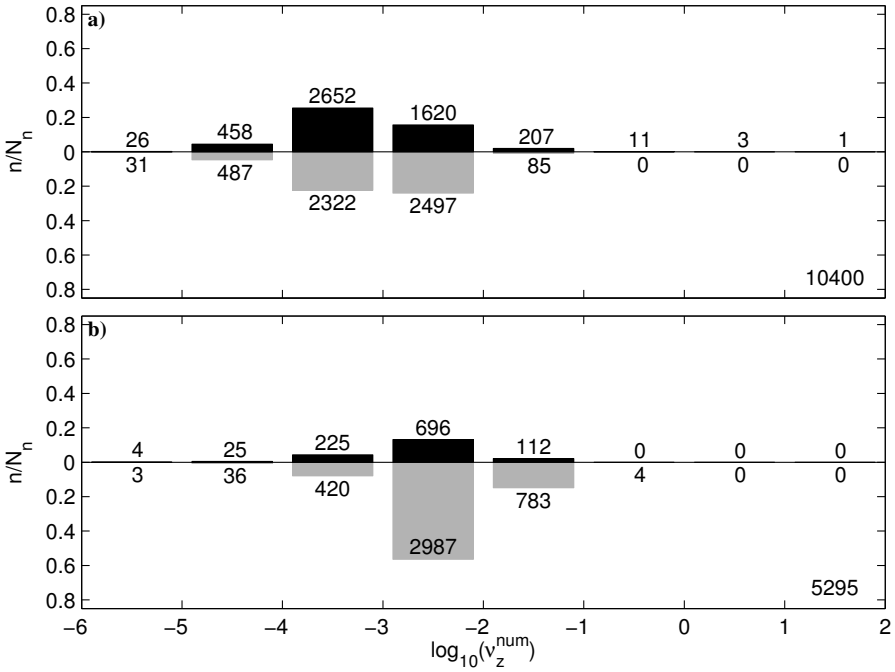

Figure 9: Distribution of the cross-stream averaged numerical diffusivity by the number of grid cells, n, with positive diffusivity (black bars) and negative diffusivity (grey bars) relative to the total number of cells with non-zero diffusivity, N_n, for (a) run1 and (b) run3. The number of cells for each diffusivity level is denoted over each bar and N_n in the lower right corner.

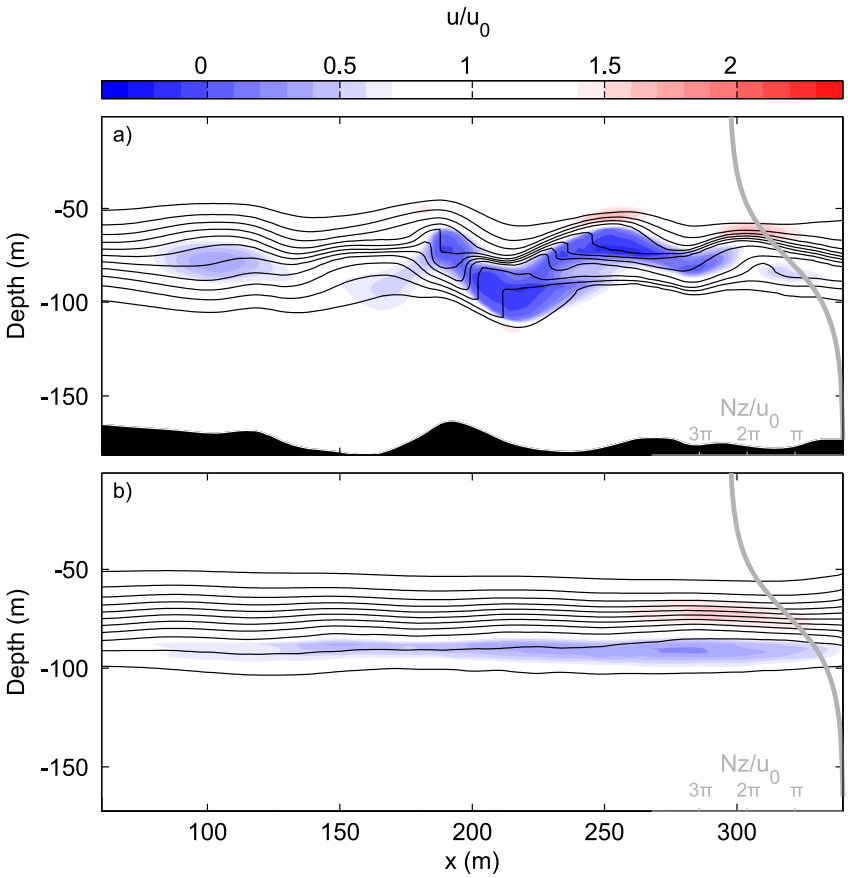

Figure 10: Vertical cross section of potential density and the horizontal velocity normalized by u_0 for (a) run4 and (b) run5 at y=200 m averaged over the period from approximately 8.5 to 10.5 hours. Density contours are drawn at 0.05 kg m^{-3} intervals.

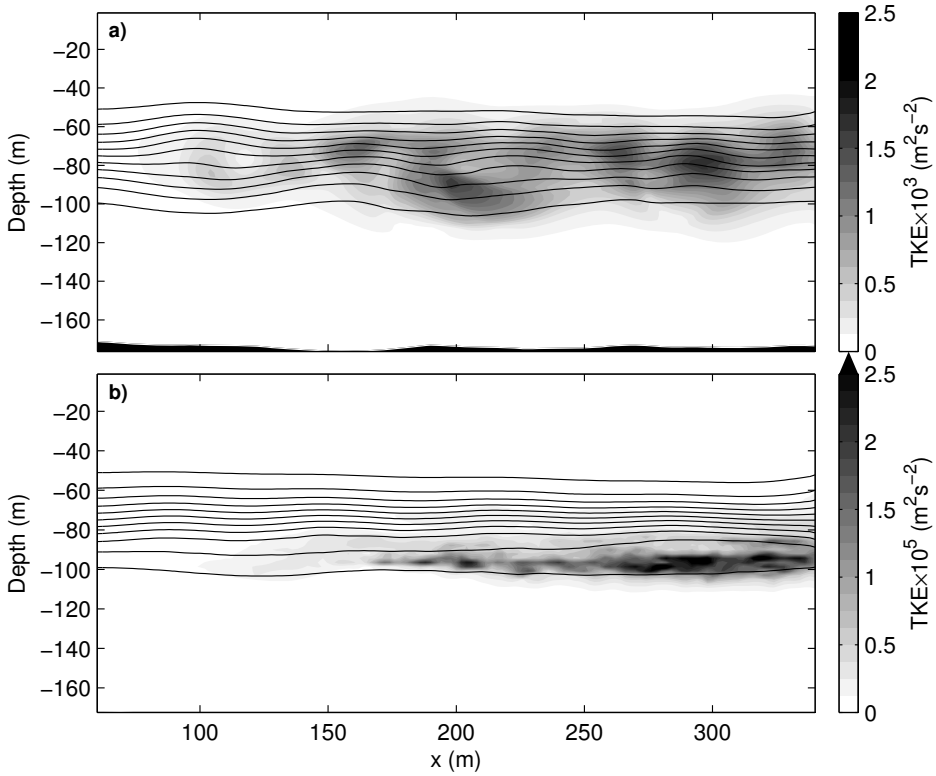

Figure 11: Cross-stream average of potential density and TKE averaged in time between 8.5 and 10.5 hours for (a) run4 and (b) run5.

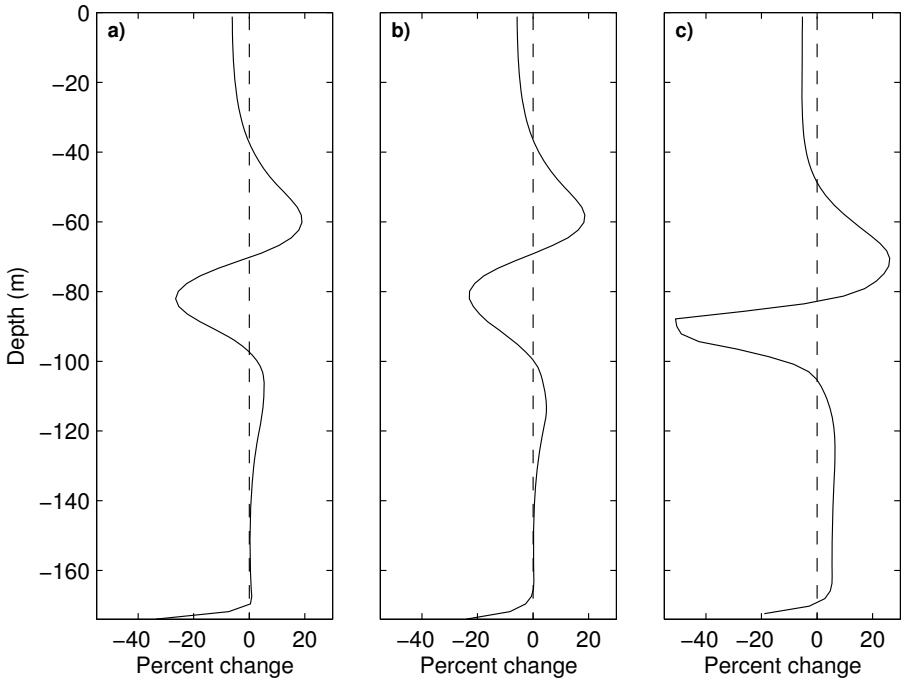

Figure 12: Vertical profile of the percent change of the horizontally domain averaged and time averaged (8.5 to 10.5 hours) u component of velocity relative to the background velocity u_0 for (a) run3, (b) run4, and (c) run5.

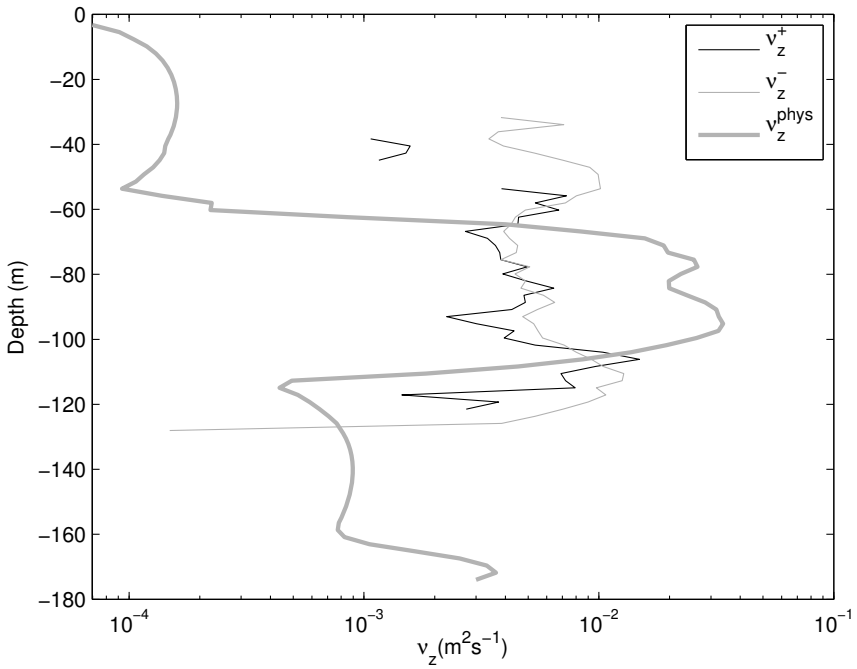

Figure 13: Vertical profile of the vertical diffusivity from run4 calculated from a horizontally averaged D_{num} time averaged over the period from 8.5 to 10.5 hours and the vertical diffusivity from the turbulence closure (grey).

R A P P O R T E R
UTGITT VED
INSTITUTT FOR MARIN TEKNIKK
(tidligere: FAKULTET FOR MARIN TEKNIKK)
NORGES TEKNISK-NATURVITENSKAPELIGE UNIVERSITET

Report No.	Author	Title
	Kavlie, Dag	Optimization of Plane Elastic Grillages, 1967
	Hansen, Hans R.	Man-Machine Communication and Data-Storage Methods in Ship Structural Design, 1971
	Gisvold, Kaare M.	A Method for non-linear mixed -integer programming and its Application to Design Problems, 1971
	Lund, Sverre	Tanker Frame Optimalization by means of SUMT-Transformation and Behaviour Models, 1971
	Vinje, Tor	On Vibration of Spherical Shells Interacting with Fluid, 1972
	Lorentz, Jan D.	Tank Arrangement for Crude Oil Carriers in Accordance with the new Anti-Pollution Regulations, 1975
	Carlsen, Carl A.	Computer-Aided Design of Tanker Structures, 1975
	Larsen, Carl M.	Static and Dynamic Analysis of Offshore Pipelines during Installation, 1976
UR-79-01	Brigt Hatlestad, MK	The finite element method used in a fatigue evaluation of fixed offshore platforms. (Dr.Ing. Thesis)
UR-79-02	Erik Pettersen, MK	Analysis and design of cellular structures. (Dr.Ing. Thesis)
UR-79-03	Sverre Valsgård, MK	Finite difference and finite element methods applied to nonlinear analysis of plated structures. (Dr.Ing. Thesis)
UR-79-04	Nils T. Nordsve, MK	Finite element collapse analysis of structural members considering imperfections and stresses due to fabrication. (Dr.Ing. Thesis)
UR-79-05	Ivar J. Fylling, MK	Analysis of towline forces in ocean towing systems. (Dr.Ing. Thesis)
UR-80-06	Nils Sandsmark, MM	Analysis of Stationary and Transient Heat Conduction by the Use of the Finite Element Method. (Dr.Ing. Thesis)
UR-80-09	Sverre Haver, MK	Analysis of uncertainties related to the stochastic modeling of ocean waves. (Dr.Ing. Thesis)
UR-81-15	Odland, Jonas	On the Strength of welded Ring stiffened cylindrical Shells primarily subjected to axial Compression

UR-82-17	Engesvik, Knut	Analysis of Uncertainties in the fatigue Capacity of Welded Joints
UR-82-18	Rye, Henrik	Ocean wave groups
UR-83-30	Eide, Oddvar Inge	On Cumulative Fatigue Damage in Steel Welded Joints
UR-83-33	Mo, Olav	Stochastic Time Domain Analysis of Slender Offshore Structures
UR-83-34	Amdahl, Jørgen	Energy absorption in Ship-platform impacts
UR-84-37	Mørch, Morten	Motions and mooring forces of semi submersibles as determined by full-scale measurements and theoretical analysis
UR-84-38	Soares, C. Guedes	Probabilistic models for load effects in ship structures
UR-84-39	Aarsnes, Jan V.	Current forces on ships
UR-84-40	Czujko, Jerzy	Collapse Analysis of Plates subjected to Biaxial Compression and Lateral Load
UR-85-46	Alf G. Engseth, MK	Finite element collapse analysis of tubular steel offshore structures. (Dr.Ing. Thesis)
UR-86-47	Dengody Sheshappa, MP	A Computer Design Model for Optimizing Fishing Vessel Designs Based on Techno-Economic Analysis. (Dr.Ing. Thesis)
UR-86-48	Vidar Aanesland, MH	A Theoretical and Numerical Study of Ship Wave Resistance. (Dr.Ing. Thesis)
UR-86-49	Heinz-Joachim Wessel, MK	Fracture Mechanics Analysis of Crack Growth in Plate Girders. (Dr.Ing. Thesis)
UR-86-50	Jon Taby, MK	Ultimate and Post-ultimate Strength of Dented Tubular Members. (Dr.Ing. Thesis)
UR-86-51	Walter Lian, MH	A Numerical Study of Two-Dimensional Separated Flow Past Bluff Bodies at Moderate KC-Numbers. (Dr.Ing. Thesis)
UR-86-52	Bjørn Sortland, MH	Force Measurements in Oscillating Flow on Ship Sections and Circular Cylinders in a U-Tube Water Tank. (Dr.Ing. Thesis)
UR-86-53	Kurt Strand, MM	A System Dynamic Approach to One-dimensional Fluid Flow. (Dr.Ing. Thesis)
UR-86-54	Arne Edvin Løken, MH	Three Dimensional Second Order Hydrodynamic Effects on Ocean Structures in Waves. (Dr.Ing. Thesis)
UR-86-55	Sigurd Falch, MH	A Numerical Study of Slamming of Two-Dimensional Bodies. (Dr.Ing. Thesis)
UR-87-56	Arne Braathen, MH	Application of a Vortex Tracking Method to the Prediction of Roll Damping of a Two-Dimension

		Floating Body. (Dr.Ing. Thesis)
UR-87-57	Bernt Leira, MK	Gaussian Vector Processes for Reliability Analysis involving Wave-Induced Load Effects. (Dr.Ing. Thesis)
UR-87-58	Magnus Småvik, MM	Thermal Load and Process Characteristics in a Two-Stroke Diesel Engine with Thermal Barriers (in Norwegian). (Dr.Ing. Thesis)
MTA-88-59	Bernt Arild Bremdal, MP	An Investigation of Marine Installation Processes – A Knowledge - Based Planning Approach. (Dr.Ing. Thesis)
MTA-88-60	Xu Jun, MK	Non-linear Dynamic Analysis of Space-framed Offshore Structures. (Dr.Ing. Thesis)
MTA-89-61	Gang Miao, MH	Hydrodynamic Forces and Dynamic Responses of Circular Cylinders in Wave Zones. (Dr.Ing. Thesis)
MTA-89-62	Martin Greenhow, MH	Linear and Non-Linear Studies of Waves and Floating Bodies. Part I and Part II. (Dr.Techn. Thesis)
MTA-89-63	Chang Li, MH	Force Coefficients of Spheres and Cubes in Oscillatory Flow with and without Current. (Dr.Ing. Thesis
MTA-89-64	Hu Ying, MP	A Study of Marketing and Design in Development of Marine Transport Systems. (Dr.Ing. Thesis)
MTA-89-65	Arild Jæger, MH	Seakeeping, Dynamic Stability and Performance of a Wedge Shaped Planing Hull. (Dr.Ing. Thesis)
MTA-89-66	Chan Siu Hung, MM	The dynamic characteristics of tilting-pad bearings
MTA-89-67	Kim Wikstrøm, MP	Analysis av projekteringen for ett offshore projekt. (Licenciat-avhandling)
MTA-89-68	Jiao Guoyang, MK	Reliability Analysis of Crack Growth under Random Loading, considering Model Updating. (Dr.Ing. Thesis)
MTA-89-69	Arnt Olufsen, MK	Uncertainty and Reliability Analysis of Fixed Offshore Structures. (Dr.Ing. Thesis)
MTA-89-70	Wu Yu-Lin, MR	System Reliability Analyses of Offshore Structures using improved Truss and Beam Models. (Dr.Ing. Thesis)
MTA-90-71	Jan Roger Hoff, MH	Three-dimensional Green function of a vessel with forward speed in waves. (Dr.Ing. Thesis)
MTA-90-72	Rong Zhao, MH	Slow-Drift Motions of a Moored Two-Dimensional Body in Irregular Waves. (Dr.Ing. Thesis)
MTA-90-73	Atle Minsaas, MP	Economical Risk Analysis. (Dr.Ing. Thesis)
MTA-90-74	Knut-Aril Farnes, MK	Long-term Statistics of Response in Non-linear Marine Structures. (Dr.Ing. Thesis)
MTA-90-	Torbjørn Sotberg, MK	Application of Reliability Methods for Safety

75		Assessment of Submarine Pipelines. (Dr.Ing. Thesis)
MTA-90-76	Zeuthen, Steffen, MP	SEAMAID. A computational model of the design process in a constraint-based logic programming environment. An example from the offshore domain. (Dr.Ing. Thesis)
MTA-91-77	Haagensen, Sven, MM	Fuel Dependant Cyclic Variability in a Spark Ignition Engine - An Optical Approach. (Dr.Ing. Thesis)
MTA-91-78	Løland, Geir, MH	Current forces on and flow through fish farms. (Dr.Ing. Thesis)
MTA-91-79	Hoen, Christopher, MK	System Identification of Structures Excited by Stochastic Load Processes. (Dr.Ing. Thesis)
MTA-91-80	Haugen, Stein, MK	Probabilistic Evaluation of Frequency of Collision between Ships and Offshore Platforms. (Dr.Ing. Thesis)
MTA-91-81	Sødahl, Nils, MK	Methods for Design and Analysis of Flexible Risers. (Dr.Ing. Thesis)
MTA-91-82	Ormberg, Harald, MK	Non-linear Response Analysis of Floating Fish Farm Systems. (Dr.Ing. Thesis)
MTA-91-83	Marley, Mark J., MK	Time Variant Reliability under Fatigue Degradation. (Dr.Ing. Thesis)
MTA-91-84	Krokstad, Jørgen R., MH	Second-order Loads in Multidirectional Seas. (Dr.Ing. Thesis)
MTA-91-85	Molteberg, Gunnar A., MM	The Application of System Identification Techniques to Performance Monitoring of Four Stroke Turbocharged Diesel Engines. (Dr.Ing. Thesis)
MTA-92-86	Mørch, Hans Jørgen Bjelke, MH	Aspects of Hydrofoil Design: with Emphasis on Hydrofoil Interaction in Calm Water. (Dr.Ing. Thesis)
MTA-92-87	Chan Siu Hung, MM	Nonlinear Analysis of Rotordynamic Instabilities in Highspeed Turbomachinery. (Dr.Ing. Thesis)
MTA-92-88	Bessason, Bjarni, MK	Assessment of Earthquake Loading and Response of Seismically Isolated Bridges. (Dr.Ing. Thesis)
MTA-92-89	Langli, Geir, MP	Improving Operational Safety through exploitation of Design Knowledge - an investigation of offshore platform safety. (Dr.Ing. Thesis)
MTA-92-90	Sævik, Svein, MK	On Stresses and Fatigue in Flexible Pipes. (Dr.Ing. Thesis)
MTA-92-91	Ask, Tor Ø., MM	Ignition and Flame Growth in Lean Gas-Air Mixtures. An Experimental Study with a Schlieren System. (Dr.Ing. Thesis)
MTA-86-92	Hessen, Gunnar, MK	Fracture Mechanics Analysis of Stiffened Tubular

		Members. (Dr.Ing. Thesis)
MTA-93-93	Steinebach, Christian, MM	Knowledge Based Systems for Diagnosis of Rotating Machinery. (Dr.Ing. Thesis)
MTA-93-94	Dalane, Jan Inge, MK	System Reliability in Design and Maintenance of Fixed Offshore Structures. (Dr.Ing. Thesis)
MTA-93-95	Steen, Sverre, MH	Cobblestone Effect on SES. (Dr.Ing. Thesis)
MTA-93-96	Karunakaran, Daniel, MK	Nonlinear Dynamic Response and Reliability Analysis of Drag-dominated Offshore Platforms. (Dr.Ing. Thesis)
MTA-93-97	Hagen, Arnulf, MP	The Framework of a Design Process Language. (Dr.Ing. Thesis)
MTA-93-98	Nordrik, Rune, MM	Investigation of Spark Ignition and Autoignition in Methane and Air Using Computational Fluid Dynamics and Chemical Reaction Kinetics. A Numerical Study of Ignition Processes in Internal Combustion Engines. (Dr.Ing. Thesis)
MTA-94-99	Passano, Elizabeth, MK	Efficient Analysis of Nonlinear Slender Marine Structures. (Dr.Ing. Thesis)
MTA-94-100	Kvålsvold, Jan, MH	Hydroelastic Modelling of Wetdeck Slamming on Multihull Vessels. (Dr.Ing. Thesis)
MTA-94-102	Bech, Sidsel M., MK	Experimental and Numerical Determination of Stiffness and Strength of GRP/PVC Sandwich Structures. (Dr.Ing. Thesis)
MTA-95-103	Paulsen, Hallvard, MM	A Study of Transient Jet and Spray using a Schlieren Method and Digital Image Processing. (Dr.Ing. Thesis)
MTA-95-104	Hovde, Geir Olav, MK	Fatigue and Overload Reliability of Offshore Structural Systems, Considering the Effect of Inspection and Repair. (Dr.Ing. Thesis)
MTA-95-105	Wang, Xiaozhi, MK	Reliability Analysis of Production Ships with Emphasis on Load Combination and Ultimate Strength. (Dr.Ing. Thesis)
MTA-95-106	Ulstein, Tore, MH	Nonlinear Effects of a Flexible Stern Seal Bag on Cobblestone Oscillations of an SES. (Dr.Ing. Thesis)
MTA-95-107	Solaas, Frøydis, MH	Analytical and Numerical Studies of Sloshing in Tanks. (Dr.Ing. Thesis)
MTA-95-108	Hellan, Øyvind, MK	Nonlinear Pushover and Cyclic Analyses in Ultimate Limit State Design and Reassessment of Tubular Steel Offshore Structures. (Dr.Ing. Thesis)
MTA-95-109	Hermundstad, Ole A., MK	Theoretical and Experimental Hydroelastic Analysis of High Speed Vessels. (Dr.Ing. Thesis)
MTA-96-110	Bratland, Anne K., MH	Wave-Current Interaction Effects on Large-Volume Bodies in Water of Finite Depth. (Dr.Ing. Thesis)

MTA-96-111	Herfjord, Kjell, MH	A Study of Two-dimensional Separated Flow by a Combination of the Finite Element Method and Navier-Stokes Equations. (Dr.Ing. Thesis)
MTA-96-112	Æsøy, Vilmar, MM	Hot Surface Assisted Compression Ignition in a Direct Injection Natural Gas Engine. (Dr.Ing. Thesis)
MTA-96-113	Eknes, Monika L., MK	Escalation Scenarios Initiated by Gas Explosions on Offshore Installations. (Dr.Ing. Thesis)
MTA-96-114	Erikstad, Stein O., MP	A Decision Support Model for Preliminary Ship Design. (Dr.Ing. Thesis)
MTA-96-115	Pedersen, Egil, MH	A Nautical Study of Towed Marine Seismic Streamer Cable Configurations. (Dr.Ing. Thesis)
MTA-97-116	Moksnes, Paul O., MM	Modelling Two-Phase Thermo-Fluid Systems Using Bond Graphs. (Dr.Ing. Thesis)
MTA-97-117	Halse, Karl H., MK	On Vortex Shedding and Prediction of Vortex-Induced Vibrations of Circular Cylinders. (Dr.Ing. Thesis)
MTA-97-118	Igland, Ragnar T., MK	Reliability Analysis of Pipelines during Laying, considering Ultimate Strength under Combined Loads. (Dr.Ing. Thesis)
MTA-97-119	Pedersen, Hans-P., MP	Levendefiskteknologi for fiskefartøy. (Dr.Ing. Thesis)
MTA-98-120	Vikestad, Kyrre, MK	Multi-Frequency Response of a Cylinder Subjected to Vortex Shedding and Support Motions. (Dr.Ing. Thesis)
MTA-98-121	Azadi, Mohammad R. E., MK	Analysis of Static and Dynamic Pile-Soil-Jacket Behaviour. (Dr.Ing. Thesis)
MTA-98-122	Ulltang, Terje, MP	A Communication Model for Product Information. (Dr.Ing. Thesis)
MTA-98-123	Torbergsen, Erik, MM	Impeller/Diffuser Interaction Forces in Centrifugal Pumps. (Dr.Ing. Thesis)
MTA-98-124	Hansen, Edmond, MH	A Discrete Element Model to Study Marginal Ice Zone Dynamics and the Behaviour of Vessels Moored in Broken Ice. (Dr.Ing. Thesis)
MTA-98-125	Videiro, Paulo M., MK	Reliability Based Design of Marine Structures. (Dr.Ing. Thesis)
MTA-99-126	Mainçon, Philippe, MK	Fatigue Reliability of Long Welds Application to Titanium Risers. (Dr.Ing. Thesis)
MTA-99-127	Haugen, Elin M., MH	Hydroelastic Analysis of Slamming on Stiffened Plates with Application to Catamaran Wetdecks. (Dr.Ing. Thesis)
MTA-99-128	Langhelle, Nina K., MK	Experimental Validation and Calibration of Nonlinear Finite Element Models for Use in Design of Aluminium Structures Exposed to Fire. (Dr.Ing.

		Thesis)
MTA-99-129	Berstad, Are J., MK	Calculation of Fatigue Damage in Ship Structures. (Dr.Ing. Thesis)
MTA-99-130	Andersen, Trond M., MM	Short Term Maintenance Planning. (Dr.Ing. Thesis)
MTA-99-131	Tveiten, Bård Wathne, MK	Fatigue Assessment of Welded Aluminium Ship Details. (Dr.Ing. Thesis)
MTA-99-132	Søreide, Fredrik, MP	Applications of underwater technology in deep water archaeology. Principles and practice. (Dr.Ing. Thesis)
MTA-99-133	Tønnessen, Rune, MH	A Finite Element Method Applied to Unsteady Viscous Flow Around 2D Blunt Bodies With Sharp Corners. (Dr.Ing. Thesis)
MTA-99-134	Elvekrok, Dag R., MP	Engineering Integration in Field Development Projects in the Norwegian Oil and Gas Industry. The Supplier Management of Norne. (Dr.Ing. Thesis)
MTA-99-135	Fagerholt, Kjetil, MP	Optimeringsbaserte Metoder for Ruteplanlegging innen skipsfart. (Dr.Ing. Thesis)
MTA-99-136	Bysveen, Marie, MM	Visualization in Two Directions on a Dynamic Combustion Rig for Studies of Fuel Quality. (Dr.Ing. Thesis)
MTA-2000-137	Storteig, Eskild, MM	Dynamic characteristics and leakage performance of liquid annular seals in centrifugal pumps. (Dr.Ing. Thesis)
MTA-2000-138	Sagli, Gro, MK	Model uncertainty and simplified estimates of long term extremes of hull girder loads in ships. (Dr.Ing. Thesis)
MTA-2000-139	Tronstad, Harald, MK	Nonlinear analysis and design of cable net structures like fishing gear based on the finite element method. (Dr.Ing. Thesis)
MTA-2000-140	Kroneberg, André, MP	Innovation in shipping by using scenarios. (Dr.Ing. Thesis)
MTA-2000-141	Haslum, Herbjørn Alf, MH	Simplified methods applied to nonlinear motion of spar platforms. (Dr.Ing. Thesis)
MTA-2001-142	Samdal, Ole Johan, MM	Modelling of Degradation Mechanisms and Stressor Interaction on Static Mechanical Equipment Residual Lifetime. (Dr.Ing. Thesis)
MTA-2001-143	Baarholm, Rolf Jarle, MH	Theoretical and experimental studies of wave impact underneath decks of offshore platforms. (Dr.Ing. Thesis)
MTA-2001-144	Wang, Lihua, MK	Probabilistic Analysis of Nonlinear Wave-induced Loads on Ships. (Dr.Ing. Thesis)
MTA-2001-145	Kristensen, Odd H. Holt, MK	Ultimate Capacity of Aluminium Plates under Multiple Loads, Considering HAZ Properties. (Dr.Ing. Thesis)

MTA-2001-146	Greco, Marilena, MH	A Two-Dimensional Study of Green-Water Loading. (Dr.Ing. Thesis)
MTA-2001-147	Heggelund, Svein E., MK	Calculation of Global Design Loads and Load Effects in Large High Speed Catamarans. (Dr.Ing. Thesis)
MTA-2001-148	Babalola, Olusegun T., MK	Fatigue Strength of Titanium Risers – Defect Sensitivity. (Dr.Ing. Thesis)
MTA-2001-149	Mohammed, Abuu K., MK	Nonlinear Shell Finite Elements for Ultimate Strength and Collapse Analysis of Ship Structures. (Dr.Ing. Thesis)
MTA-2002-150	Holmedal, Lars E., MH	Wave-current interactions in the vicinity of the sea bed. (Dr.Ing. Thesis)
MTA-2002-151	Rognebakke, Olav F., MH	Sloshing in rectangular tanks and interaction with ship motions. (Dr.Ing. Thesis)
MTA-2002-152	Lader, Pål Furset, MH	Geometry and Kinematics of Breaking Waves. (Dr.Ing. Thesis)
MTA-2002-153	Yang, Qinzheng, MH	Wash and wave resistance of ships in finite water depth. (Dr.Ing. Thesis)
MTA-2002-154	Melhus, Øyvin, MM	Utilization of VOC in Diesel Engines. Ignition and combustion of VOC released by crude oil tankers. (Dr.Ing. Thesis)
MTA-2002-155	Ronæss, Marit, MH	Wave Induced Motions of Two Ships Advancing on Parallel Course. (Dr.Ing. Thesis)
MTA-2002-156	Økland, Ole D., MK	Numerical and experimental investigation of whipping in twin hull vessels exposed to severe wet deck slamming. (Dr.Ing. Thesis)
MTA-2002-157	Ge, Chunhua, MK	Global Hydroelastic Response of Catamarans due to Wet Deck Slamming. (Dr.Ing. Thesis)
MTA-2002-158	Byklum, Eirik, MK	Nonlinear Shell Finite Elements for Ultimate Strength and Collapse Analysis of Ship Structures. (Dr.Ing. Thesis)
IMT-2003-1	Chen, Haibo, MK	Probabilistic Evaluation of FPSO-Tanker Collision in Tandem Offloading Operation. (Dr.Ing. Thesis)
IMT-2003-2	Skaugset, Kjetil Bjørn, MK	On the Suppression of Vortex Induced Vibrations of Circular Cylinders by Radial Water Jets. (Dr.Ing. Thesis)
IMT-2003-3	Chezhian, Muthu	Three-Dimensional Analysis of Slamming. (Dr.Ing. Thesis)
IMT-2003-4	Buhaug, Øyvind	Deposit Formation on Cylinder Liner Surfaces in Medium Speed Engines. (Dr.Ing. Thesis)
IMT-2003-5	Tregde, Vidar	Aspects of Ship Design: Optimization of Aft Hull with Inverse Geometry Design. (Dr.Ing. Thesis)
IMT-2003-6	Wist, Hanne Therese	Statistical Properties of Successive Ocean Wave

		Parameters. (Dr.Ing. Thesis)
IMT-2004-7	Ransau, Samuel	Numerical Methods for Flows with Evolving Interfaces. (Dr.Ing. Thesis)
IMT-2004-8	Soma, Torkel	Blue-Chip or Sub-Standard. A data interrogation approach of identity safety characteristics of shipping organization. (Dr.Ing. Thesis)
IMT-2004-9	Ersdal, Svein	An experimental study of hydrodynamic forces on cylinders and cables in near axial flow. (Dr.Ing. Thesis)
IMT-2005-10	Brodtkorb, Per Andreas	The Probability of Occurrence of Dangerous Wave Situations at Sea. (Dr.Ing. Thesis)
IMT-2005-11	Yttervik, Rune	Ocean current variability in relation to offshore engineering. (Dr.Ing. Thesis)
IMT-2005-12	Fredheim, Arne	Current Forces on Net-Structures. (Dr.Ing. Thesis)
IMT-2005-13	Heggernes, Kjetil	Flow around marine structures. (Dr.Ing. Thesis
IMT-2005-14	Fouques, Sebastien	Lagrangian Modelling of Ocean Surface Waves and Synthetic Aperture Radar Wave Measurements. (Dr.Ing. Thesis)
IMT-2006-15	Holm, Håvard	Numerical calculation of viscous free surface flow around marine structures. (Dr.Ing. Thesis)
IMT-2006-16	Bjørheim, Lars G.	Failure Assessment of Long Through Thickness Fatigue Cracks in Ship Hulls. (Dr.Ing. Thesis)
IMT-2006-17	Hansson, Lisbeth	Safety Management for Prevention of Occupational Accidents. (Dr.Ing. Thesis)
IMT-2006-18	Zhu, Xinying	Application of the CIP Method to Strongly Nonlinear Wave-Body Interaction Problems. (Dr.Ing. Thesis)
IMT-2006-19	Reite, Karl Johan	Modelling and Control of Trawl Systems. (Dr.Ing. Thesis)
IMT-2006-20	Smogeli, Øyvind Notland	Control of Marine Propellers. From Normal to Extreme Conditions. (Dr.Ing. Thesis)
IMT-2007-21	Storhaug, Gaute	Experimental Investigation of Wave Induced Vibrations and Their Effect on the Fatigue Loading of Ships. (Dr.Ing. Thesis)
IMT-2007-22	Sun, Hui	A Boundary Element Method Applied to Strongly Nonlinear Wave-Body Interaction Problems. (PhD Thesis, CeSOS)
IMT-2007-23	Rustad, Anne Marthine	Modelling and Control of Top Tensioned Risers. (PhD Thesis, CeSOS)
IMT-2007-24	Johansen, Vegar	Modelling flexible slender system for real-time simulations and control applications
IMT-2007-25	Wroldsen, Anders Sunde	Modelling and control of tensegrity structures. (PhD

		Thesis, CeSOS)
IMT-2007-26	Aronsen, Kristoffer Høye	An experimental investigation of in-line and combined inline and cross flow vortex induced vibrations. (Dr. avhandling, IMT)
IMT-2007-27	Gao, Zhen	Stochastic Response Analysis of Mooring Systems with Emphasis on Frequency-domain Analysis of Fatigue due to Wide-band Response Processes (PhD Thesis, CeSOS)
IMT-2007-28	Thorstensen, Tom Anders	Lifetime Profit Modelling of Ageing Systems Utilizing Information about Technical Condition. (Dr.ing. thesis, IMT)
IMT-2008-29	Berntsen, Per Ivar B.	Structural Reliability Based Position Mooring. (PhD-Thesis, IMT)
IMT-2008-30	Ye, Naiquan	Fatigue Assessment of Aluminium Welded Box-stiffener Joints in Ships (Dr.ing. thesis, IMT)
IMT-2008-31	Radan, Damir	Integrated Control of Marine Electrical Power Systems. (PhD-Thesis, IMT)
IMT-2008-32	Thomassen, Paul	Methods for Dynamic Response Analysis and Fatigue Life Estimation of Floating Fish Cages. (Dr.ing. thesis, IMT)
IMT-2008-33	Pákozdi, Csaba	A Smoothed Particle Hydrodynamics Study of Two-dimensional Nonlinear Sloshing in Rectangular Tanks. (Dr.ing.thesis, IMT)
IMT-2007-34	Grytøyr, Guttorm	A Higher-Order Boundary Element Method and Applications to Marine Hydrodynamics. (Dr.ing.thesis, IMT)
IMT-2008-35	Drummen, Ingo	Experimental and Numerical Investigation of Nonlinear Wave-Induced Load Effects in Containerships considering Hydroelasticity. (PhD thesis, CeSOS)
IMT-2008-36	Skejic, Renato	Maneuvering and Seakeeping of a Singel Ship and of Two Ships in Interaction. (PhD-Thesis, CeSOS)
IMT-2008-37	Harlem, Alf	An Age-Based Replacement Model for Repairable Systems with Attention to High-Speed Marine Diesel Engines. (PhD-Thesis, IMT)
IMT-2008-38	Alsos, Hagbart S.	Ship Grounding. Analysis of Ductile Fracture, Bottom Damage and Hull Girder Response. (PhD-thesis, IMT)
IMT-2008-39	Graczyk, Mateusz	Experimental Investigation of Sloshing Loading and Load Effects in Membrane LNG Tanks Subjected to Random Excitation. (PhD-thesis, CeSOS)
IMT-2008-40	Taghipour, Reza	Efficient Prediction of Dynamic Response for Flexible amd Multi-body Marine Structures. (PhD-thesis, CeSOS)
IMT-2008-41	Ruth, Eivind	Propulsion control and thrust allocation on marine vessels. (PhD thesis, CeSOS)

IMT-2008-42	Nystad, Bent Helge	Technical Condition Indexes and Remaining Useful Life of Aggregated Systems. PhD thesis, IMT
IMT-2008-43	Soni, Prashant Kumar	Hydrodynamic Coefficients for Vortex Induced Vibrations of Flexible Beams, PhD thesis, CeSOS
IMT-2009-43	Amlashi, Hadi K.K.	Ultimate Strength and Reliability-based Design of Ship Hulls with Emphasis on Combined Global and Local Loads. PhD Thesis, IMT
IMT-2009-44	Pedersen, Tom Arne	Bond Graph Modelling of Marine Power Systems. PhD Thesis, IMT
IMT-2009-45	Kristiansen, Trygve	Two-Dimensional Numerical and Experimental Studies of Piston-Mode Resonance. PhD-Thesis, CeSOS
IMT-2009-46	Ong, Muk Chen	Applications of a Standard High Reynolds Number Model and a Stochastic Scour Prediction Model for Marine Structures. PhD-thesis, IMT
IMT-2009-47	Hong, Lin	Simplified Analysis and Design of Ships subjected to Collision and Grounding. PhD-thesis, IMT
IMT-2009-48	Koushan, Kamran	Vortex Induced Vibrations of Free Span Pipelines, PhD thesis, IMT
IMT-2009-49	Korsvik, Jarl Eirik	Heuristic Methods for Ship Routing and Scheduling. PhD-thesis, IMT
IMT-2009-50	Lee, Jihoon	Experimental Investigation and Numerical in Analyzing the Ocean Current Displacement of Longlines. Ph.d.-Thesis, IMT.
IMT-2009-51	Vestbøstad, Tone Gran	A Numerical Study of Wave-in-Deck Impact usin a Two-Dimensional Constrained Interpolation Profile Method, Ph.d.thesis, CeSOS.
IMT-2009-52	Bruun, Kristine	Bond Graph Modelling of Fuel Cells for Marine Power Plants. Ph.d.-thesis, IMT
IMT 2009-53	Holstad, Anders	Numerical Investigation of Turbulence in a Sekwed Three-Dimensional Channel Flow, Ph.d.-thesis, IMT.
IMT 2009-54	Ayala-Uraga, Efren	Reliability-Based Assessment of Deteriorating Ship-shaped Offshore Structures, Ph.d.-thesis, IMT
IMT 2009-55	Kong, Xiangjun	A Numerical Study of a Damaged Ship in Beam Sea Waves. Ph.d.-thesis, IMT/CeSOS.
IMT 2010-56	Kristiansen, David	Wave Induced Effects on Floaters of Aquaculture Plants, Ph.d.-thesis, IMT/CeSOS.
IMT 2010-57	Ludvigsen, Martin	An ROV-Toolbox for Optical and Acoustic Scientific Seabed Investigation. Ph.d.-thesis IMT.
IMT 2010-58	Hals, Jørgen	Modelling and Phase Control of Wave-Energy Converters Ph.d.thesis, CeSOS.

IMT 2010-59	Shu, Zhi	Uncertainty Assesment of Wave Loads and Ultimate Strength of Tankers and Bulk Carriers in a Reliability Framework, Ph.d.-thesis, IMT.
IMT 2010-60	Jakobsen, Ken-Robert G.	Turbulence Modeling of Transverse Flow on Ship Hulls in Shallow Water. Ph.d.thesis, IMT.
IMT 2010-61	Shao, Yanlin	Numerical Potential-Flow Studies on Weakly-Nonlinear Wave-Body Interactions with/without Small Forward Speed, Ph.d.thesis, IMT.
IMT 2010-62	Califano, Andrea	Dynamic Loads on Marine Propellers due to Intermittent Ventilation. Ph.d.thesis, IMT.